Data-driven Tactile Sensing using Spatially Overlapping Signals

Pedro Piacenza

Submitted in partial fulfillment of the
requirements for the degree of
Doctor of Philosophy
under the Executive Committee
of the Graduate School of Arts and Sciences

COLUMBIA UNIVERSITY

2020

Abstract

Data-driven Tactile Sensing using Spatially Overlapping Signals

Pedro Piacenza

Providing robots with distributed, robust and accurate tactile feedback is a fundamental problem in robotics because of the large number of tasks that require physical interaction with objects. Tactile sensors can provide robots with information about the location of each point of contact with the manipulated object, an estimation of the contact forces applied (normal and shear) and even slip detection. Despite significant advances in touch and force transduction, tactile sensing is still far from ubiquitous in robotic manipulation. Existing methods for building touch sensors have proven difficult to integrate into robot fingers due to multiple challenges, including difficulty in covering multicurved surfaces, high wire count, or packaging constrains preventing their use in dexterous hands.

In this dissertation, we focus on the development of soft tactile systems that can be deployed over complex, three-dimensional surfaces with a low wire count and using easily accessible manufacturing methods. To this effect, we present a general methodology called *spatially overlapping signals*. The key idea behind our method is to embed multiple sensing terminals in a volume of soft material which can be deployed over arbitrary, non-developable surfaces. Unlike a traditional taxel, these sensing terminals are not capable of measuring strain on their own. Instead, we take measurements across pairs of sensing terminals. Applying strain in the receptive field of this terminal pair should measurably affect the signal associated with it. As we embed multiple sensing

terminals in this soft material, a significant overlap of these receptive fields occurs across the whole active sensing area, providing us with a very rich dataset characterizing the contact event. The use of an all-pairs approach, where all possible combinations of sensing terminals pairs are used, maximizes the number of signals extracted while reducing the total number of wires for the overall sensor, which in turn facilitates its integration.

Building an analytical model for how this rich signal set relates to various contacts events can be very challenging. Further, any such model would depend on knowing the exact locations of the terminals in the sensor, thus requiring very precise manufacturing. Instead, we build forward models of our sensors from data. We collect training data using a dataset of controlled indentations of known characteristics, directly learning the mapping between our signals and the variables characterizing a contact event. This approach allows for accessible, cheap manufacturing while enabling extensive coverage of curved surfaces.

The concept of spatially overlapping signals can be realized using various transduction methods; we demonstrate sensors using piezoresistance, pressure transducers and optics. With piezoresistivity we measure resistance values across various electrodes embedded in a carbon nanotubes infused elastomer to determine the location of touch. Using commercially available pressure transducers embedded in various configurations inside a soft volume of rubber, we show its possible to localize contacts across a curved surface. Finally, using optics, we measure light transport between LEDs and photodiodes inside a clear elastomer which makes up our sensor. Our optical sensors are able to detect both the location and depth of an indentation very accurately on both planar and multicurved surfaces.

Our *Distributed Interleaved Signals for Contact via Optics* or D.I.S.C.O Finger is the culmination of this methodology: a fully integrated, sensorized robot finger, with a low wire count and designed for easy integration into dexterous manipulators. Our DISCO Finger can generally determine contact location with sub-millimeter accuracy, and contact force to within 10% (and often with 5%) of the true value without the need for analytical models. While our data-driven method requires training data representative of the final operational conditions that the system will encounter, we show our finger can be robust to novel contact scenarios where the shape of the indenter has not been seen during training. Moreover, the forward model that predicts contact locations and applied normal force can be transfered to new fingers with minimal loss of performance, eliminating the need to collect training data for each individual finger. We believe that rich tactile information, in a highly functional form with limited blind spots and a simple integration path into complete systems, like we demonstrate in this dissertation, will prove to be an important enabler for data-driven complex robotic motor skills, such as dexterous manipulation.

Table of Contents

List of Tables

List of Figures

Acknowledgements

So many have helped me along this journey. First, I would like to express my gratitude to my advisor, Matei Ciocarlie. I find it hard to put into words the profound effect your mentorship had over this body of work and over my own personal growth. I will always admire your clarity of thought and immense capability to engage people. Your advice, support and availability helped me push through the hardest of challenges. I could not have asked for a more involved, caring and friendly advisor. I also want to thank John Kymissis, our long-time collaborator, for all of his guidance and patience towards my endless questions.

Looking back, many colleagues helped make this project a reality. Keith Behrman played a huge role in the design and engineering of the DISCO Finger electronics and never complained about my incessant demand for new iterations. Benedikt Schifferer, for all the data crunching and neural network optimization that made the DISCO Finger possible. Sydney Sherman, for the long hours dedicated to the simulation of our tactile dome. And to all of my labmates - Max, Cassie, Tianjian, Sangwoo, Emily - thank you for making our lab such an amazing place to spend my time over the last five years.

Last but not least, I would like to thank my family and friends. Without my parents' support I would have never been able to pursue my graduate education. They made an incredible sacrifice, prioritizing my education over their own plans without ever showing an ounce of hesitation or expecting anything in return. To my sister Teresa and brother-in-law Federico: I will always be in debt to you as well. You opened the doors of your house and your lives to me and made all of this possible. I will always look back fondly to our time living together. Finally, to my significant other, Alicia. Thank you for your love, your company and your unconditional support. I cannot wait to see what lies ahead for us.

Chapter 1: Introduction

1.1 Motivation

Industrial robots have transformed manufacturing since they first appeared in factories during the second half of the twentieth century. Robots took over humans in performing repetitive tasks in structured environments that usually required high positional accuracy. For the remainder of the century, in general, the success story of robotic automation entailed robots operating in cages, separated from humans and with almost complete knowledge of their environment. This extensive prior knowledge of the task and environment meant that these robots required minimal capabilities to sense the world around them.

Recently the field of robotics is expanding from these highly structured environments into more complex, human environments such as homes [1], outdoors [2], hospitals [3] and the workplace [4]. These new application areas require robots that are capable to interact with humans, objects and tools to perform a wider range of tasks than ever before. Such robots should be capable of reaching their goal while continuously sensing and adapting to changes in the environment. This continuous adaptation requires robots to be equipped with more advanced sensory capabilities and drives the need for control algorithms that can leverage this vast amount of sensor data. A fundamental part of interacting with the world involves the physical manipulation of objects around us, making the development of tactile feedback systems for robots a key issue in the robotics community.

Tactile sensing is an essential survival tool in nature, with even the simplest organisms possessing tactile capabilities for exploration and as a response to various external stimuli. Neuroscience studies have proven the importance of tactile feedback in humans, particularly for manipulation tasks. An experiment where the subjects had their hands numbed showed that their movements became inaccurate and they had difficulty maintaining a stable grasp of objects [5, 6]. Another study with sensory impaired subjects demonstrated their difficulty when performing manipulation tasks [7]. Our “sense of touch” not only allows us to assess object properties such as size, shape, texture, but it can also detect slip [6] such that we adjust our grasp to keep it stable.

Providing robots with distributed, robust and accurate tactile feedback is a problem of great importance in the robotics community because of the large number of tasks that require the robot to make physical contact with objects. In this dissertation we are particularly concerned with the use of tactile feedback for manipulation. Tactile sensors can provide robots with information about the location of each point of contact with the manipulated object, an estimation of the contact forces (normal and shear) applied and even slip detection [8]. Moreover, with exploratory movements the robot can infer information about the object itself: its texture, shape, stiffness and temperature [9]. All of these capabilities are important to build human-safe systems but also to perform human-like manipulation tasks including in-hand regrasping, rotation and translation.

Tactile sensing modalities designed for robot hands have made great strides over the past years. A number of comprehensive reviews [10–15] describe numerous tactile sensors, based on various transduction methods (e.g. piezoresistance, piezocapacitance, piezoelectricity, optics, ultrasonics, etc.). Still, these advances in sensing modalities are only slowly translating to improved manipulation abilities for robot hands and the usage of tactile sensors in practical applications is still limited [16]. This can be partially attributed to the fact that many researchers put a lot of emphasis on sensor development but stop short of showing full system integration and how to deploy these sensors on robotic hands.

1.2 Goals for tactile sensing in robotics

The main objective of a tactile feedback system is the ability to detect contact events across a given surface. Regardless of implementation details, it is widely accepted that an important metric on any tactile sensor is its spatial resolution: the smallest distance at which the sensor distinguishes two separate contact points, i.e. how accurately it can detect the location of contact. Increasing the spatial resolution of a tactile sensor can be quite expensive from both a manufacturing as well as an algorithmic point of view, as it requires a higher concentration of sensing units. Requirements for spatial resolution can vary depending on the application, but as a general rule, for manipulation tasks it is expected that fingertips can resolve a contact location within approximately 1 *mm* based on equivalent human spatial acuity [17]. It must be noted that, while this particular spatial resolution target is common in the literature, there are not quantitative studies showing this is a meaningful threshold for manipulation tasks. As is the case with the sense of touch in humans, lower resolutions can be acceptable in less sensitive parts like the palm or other parts of the body.

Another important requirement for tactile sensors is their force sensitivity, that is, the smallest detectable variation in applied force. The dynamic range of the sensor - the range between the minimum and maximum force the sensor is able to measure - is usually intertwined with the sensor sensitivity: high sensitivity sensors usually cannot measure big forces and vice versa. Most normal manipulation tasks require forces in the range of $0.1-1$ N [18], but higher forces may be necessary for functional tasks and heavy objects. It is desirable as well that the tactile sensor can measure both the magnitude as well as the direction of applied forces.

We are particularly interested in bridging the existing gap between stand-alone *tactile sensors* and fully integrated *tactile fingers*. Consider a robot hand operating in cluttered, unstructured environments. Just like a stand-alone sensor, a tactile finger should be able to collect and report *rich data characterizing touch*. The information contained in this data will vary depending on the application, but typical use cases require the ability to infer touch location, characteristics of transmitted force, or perhaps the motor actions to be applied by the robot in response to the touch. However, unlike stand-alone sensors, a tactile finger's performance is also determined by the related problems of *shape and coverage*. When operating in clutter, a finger equipped with discontinuous "patches" of tactile sensing, and "unsensed" areas of higher curvature in between (such as edges or corners) has a high chance of making contact in a blind spot.

An additional challenge, beyond those that stem from engineering an effective tactile sensor, is that of processing the tactile data reported by the system [16, 19]. Compared to other senses used in robotics - most notably hearing and visual feedback - the properties of tactile sensor data are decidedly more variable [20–22]. Tactile sensors signals can be high-dimensional, noisy and very likely need to fuse several modalities to capture all relevant features to characterize a contact event [19, 23]. How to incorporate the information obtained from a tactile feedback system into a control algorithm to enhance grasping or manipulation skills is very much an open problem [24–26]. So far, most tactile data is processed using either simple heuristics or, more recently, as an input to a machine learning algorithm. Learning manipulation skills may require large amounts of real-world data, hence many researchers rely on simulated environments [27, 28]. Still, these simulated environments operate under simplified models for soft contacts and deformable objects, which can complicate their use for manipulation tasks.

1.3 Contributions

In this dissertation we focus on the development of a tactile feedback system capable of providing coverage of multicurved arbitrary geometry with a special focus on achieving contact localization and normal force estimation with high accuracy while addressing other system level concerns like manufacturability, low wire count and full integration into robotic fingers. The method we develop is called *spatially overlapping signals*.

This method forgoes the notion of a “taxel” capable of delivering a signal that can be calibrated to a physical magnitude, for example, force. Instead, we have multiple terminals embedded in a soft volume and we measure strain-sensitive signals between all possible terminal pairs: a single terminal can be measured against many others, and any given combination provides a signal. This creates a very rich dataset, as we are able to extract many signals using fewer wires, which in turn facilitates the system integration onto real hands. Moreover, this method can be deployed using various transduction types. A more in depth discussion about the spatially overlapping signals approach can be found on chapter 3.

Because we can extract such a large number of signals from our sensors, we propose that this rich dataset can then be mined in purely data-driven fashion to learn the mapping between these signals and the contact parameters of interest. Another interesting case is to leverage this rich dataset to perform end-to-end learning without an intermediate representations such as force. This approach is enabled by recent advances in machine learning allowing us to train regressors and classifiers on high-dimensional feature spaces, as is the case for our tactile finger.

To summarize our contributions, this dissertation is the first to:

- Propose a transduction-agnostic methodology for tactile sensors - spatially overlapping signals - that can provide coverage over multicurved three-dimensional surfaces and extract a large number of strain sensitive signals while reducing the number of wires for the overall sensor.

- Show that purely data-driven methods can extract useful information from spatially overlapping signals, such as contact locations, normal force and indenter shape. This data-driven method allows us to deploy our sensing terminals on soft materials with simple manufacturing methods and circumvent the need of an analytical model for the sensor.

- Study the use of simulation tools to aid the design of data-driven sensors and evaluate the relative final performance of different distributions of sensing terminals inside a volume of soft material.

- Demonstrate a soft tactile robot finger capable of resolving contact locations with ~1 *mm* accuracy and determine the normal contact force with 5-10% error over a non-developable three-dimensional surface, in a fully integrated, finger-shaped package.

The novelty behind our methodology is that it forces us to rethink tactile systems from a new perspective - moving away from the “one taxel, one signal” approach and encouraging the design of data-rich systems that exploit the recent advent of learning-from-data algorithms. While systems designed under our method can be trained using ground truth to output traditional contact parameters, perhaps their biggest potential lies in the possibility to extract tactile features directly shaped by the task being learned. In a similar fashion to the evolution of computer vision through the use of convolutional neural networks, as machine learning becomes the norm in terms of extracting relevant features from tactile information, we believe there is great value in the design of sensors that are intrinsically amenable to serve as platforms for learning algorithms. With their ability to capture rich tactile information and the ease of integration, these type of tactile sensors could finally bring us closer to enabling dexterous manipulation for robots.

1.4 Dissertation outline

The structure of this dissertation mostly follows the chronological order in which we developed our methodology of spatially overlapping signals. Chapter 3 elaborates in detail our spatially overlapping signals method. Chapter 4 presents our first sensor prototype using this approach, based on piezoresistivity, which serves as an initial validation to our method. In chapter 5 we consider a different transduction method using MEMS ("Micro-Electro-Mechanical System") pressure transducers and study the relationship between the location of sensing terminals and the resulting localization performance on a curved surface. Chapter 6 introduces our planar optic sensors, where we show the ability to predict both the location and depth of an indentation. We also demonstrate classification of different indenter shapes and show the sensor robustness when encountering new indenter geometries. Finally, chapters 7 and 8 focus on the DISCO Finger. This sensor demonstrates it is possible to use our spatially overlapping signals method to build curved sensors with extensive coverage and a low wire count while providing very accurate contact localization and normal force measurements.

Chapter 2: Related work

We organize some of the related work under three sections. First, we go through related sensors in terms of their design and transduction methodologies, that is, the mechanism under which they convert mechanical strain or forces into an electrical signal. We briefly comment on how those transduction principles work and their general advantages and disadvantages. Second, we present relevant work based on the sensor data processing: how the signals are treated or processed to make a device an effective tactile sensor. Finally, we discuss machine learning approaches and their applications in tactile feedback systems.

2.1 Sensor design and transduction types

Numerous types of transduction principles have been explored during the last two decades when building tactile sensors: resistive, capacitive, optical, ultrasonic, magnetism-based, piezoelectric, tunnel effect sensors, etc. We refer the reader to a number of comprehensive reviews [10–15] for a more extensive overview of these methods. Our goal however is not to explore a new sensing modality; rather, we are looking to build on top of these in order to find a methodology to deploy them over three dimensional surfaces while providing accurate contact localization and force measurements with a low wire count to facilitate their integration.

The transduction method used in our first sensor, described in chapter 4, is piezoresistivity. A piezoresistive material is one that changes its electrical resistivity when mechanical strain is applied. Piezoresistivity is one of the most commonly used transduction methods for tactile sensing, but its implementations can vary widely: strain-gages, metal or semiconductor materials [29] and materials exploiting quantum tunneling or the percolation mechanism. Our sensor uses the latter mechanism, where a conductive filler is dispersed on an insulating matrix (an elastomer in our case). The motion of the particles inside the matrix, generated by the applied load, induces a rearrangement of the conduction path and thus a variation of electrical resistance. These sensors are usually soft, compliant and cheap to produce. The major drawbacks of these types of devices are represented by the temperature sensitivity and hysteresis phenomena of the sensing response, which can influence the repeatability of the measurements [30]. Another issue is the frailty of the electrical connections between the piezoresistive material and the conditioning circuitry.

Numerous examples of using the percolation method exist in the literature [31–34], with carbon black and carbon nanotubes as the most commonly employed fillers. Multi-layered designs or additional microstructures can further improve performance [35–37]. Recently, embedding microchannels of conductive fluids inside an elastic volume [38–40] has been shown to be an effective alternative to making the entire volume conductive, especially if large strains are desirable. In our sensor however we opt for the simplicity of single volume isotropic materials which can be directly molded into the desired shape.

Another very relevant method to this dissertation, also based on piezoresistance, is Electric Impedance Tomography (EIT) [41]. EIT methods use an electrical conductive material such as rubber, foam or fabric, that responds to localized strain with a local change in conductivity. Using electrodes located along the edge of this conductive material, EIT can produce a map localizing the contact events and quantifying the strain. While originally used for medical applications, EIT techniques have been applied successfully for manufacturing artificial sensitive skin for robotics [42–45]. Because this method uses flexible and sometimes stretchable materials, it is a good candidate to cover complex geometries. Major disadvantages, however, are their relatively low spatial and temporal resolutions, and limited ability to discriminate between pressure intensities and contact areas [46].

Piezoresistive tactile sensing is particularly popular among microelectromechanical systems (MEMS) and silicon (Si)-based tactile sensors. MEMS technology is very attractive for producing dense, highly integrated tactile sensors arrays. Capacitive taxels are also a very popular option to build tactile sensing arrays with these standard miniaturization techniques [47]. In general, while piezoresistive devices offer higher linearity, the capacitive devices are an order of magnitude more sensitive [11]. Regardless of the base transduction principle, attempts to increase spatial resolution have often resulted in the arrangement of multiple miniaturized discrete sensors into a matrix to cover a given target surface. Some of these arrays can develop very high spatial resolution [48–50]. However, a drawback of this approach is the difficulty involved in manufacturing these arrays onto a flexible substrate than can conform to complex surfaces. Possible technologies to overcome this problem include organic FETs/thin film transistors realized on elastomeric substrates and other related techniques [51–53]. Still, wiring and manufacturing complexity are still issues preventing these technologies from being fully integrated into tactile fingers.

A particular MEMS device that has seen wide practical application in robotics is the Takktile from Right Hand Robotics [54] which we use as the sensing element in our tactile dome (chapter 5). These pressure transducers are based on a regular MEMS barometric chip found in various consumer products which is overmolded with rubber to convert it into a tactile sensor. The resulting sensor is very robust as it is protected by the casted rubber while providing good sensitivity and linearity. Jentoft et al. demonstrates a matrix implementation of these sensors on a flexible, stretchable membrane capable of covering curved surfaces [55]. While the Takktiles are mainly designed to measure normal forces, Reeks et al. [56] has shown that positioning them at an angle can produce meaningful signals to measure shear forces. In contrast, our tactile dome focuses on contact localization over a three dimensional surface and does not provide force measurements.

Finally we take a look at previous work on optics-based tactile sensors, which is the main transduction method used in our latest designs. Optic sensors tend to have excellent spatial resolution, sensitivity and they are immune to electro-magnetic interference. However, generally speaking, they can consume more power than other transduction methods and may require high computational costs [57].

Waveguides have been used as force transducers [58, 59] with very high sensitivity, but without contact localization, which, in our case, is provided by overlapping multiple signals in the same waveguide. Levi et al. [60] is able to localize contact, but their method is limited to planar sensors.

Previous work has also used reflection and refraction to build an IR touch sensor that doubles as a proximity [61] or proprioceptive sensor [62], but without localizing contact.

Camera-based systems have become increasingly popular among optic methods [63]. Most of these systems share the commonality of a CMOS (Complementary Metal–Oxide–Semiconductor) or CCD (Charge-Coupled Device) camera sensor recording the deformation of a surface from the inside. Interestingly, these sensors have the advantage of leveraging the latest advancements in image processing using deep learning methods since the data output is an image.

Early work by Begej demonstrated both a planar prototype and a robotic finger operating under this principle [64]. On these prototypes light is guided across a waveguide which is covered with textured transducer membrane (usually the texture is an array of cones). When an object makes contact with the sensor surface, it pushes the transducer membrane to contact the waveguide and the condition for total internal reflection is broken. The scattered light produced where the contact between the waveguide and the membrane happens is captured by the camera to characterize the contact patch and applied force [65].

A similar approach forgoes the transducer membrane in favor of a reflective skin and controlled lighting conditions to reconstruct the surface deformation from the captured image using photometric stereo algorithms. Notable exponents of this approach include the GelSight [66, 67], GelSlim [68, 69] and DIGIT [70] sensors which can provide an incredibly detailed picture of the skin deformation, even showing perfect detail of the object surface texture.

A common variation of the previous approach is the addition of markers on the sensor surface. The main benefit of these markers is to track their displacement enabling the measurement of shear, torsional and normal forces as demonstrated with a modified GelSight sensor [71, 72]. The TacTip family of sensors [73, 74] uses similar markers exclusively (without a reflective skin to resolve contact shape) to demonstrate super-resolution capabilities in localizing contact with submillimeter accuracy. Using the same sensor, Cramphorn et al. showed the ability to infer shear direction and magnitude [75] measuring the area of Voronoi cells constructed around each marker. Ma et al. [69] and Sferrazza et al. [76] demonstrate the use of finite element models to reliably map the markers displacement to the complete contact force distribution on the sensor surface. In terms of force sensing without location or contact shape, Ouyang and Howe use a camera to track a fiduciary marker to build a cheap 6-axis force sensor [77].

In all of these cases, the imaging array must be able to image the entire touch area, hence the camera needs to be positioned far enough from the sensor surface leading to bulky assemblies or partially sensorized fingers. In our work, the sensing terminals are fully distributed, allowing for coverage of large areas and curved geometry. Only most recently have these methods been deployed over curved surfaces [78] and with extended coverage equivalent to our sensors although at a much higher cost [79].

2.2 Tactile data processing

Our spatially overlapping signals methodology leverages the fact that few terminals can give rise to many terminal pairs as we measure strain-sensitive signals between all these pairs and use machine learning methods to map those signals to touch parameters of interest. See chapter 3 for a more detailed description of the method.

Extracting contact information from overlapping signals has been done in the context of methods inspired by Electric Impedance Tomography (EIT) [42, 43, 80, 81]; for a comprehensive survey on the use of EIT for robotic skin see the work of Silvera et al. [46]. EIT offers stretchable, continuous tactile sensing with the ability to discriminate multiple points of contact. Similarly to our method, EIT requires current to be injected across two electrodes and the potential of all other electrodes is measured. From these measurements, the inverse problem of finding the body internal conductivity needs to be solved. This is an ill-posed non-linear problem and its solution usually involves the numerical computation of a jacobian or “sensitivity matrix” from a forward model: given a known conductivity distribution within a body and a known injected current, a finite element method is used to compute the potential at the boundary.

An intrinsic advantage of EIT is that it can produce full contact maps for multi-touch situations, an ability which we have not yet investigated with our method. However, EIT methods require this analytical model for the internal conductivity to construct an image showing the areas where strain is applied, where our sensor is completely data-driven and does not require knowledge of a forward model of the sensor, which allows us to embed terminals along complex multicurved boundaries of three-dimensional sensing areas. The manufacturing of EIT skins is also complex, as Silvera et al. mentions in his review: “These approaches, however, also suffer the disadvantages that exist in any sensor manufactured using conductive fabrics. These include complicated electrode connections, non-linear responses, susceptibility to electrical noise, degradation of response over time and high hysteresis” [46].

Our localization approach can be thought of as a close relative to super-resolution techniques. In general, super-resolution for tactile sensing leverages overlapping receptive fields of neighboring taxels to perceive stimuli detail finer than the sensor resolution. Van den Heever et al. [82] used a similar algorithm to super-resolution imaging, combining several measurements of a 5 by 5 force sensitive resistors array into an overall higher resolution measurement. Lepora and Ward-Cherrier [73] and Lepora et al.[83] used an array of sensors covered in soft silicon foam, such that the sensitive receptive fields of each individual sensor overlap. Using a Bayesian perception method, they obtained a 35-fold improvement of localization acuity (0.12mm) over a sensor resolution of 4mm. Other sensors also use a small number of underlying transducers to recover richer information about the contact. For example, work in the ROBOSKIN project showed how to calibrate multiple piezocapacitive transducers [84] and then used them to recover a complete contact profile [85]. In our spatially overlapping signals method the overlap of receptive fields from different terminal pairs is what allows us to localize contacts, but it is hard to draw a direct comparison with super-resolution as we do not have a clear resolution metric for our sensors.

Our tactile dome described in chapter 5, on the other hand, finds itself closer to a traditional implementation of super-resolution. Guggenheim et al. [86] used Takktile sensors to built a 6 axis force-torque sensor by arranging the sensors in a particular spatial configuration, and fitting an analytical model to the calibration data. This work shows that appropriate spatial arrangement of Takktile sensors can be used to measure multi-axial forces. Although our tactile dome solely focuses on touch localization, we show that the concept of optimizing the geometry and positioning of the pressure sensors inside a volume of soft material can yield significant improvements in the overall sensor performance.

Another similar sensor to our tactile dome was presented by Chathuranga et al. [87] using a permanent magnets embedded in a hemispherical volume of silicon rubber. Three orthogonal hall effect sensors are embedded into the rubber and their individual measurements allow them to determine the displacement of the magnet, which is used to calculate the applied force. Another analogous magnetic-based sensor was built by Paulino et al. [88] using a single Hall-effect based tri-axis magnetometer to measure the displacement of the permanent magnet embedded in the elastomer. They improved sensitivity by intentionally creating an air gap between the elastomer and the magnetometer. Once again both of these sensors focus on determining the applied forces but do not provide touch localization capabilities. Additionally a big disadvantage of these magnetic based tactile sensing systems is that they will not work properly when handling ferromagnetic materials.

Random location of transduction terminals in a soft finger has been used for texture discrimination [89], but without the ability to localize contact or measure force. The BioTac sensor [90] pioneered an overlapping-signals approach for tactile sensing by measuring impedance changes in a fluid, in addition to other multimodal data (fluid temperature and pressure changes due to contact). However, impedance signals were measured between a single ground electrode and multiple working electrodes, producing a number of signals that was linear in the number of electrodes, as opposed to our approach of measuring terminal pairs, thus obtaining a number of signals quadratic in the number of terminals.

Our sensors exploit the large number of signals collected with overlapping receptive fields to provide very high accuracy to localize contacts. In the absence of learning-based or super-resolution techniques, high spatial acuity has been achieved through high-resolution taxel arrays [48–50], which can not cover curved surfaces. The highly active field of e-skin research [35, 52, 53, 91–100] shows promise to overcome such problems through flexible sensors that include features like high density of sensing elements, multimodal sensing, and even actuation [101]. Flexible tactile skin has also been used to sensorize gloves for collecting tactile data on human manipulation [94], and taxelized skins can inherently distinguish multitouch conditions. However, manufacturing complexity, along with system-level issues such as wiring, addressing, signal processing of multiple sensor elements or off-board amplification electronics remain important roadblocks on the way to using e-skin for fully integrated sensorized robot fingers exhibiting sub-millimeter localization accuracy as well as complete coverage of complex non-developable geometry, as we present in this dissertation.

2.3 Data-driven tactile sensing

We rely on data-driven methods to extract contact parameters such as location and normal force from our spatially overlapping signal set. In this sense, our sensor uses machine learning tools to provide these physical quantities as outputs. A close comparison can be drawn with the BioTac which relies on impedance measurements to provide contact localization and force information. Wettels et al. [102] also used data-driven methods like the ones shown in this dissertation to extract these parameters from the impedance signals on their sensor. More common, however, is the case of using machine learning algorithms as a mean to process tactile signals into useful motor actions or classification tasks.

A common application of data-driven methods for tactile sensing is grasp stability classification. Regardless of the tactile sensor used, this use case attempts to predict if a grasp is stable before lifting the object based on proprioception and tactile data [22, 103–105]. It is worth noting that the prediction accuracy is highly dependent on the quality and resolution of the tactile sensor, as demonstrated by Wan and Howe [106]. Other common applications include grasp adaptation or object identification through tactile sensing [100, 103, 107–111]. Meier et al. used a convolutional network to classify stable and slip contacts as well as translational versus rotational slip using a CCD-based tactile sensor [112]. Ponce Wong et al. [113] learned to discriminate between different types of geometric features based on the signals provided by the previously mentioned BioTac sensor while performing exploratory movements. Tawil et al. managed to classify different touch gestures on a novel EIT-based skin [44].

Give how humans rely on both visual and tactile senses to interact with the world around us, it is no surprise that we have seen some recent work leveraging the power of machine learning methods to fuse these sensory inputs and demonstrate enhanced performance on many tasks compared to using only one sensing modality. Watkins et al. [114] fuses a partial view of an object with exploratory tactile information to reconstruct the object geometry using a 3D convolutional neural network (CNN). Lee et al. [115] uses self-supervision to learn a compact and multimodal representation of vision, tactile and proprioception sensory inputs to learn a policy through reinforcement learning (RL) in a peg insertion task. Similarly, Gao et al. [116] uses vision and haptic information from a BioTac sensor to classify surfaces with haptic adjectives (compressible, smooth, fuzzy, etc). Calandra et al. demonstrates an end-to-end learning framework using both raw visual and tactile information to reliably predict grasp success [117] and adjust grasp accordingly if necessary [118].

Machine learning methods leveraging tactile data have also shown interesting results in manipulation tasks. Van Hoof et al. [119] was one of the first to demonstrate manipulation skills acquired through reinforcement learning on an under-actuated compliant hand (ReFlex). They demonstrate a policy that rolls an object between the fingertips using tactile data from the Takktile sensor array in the hand in addition to joint encoder information. The learned tactile skill also generalizes to novel objects. In posterior work, Van Hoof et al. studies the influence of different auto-encoder techniques to find which one yields better learning performance on a task involving the repositioning of a pole using a BioTac sensor [120]. Others have tackled the problem of tactile servoing, i.e given a current tactile state and a goal, also in tactile space, find the set of actions that will make the system transition from the current tactile state to the goal state. Tian et al. [121] proposes the use of deep tactile Model Predictive Control (MPC) for learning to perform tactile servoing from raw tactile signals from a GelSight sensor. They demonstrate the ability to maneuver a ball, manipulate a die to new faces, control a joystick, all entirely by feel. Sutanto et al. [122] uses a BioTac sensor to learn a tactile servoing policy indirectly by learning a latent space dynamics model from demonstrations. Their latent space is engineered to be Euclidean to simplify the control and the inverse dynamics control action can be computed analytically given both the current and target latent states.

While we apply data-driven methods to learn a model of the sensor itself, we believe our sensors make for great candidates in data-driven learning methods as referenced in this section. Developing a data rich sensor simultaneously with the learning techniques that make use of the data can bring us closer to achieving complete tactile systems that enable advanced manipulation skills on robot hands.

Chapter 3: Spatially overlapping signals

The design of a tactile sensor is an exercise in compromise. A large number of sensing units can increase the spatial resolution of the system, but inevitably increases the wiring and cost. Taxels with very high sensitivity usually have poor dynamic range and struggle to measure large forces. Matrices of taxels can result in some very accurate and capable sensors but are extremely challenging to deploy in non-flat surfaces. The use of soft materials provides a major advantage in grip and compliance, but can cause hysteresis and act as a low-pass filter when sensing strain with terminals embedded deep into the material.

To complicate things further, the complete characterization of a contact event can be almost impossible to capture with a single modality. Many 3-axis force sensors are developed as monolithic units and the location of contact cannot be sensed directly. On the flip side, sensing methods that can provide contact localization over a continuous surface, usually cannot sense both shear and normal forces across their active sensing areas. In certain applications, the detection of slip or texture recognition can be of critical importance, which requires sensing units with a frequency response well above 100Hz (humans are capable of detecting vibrations up to 700 Hz [123]).

These are some of the challenges we face when designing a tactile sensor. We think it is not enough to concern ourselves with the sensor or taxel design but also acknowledge the whole tactile feedback *system*: Is it feasible to wire such system in a robot hand? Can it be deployed over arbitrary non-planar geometry? Will it be robust enough to survive impacts and sustained use in a real-world application? Without an answer to these questions, tactile sensors are guaranteed to remain technical exercises with little hope to exist outside a laboratory workbench.

We consider it is especially important to provide extensive coverage over robotic fingers. Many sensors are designed as flat tactile pads that can be incorporated into the fingertip of a robotic finger. In perfect conditions where grasps are executed as planned these designs can be adequate.

However, due to calibration errors, the contact with the object may happen at a different location than the one selected by the grasp planner. In these cases, the flat tactile pad may not approach the object surface in the normal direction and contact may occur at the edge of the sensor, which can compromise the tactile measurement. In the worst case scenario, if the edges of the tactile pad are rigid, they can become blind spots and contacts can fail to register altogether. A curved, continuously smooth surface, much like our own fingers, avoids this problem. Furthermore, to perform dexterous in-hand manipulation tasks where the object changes pose while stability grasped, contacts need to roll across a smooth surface without higher curvature areas or edges. For these reasons, we believe a complete tactile system must provide extensive coverage of three dimensional, curved surfaces.

3.1 Towards a real world tactile sensing methodology

Our method begins with a continuous volume of soft material. In this soft material we embed multiple sensing terminals, much like the mechanoreceptors found in the human dermis. However, unlike human skin, a sensing terminal is not capable of measuring any kind of strain on its own, i.e, it is not a taxel. To measure strain, or a proxy for strain, we require a pair of sensing terminals for the measurement to happen across these two terminals (although we relax this requirement and experiment with a taxel approach in chapter 5). We assume a transduction method such that strain in the soft material in the vicinity of this terminal pair will affect the measurement between the two terminals: generally speaking, every pair of sensing terminals has a signal associated with it.

Each sensing pair also has an associated receptive field or area of influence. Applying mechanical strain within this area will produce a measurable change in the signal for that particular sensing pair. As we embed multiple sensing terminals within the soft material, the active sensing area is covered with the receptive fields of multiple sensing pairs. Because the receptive fields of these pairs overlap over the sensing area, we call this general method *spatially overlapping signals*. Depending on the spatial distribution of our terminals, a single contact event will affect signals between multiple pairs (Figure 3.1). If our transduction method is sensitive enough, a sens-

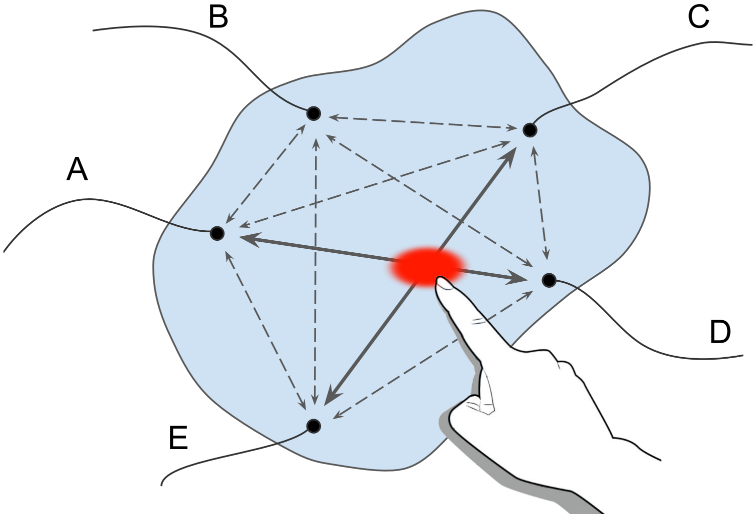

Figure 3.1: Spatially Overlapping Signals. Sensing terminals (A through E) are embedded in a volume of soft material. We group sensing terminal pairs in all possible combinations to extract a rich dataset using fewer wires. Arrows represent the spatial receptive field of a given pair of sensing terminals. A single contact can affect signals extracted from multiple pairs whose receptive fields overlap on the contact location: pairs CE and AD in this illustration.

ing pair can produce a very large receptive field in our active sensing surface if the two terminals are far apart. We believe these large, overlapping receptive fields can provide us with many signals characterizing contact.

We are intentionally vague when using the term “sensing terminal”. This is because the spatially overlapping signals concept itself is transparent when it comes to the sensing transduction method used. In this paper we show this concept applied with three very distinct transduction methods: piezoresistivity, pressure transducers and optics. It must be noted that how we construct these sensing pairs varies depending on the transduction method. A sensing terminal for our piezoresistive sensor (see chapter 4) is merely an electrode, and each pair of electrodes provides us with a resistance measurement. However in the case of our optical sensors (see chapters 6 - 8), a given sensing terminal has a defined role: it can either be an emitter (an LED) or a receiver (a photodiode). The signal associated with each pair relates to the light intensity received by the photodiode. As mentioned above, we relax the sensing pair requirement in our MEMS tactile dome (see chapter 5) as we are using monolithic pressure transducers, where each sensing terminal can provide a measurement.

We strive to extract as much information as possible about contact events in the soft material that makes up our active sensing area. Naturally, as we increase the number and concentration of sensing terminals we should reap the benefits in terms of the tactile system performance. However, we also increase the wiring complexity of the system which can jeopardize the real-world deployment of the system. To tackle this problem we propose the use of an all-pairs approach, where all possible combinations of sensing terminal pairs are used. This allows us to obtain a very rich dataset with fewer sensing terminals, resulting in a reduced number of wires for the overall sensor.

The number of sensing pairs (and thus signals we harvest) is generally quadratic in the number of terminals. More specifically, for our resistive sensor the number of signals collected for n terminals under this modality can be expressed as $\frac{1}{2}\,\frac{n!}{(n-2)!}$ or equivalently $\frac{1}{2}(n^2 - n)$. In the case of our optical sensors, the number of signals extracted is the product between the number of LEDs and the number of photodiodes. To extract the largest number of signals possible, we should keep the number of emitters and receivers equal, hence for n total terminals, $\frac{n}{2}$ would be LEDs and $\frac{n}{2}$ would be photodiodes, resulting in the number of collected signals to be $\frac{n^2}{4}$. Because in our optic sensors a sensing terminal has a specific role, the number of possible sensing pairs combinations is lower when compared to the piezoresistive sensor. Moreover, the resistive sensor only requires one wire per sensing terminal, compared to the two wires required on the optical sensors for each LED and photodiode. As we will detail in subsequent chapters, the optical transduction method still offers significant advantages over piezoresistivity.

To further reduce wiring, we propose the use of time-multiplexing to sample all of our signals/sensing pairs. Placing local multiplexers wired to the sensing terminals allows us to use binary addressing. For example, a 32 channel multiplexer can service 32 sensing terminals but we only need 5 wires to select an individual channel. With the use of modern microcontrollers we can switch and sample different sensing pairs at very high speeds.

3.2 A data-driven method

One of the trade-offs in our method is that of data processing. We strive for rich, high dimensional tactile signals that capture contact events through the use of spatially overlapping signals. But how do these signals relate to measurable contact parameters such as normal force? By our signal pair design, it is not possible to calibrate a single signal to a traditional contact parameter. While each individual signal must be strain sensitive in the transduction method of choice, only a larger signal set contains enough information to describe the contact event. In this sense, our method loses interpretability when compared to traditional taxel-based methodologies where signals can be calibrated to a physical quantity.

Building an analytical model of how this rich signal set is affected by mechanical strain applied to a soft material is a daunting task; furthermore, any such model would depend on knowing the exact locations of the terminals in the sensor, thus requiring very precise manufacturing. Qualitatively, we expect that the intensity of the collected signals is directly related to the magnitude of the applied strain, whereas the pattern of which pairs respond is directly related to the location of the applied strain.

We thus use a purely data-driven method to directly learn the mapping between the signal set extracted from the sensor and our variables of interest. We collect training data using a set of indentations of known characteristics. Throughout this dissertation we focus mainly on learning mappings for contact localization and indentation depth or force. In our optical sensors we also investigate the ability to discriminate between a finite set of possible indenter shapes.

Abandoning the use of analytical models means we can formulate this method in a generic way, using any transduction methods of our choice regardless of the availability of a model. Also, it relaxes the manufacturing precision (which in turn can help cut costs) by allowing us to freely distribute sensing terminals inside an soft material since the forward model is learned based on collected data. However, the data collection process requires specialized equipment to collect enough labeled data as well as a significant time investment. Scalability is also a concern when collecting labeled data, with the amount of data needed growing exponentially as we attempt to predict more parameters simultaneously. Multitouch situations are a good example of this problem. Training for a single contact is not an issue, but training for two or three simultaneous contacts becomes harder to realize: we need instrumentation to precisely control the indentations in several locations at the same time, and the number of different combinations of contact locations (and forces applied at each location) quickly grows to the point where it becomes unfeasible to sufficiently explore the feature space. Our view is that the signal set extracted from our sensors contains a rich description of most interesting contact parameters that manifest as measurable surface deformation, but extracting this information with a supervised learning approach can prove challenging.

An interesting alternative is to forgo data collection altogether, and to use this data-rich method for end-to-end, model-free sensorimotor learning. These methods learn a direct mapping from raw sensor data to motor commands. Any intermediate representations of the sensor data are learned at the same time as the task itself, without ground truth other than the general reward signal related to task success. Likely, the use of unsupervised learning can be also useful to learn lower dimensional representations of our high dimensional signal output. In a way, such approach can make better use of the information embedded in our signals, because we do not force the network to learn hand-picked features, but instead have it find the most relevant features related to the task. While we do not expressly explore these possibilities in this dissertation, we believe there is great promise in using our sensors as platforms for this type of approach.

Overall, we believe the trade-offs our our data-driven methodology are worth it as they become enablers of tactile sensors with many desirable characteristics such as providing extensive coverage of curved surfaces, high accuracy in contact localization and force detection with a low wire count and cheap manufacturing. In the following chapters, we present concrete implementations of these concepts using three transduction methods, based on piezoresistance (chapter 4), MEMS pressure transducers (chapter 5) and optics (chapters 6 through 8).

Chapter 4: Localizing touch on a piezoresistive elastomer

In this chapter we introduce our first tactile sensor prototype using the concept of spatially overlapping signals. For this sensor we decided to use a piezoresistive elastomer onto which we can embed several electrodes to measure resistance changes in the material.

With the use of piezoresistivity as a transduction method, a given sensing terminal can be paired up with any other to obtain a resistance measurement. Because each terminal is effectively an electrode, only a single wire is needed per terminal. As a result, a sensor with these characteristics can provide a large number of signals with minimal wiring, a desirable trait for integration into robot hands. Another attractive quality of this approach is the fact that the piezoresistive material can be molded into arbitrary geometries. Furthermore, we can embed electrodes anywhere in this volume which could allow the tuning of spatial resolution, as more electrodes can be added in areas like fingertips.

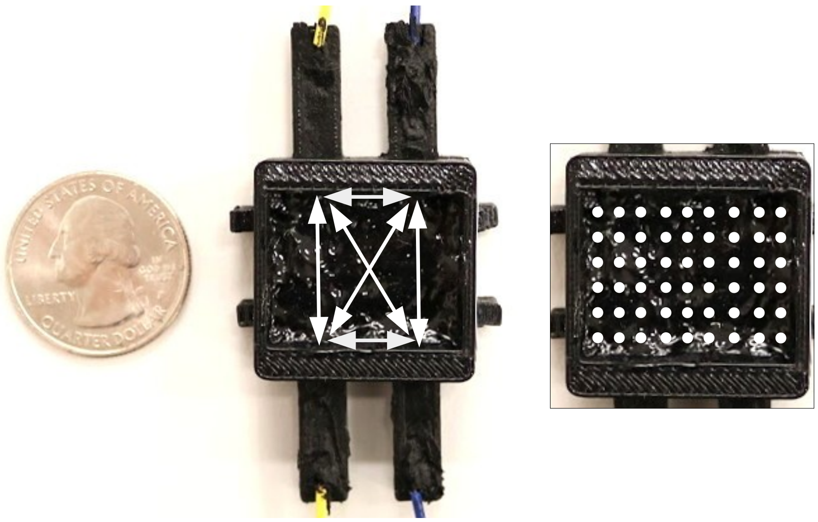

Figure 4.1: Proof of concept design, with a rectangular volume of piezoresistive elastomer and four connected electrodes. We measure resistance change due to indentation between all electrode pairs (illustrated by arrows) and use grids of known measurements (illustrated on the right) to learn a mapping from these signals to indentation location.

To evaluate our method, we build a prototype illustrated in Figure 4.1. A continuous volume of piezoresistive polymer is poured into a mold with 4 electrodes, which results in 6 possible sensing pairs. For an indentation anywhere on the surface of this volume, we measure resistance change in response to strain between all the pairs of electrodes in the area. Because the change in resistance is local to the location where strain was applied, we expect that each location produces a certain signature in terms of the signal pattern that arises when strain is applied. We do not attempt to model this change in resistance, but instead propose the use of purely data-driven techniques to learn a mapping between these 6 resistance values to the contact location directly from indentation tests. We will show that this mapping can be effectively learned from data. The result is a compliant sensor with high spatial resolution that can conform to complex surfaces, which facilitates future integration into robot hands.

4.1 Sensor design and construction

Our overall approach to achieving high spatial resolution starts with a continuous volume of piezoresistive material, with a number of embedded electrodes. Molding a silicone elastomer into the desired shape allows us to embed electrodes while the mixture is viscous, and keeps open the possibility of covering complex, non-flat surfaces in the future. To achieve piezoresistance for our silicone, we use the well established method of dispersing a conductive filler, as detailed below. We then describe the switching circuit developed so that we can sample the change in resistance between any pair of electrodes at high rates.

Building a piezoresistive material

We disperse multiwall carbon nanotubes (MWCNT, purity: 85%, Nanolab Inc.) into polydimethylsiloxane (PDMS, Sylgard 184, Dow Corning), a two-part silicone elastomer. The key aspect of this process for achieving piezoresistance is choosing the appropriate ratio of conductive filler to elastomer. According to the commonly used percolation theory, the conductivity of the composite w.r.t. filler ratio displays an inflection near a point referred to as the percolation

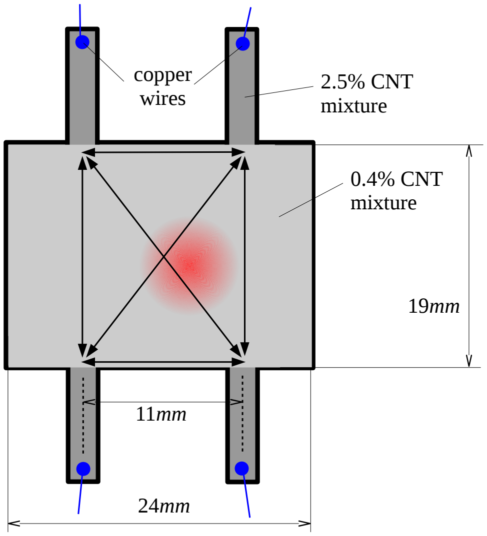

Figure 4.2: Design of the proof of concept sensor used for the experiments in this paper. The rectangular center is filled with piezoresistive PDMS/CNT mixture. Side channels are filled with a conductive mixture with higher CNT ratio in order to mechanically isolate copper wire contacts from indentations. For a given indentation (illustrated by red circular pattern) we measure the change in resistance between all six electrode pairs (illustrated by arrows on the surface of the volume).

threshold. A composite with that ratio will also display the most pronounced piezoresistive effect [124]. In order to find the percolation threshold of our materials, we built and tested a series of sensors with the concentrations of MWCNTs from 0.2wt.% to 5wt.%. We found that the most pronounced change in conductivity occurred around the threshold of 0.4wt.% filler, which we used in all subsequent experiments.

In order to achieve uniform distribution of carbon nanotubes within PDMS, we use a chloroform as a common solvent, an approach referred to as the solution casting method [125]. First, we add chloroform and MWCNT into a beaker and sonicate with a horn-type ultrasonicator in a pulse mode with 50% amplitude for 30 min to evenly disperse MWCNTs into chloroform. After that, we pour PDMS into the beaker (at chloroform:PDMS weight ratio of 6:1 or more to reduce the viscosity of the whole mixture), stir the mixture for 5 min to diffuse the PDMS into the solvent, and then sonicate again for 30 min to disperse the MWCNTs into PDMS. We then heat the mixture at 80° C for 24 hours to evaporate the chloroform. After adding the curing agent, the mixture is ready to be poured into the mold; for the experiments presented here we empirically selected a curing agent to PDMS ratio of 1:20. Finally, the sensor is finished after curing in an oven at 80° C for 4 hours.

Our goal for this design is to measure resistance through a volume between multiple pairs of terminals. However, in order to isolate piezoresistive effects from mechanical changes at the contacts due to indentation, we mechanically separated the wire contacts from the piezoresistive sensor placed under indentation tests. We extended a number of 30 *mm* side channels from the sensor, each filled with a CNT-filled PDMS mixture with a higher concentration of 2.5wt.% We then embedded copper wires directly into the mixture at the end of these channels (Figure 4.2). The mixture with the ratio of 2.5wt.% has no piezoresistive characteristics and its conductivity is close to that of the copper wires; thus, the mixture with the ratio of 0.4wt.% located at the center of the mold dominates the overall conductivity.

Sampling circuit

The main objective for our sampling circuit is to measure the change in resistance between all pairs of electrodes/terminals that occurs as a result of some strain being applied to our sensor material. We found that this change can be around 5% of the nominal value at rest. Furthermore, every pair of terminals will have different resistance values at rest. It is also important to be able

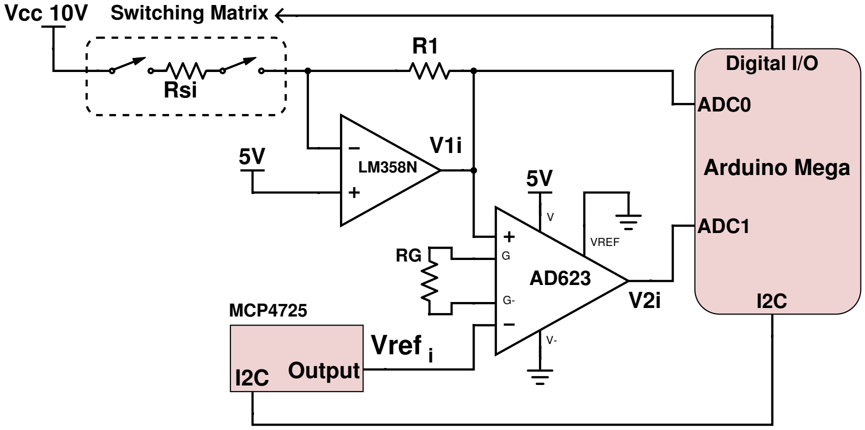

Figure 4.3: Measuring circuit. For every terminal pair with a resistance R_{si}, we take a measurement of V_{1i} with the sensor at rest. This measured voltage is then reproduced on V_{ref_i} by means of a digital to analogue converter such that we only amplify the change on V_{1i} when the sensor is indented.

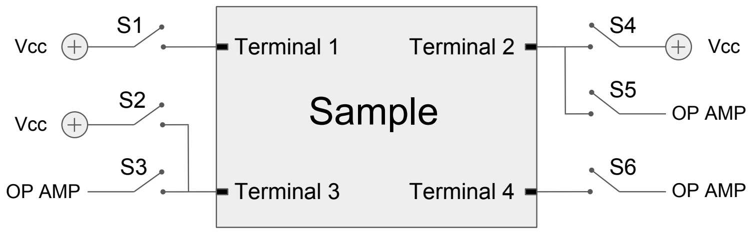

Figure 4.4: Switching Matrix structure. All six switches are controlled with digital signals from our microcontroller. This configuration allows us to measure the resistance change across any pair of terminals. The switches must be closed such that we always connect one terminal to Vcc and the remaining one to the inverting input of the operational amplifier.

to sensor these relatively small changes in resistance at a high enough rate such that a set of all measurements across terminals can be representative of the instantaneous strain applied.

Consider R_{si} to be the resistance across the i-th terminal pair that we are interested in measuring, $i \in \{1, 2, 3, 4, 5, 6\}$. As shown in Figure 4.3, we use a first stage with a simple operational amplifier in inverting configuration in a way that we guarantee an output V_{1i} between 0 and 5 volts such that it can be directly measured by our microcontroller analogue to digital converter module (ADC). The output of this stage, V_{1i}, is given by equation 4.1

$$V_{1i} = 5\mathrm{V} - 5\mathrm{V}\left(\frac{R_1}{R_{si}}\right) \tag{4.1}$$

Since the change in the resistance R_{si} can be very small, it stands to reason that the change in our output voltage V_{1i} from this first stage will also be small. It is worth noting that the value of R_1 has to be smaller than any of our values R_{si}, and the sensitivity of V_{1i} with respect to R_{si} changing increases as the value of R_1 is closer to those of R_{si}.

Because we are not interested in the absolute value of V_{1i} but only in its change over time when strain is applied, we take a baseline measurement of V_{1i} when the sensor is undisturbed. These baseline measurements are then used as the values of V_{ref_i} that we hold on the negative input of an instrumentation amplifier for the second stage of the circuit. This allows us to remember the undisturbed value of V_{1i}, compare it with the current one, and amplify that difference. The voltage V_{ref_i} is provided in our circuit by a digital to analogue converter (DAC, MCP4725).

Our switching matrix is shown in Figure 4.4, where we have six switches total, allowing us to measure across any combination of terminals, T1 through T4. Each one of these terminal pairs has a value of R_{si}, where $i \in \{1, 2, 3, 4, 5, 6\}$. The overall circuit delivers the set of all six V_{2i} values every 25 milliseconds, resulting in a 40Hz sampling frequency. The main bottleneck for this sampling frequency is the speed of the analog-to-digital converter (ADC) in the Arduino Mega we utilize. A faster ADC module would increase our sampling rate although this is beyond the scope of this prototype.

4.2 Data collection

To collect training and testing data, we indent the sensor at a series of known locations and to a known depth. We place the sensor on a planar stage (Marzhauser LStep) and indent vertically using a linear probe (see Figure 4.5). We use a hemispherical indenter tip with a 6 *mm* diameter printed in ABS plastic. All indentations are position-controlled relative to the surface of the sensor, which we determine manually by lowering the probe until we observe contact.

For indentation locations, we use two patterns. The *grid indentation pattern* consists of a regular 2D grid of indentation locations, spaced 2 *mm* apart along each axis. However, the order in

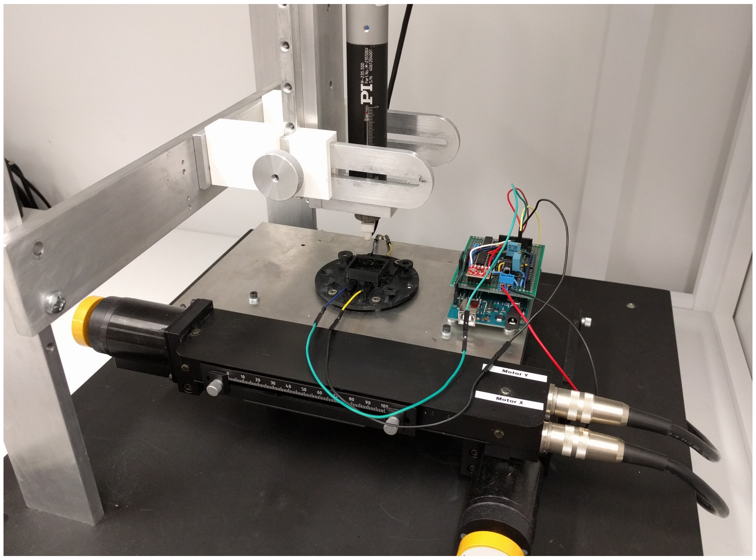

Figure 4.5: We collect sensor data using a planar stage to move the sensor relative to a vertically fixed linear probe which handles the position controlled indentations

which grid locations were indented was randomized. This is in contrast with the *random indentation pattern*, where the locations of the indentations were sampled randomly over the surface of the sensor (not following any pattern).

For each indentation location, we measure the signal from each pair of electrodes at multiple indentation depths. Each such measurement resulted in a tuple of the form $\Phi_i = (x_i, y_i, d_i, r_i^1, .., r_i^6)$, where x_i and y_i represent the location of the indentation, d_i is the indentation depth, and $r_i^1, .., r_i^6$ (also referred to collectively as $\mathbf{r}_i$) represent the change in the six resistance values we measure between depth d_i and depth 0 (the probe on the surface of the sensor). These tuples are used for data analysis as described in the next section.

4.3 Localization results

Our main goal is to learn the mapping from all terminal pairs readings $\mathbf{r}_i$ to the indentation location (x, y). To train the predictor, we collected four datasets in regular grid patterns, totaling 216 indentations. For testing, we collected a dataset consisting of 60 indentations in a random pattern. All indentations used here were performed to a depth of 3 *mm*, or 50% of the total depth of the sensor, which represents an approximate force of 12 N. The metric used to quantify the success of this mapping is the magnitude of the error (in mm) between the predicted indentation position and ground truth. In our analysis below, we report this error for individual test points, as well as its mean, median and standard deviation over the complete testing set.

The baseline that we compare our results against includes a “Center Predictor” and a “Random Predictor”. The former will always predict the location of the indentation on the center of our sensor, and the later will predict a completely random location within the sensor surface. The

Table 4.1: Prediction accuracy for indentation location

Predictor	**Median Err.**	**Mean Err.**	**Std. Dev.**
Center predictor	5.00 mm	5.13 mm	2.00 mm
Random predictor	6.30 mm	6.70 mm	3.80 mm
Linear regression	1.75 mm	1.75 mm	0.83 mm
Laplacian ridge regression	**0.97 mm**	**1.09 mm**	**0.59 mm**

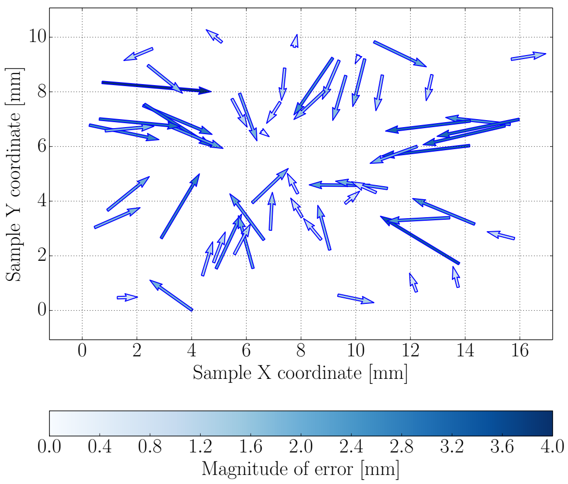

a) Linear regression

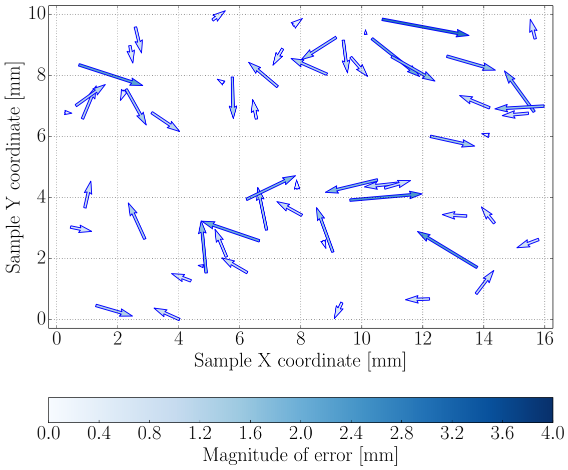

b) Laplacian ridge regression

Figure 4.6: Magnitude and direction of localization errors for Linear and Laplacian ridge regressions. Each arrow represents one indentation in our test set; the base of the arrow is at the ground truth indentation location while the tip is at the predicted location.

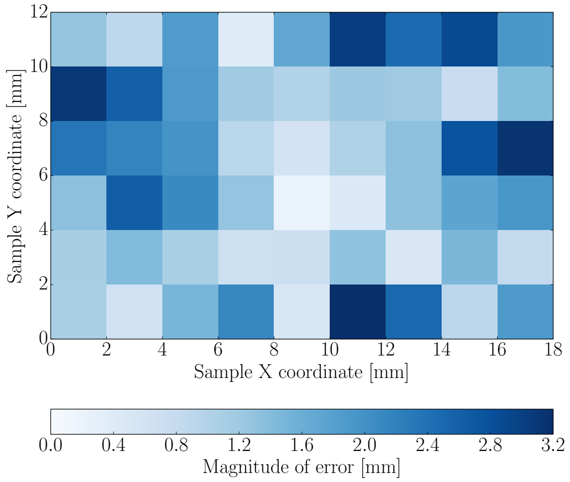

a) Linear regression

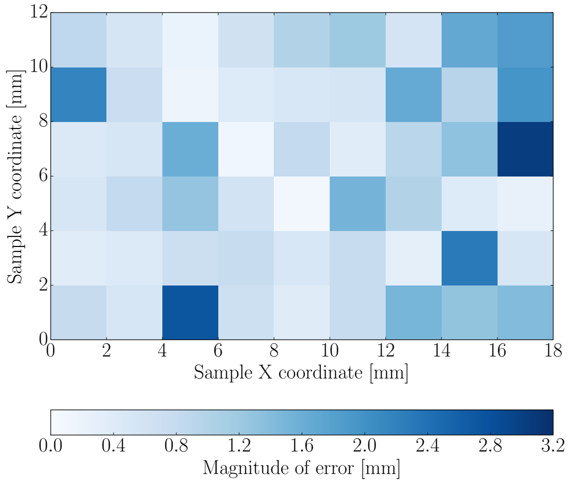

b) Laplacian ridge regression

Figure 4.7: Heatmap of localization error magnitude based on indentation location for Linear and Laplacian ridge regression.

useful area of our sensor is 16 *mm* by 10 *mm*; on our test set, the Center Predictor produces a median error of 5 *mm*, while the random predictor, if given a large test set, converges on a median error of above 6 *mm*.

We first attempted Linear Regression as our learning method. The results were significantly better than the baseline, with a median error of under 2 *mm*. Still, visual inspection of the magnitude and direction of the errors revealed a circular bias towards the center that we attempted to compensate for with a different choice of learning algorithm. The second regression algorithm we tested was Ridge Regression with a Laplacian kernel. The Laplacian kernel is a simple variation of the ubiquitous radial basis kernel, which explains its ability to remove the non-linear bias noticed in linear regression results. In this case, we used the first half of the training data for training the predictor, and the second half to calibrate the ridge regression tuning factor λ and the kernel bandwidth σ through grid search.

The numerical results using both of our predictors, as well as the two baseline predictors, are summarized in Table 4.1. These results are aggregated over the complete test set consisting of 60 indentations. Linear regression identifies the location of the indentation within 2 mm on average, while Laplacian ridge regression ($\lambda = 2.7e^{-2}$, $\sigma = 6.15e^{-4}$) further improves this results achieving sub-millimeter median accuracy.

In addition to the aggregate results, Figure 4.6 illustrates the magnitude and direction of the localization error for the entire test set. To characterize localization error uniformly over the entire sensor, we also performed a separate analysis where the test set also consisted of a regular grid of indentations (in this case, we used only three such grids for training and the fourth one for testing). This allows us to plot localization error as a function of position on the surface of the sensor; the results are shown in Figure 4.7. Again the predictor using Laplacian ridge regression achieves high accuracy throughout most of the sensor's area, with larger errors occurring on the edges. We believe that this pattern can be explained by the fact that an indentation closer to the center is likely to produce a meaningful signal for more electrode pairs compared to an indentation at the edge.

4.4 Discussion

In this chapter we demonstrate the first piezoresistive sensor that achieves submillimeter median accuracy in determining contact position on a 160 mm^2 surface using a purely data-driven approach. This is achieved using only four wires that connect to the sensor, by measuring resistance change between six electrode pairs, and without relying on a flat rigid substrate or circuit board.

This proof of concept study is meant to illustrate the feasibility of our spatially overlapping signals methodology and its benefits over traditional approaches; namely its potential to provide contact rich data using fewer wires. In this prototype, we show a localization error of approximately 1 *mm* over an effective sensing area of 10 by 16 *mm*, the equivalent of 160 individual taxels. Even assuming worst-case accuracy throughout the sensor, we can still locate contact within 3 *mm*, the equivalent of 15 taxels, using only four wires.

While this high spatial resolution with such a low wire count is promising, we found a number of critical problems that hinder the practical application of this sensor. The mechanical interface between the terminals and the piezoresistive elastomer significantly affects resistance measurements; in this proof-of-concept prototype, we used side channels with highly conductive elastomer to isolate the sensor, but this complicates future integration in robot fingers. We also found that the sensor exhibits significant hysteresis over time scales on the order of seconds (see Figure 4.8), as well as signal drift over longer time scales. We mitigate this here by using the resistance values at depth 0 (just before touching) as a baseline that is subtracted from all signals collected during that indentation, and by always indenting to a known depth. By extension, the instability of the collected signals due to hysteresis, prevents the possibility of reliably discriminating the contact force, a capability of critical importance for a complete tactile feedback system.

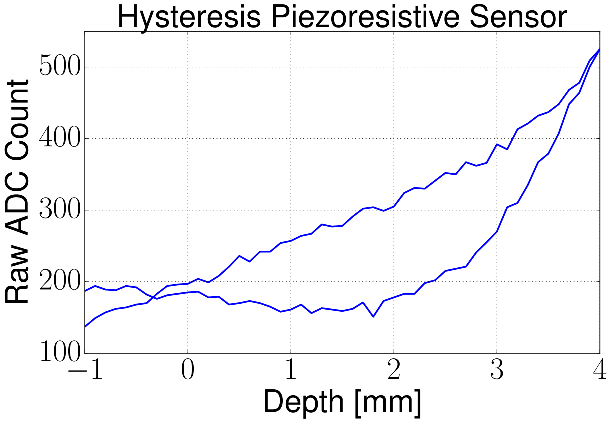

Figure 4.8: The response of a single terminal pair to an indentation up to 4 *mm* using a 6 *mm* diameter hemispherical indenter shows significant hysteresis.

Based on the results presented on this chapter, our piezoresistive sensor prototype has provided us with an initial validation of our method but ultimately falls short of our requirements for deployment on a fully integrated robotic finger. Ultimately, a data-driven method is only as good as the quality of the data we can extract from the sensor. Signals that present high levels of noise and hysteresis cannot be used to build a reliable mapping for contact parameters. With improvements in the manufacturing of piezoresistive materials to address some of these issues, overlapping piezoresistive signals could hold significant promise for collecting rich contact data using very few terminals. In subsequent chapters we explore other transduction methods, such as MEMS pressure transducers and optics, to build new sensor prototypes and evaluate their potential when used within our framework.

Chapter 5: Overlapping strain signals on curved surfaces

In this chapter we aim to provide tactile sensing over a three dimensional surface, such as a spherical dome, and localize contact events anywhere along this surface. To achieve this goal, we decide to use a proven, stand-alone pressure transducer like the Takktile [54]. We demonstrate this approach on a hemispherical body, a "tactile dome", with multiple Takktile pressure transducers embedded deep in the urethane rubber that makes up this soft volume (see Figure 5.1).

The Takktile is an inexpensive, highly sensitive, tactile pressure transducer based on commercial MEMS barometers chips. The chips include tightly integrated instrumentation amplifiers, analog-to-digital converters, temperature sensing, and control circuitry that provides excellent signal quality over standard digital bus interfaces. The barometer is converted into a touch transducer by casting a rubber urethane over the chip such that any pressure on this external rubber encapsulation is transmitted into the internal strain gauges. In our prototype we use Takktile chips that have already been casted, but embed them deeper into a larger volume of the same type of rubber.

For this prototype, we forgo the "sensing pairs" implementation since our sensing terminals are

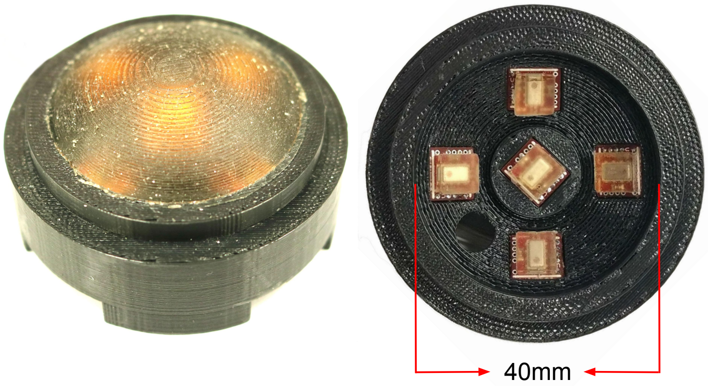

Figure 5.1: Example of a soft volume embedded with individual pressure transducers. This tactile dome has a hemispherical surface and five embedded Takktile pressure transducers. We use data driven techniques to localize touch across its three dimensional surface.

monolithic pressure transducers. As a result, the potential number of signals collected from such a sensor is much lower: we can only collect one signal per Takktile pressure transducer. For this reason, we assume that the location (or “configuration”) of the sensing terminals inside the soft material is of particular importance. However, given the data-driven nature of our method (with no analytical model), it is hard to predict the final performance of the sensor at design time: we need to build the sensor, collect training data and only then we can evaluate the localization performance by training a regressor.

To address this, we implement a quasi-static finite element analysis (FEA) simulation which we show is a reliable predictor for the behavior of real sensors. The FEA simulation generates synthetic datasets which we feed into our machine learning algorithm to predict the performance of a given sensor configuration. This enables us to test different configurations virtually without having to build a physical sensor. We demonstrate this by testing ten different sensor configurations in simulation. Moreover, we build two of the simulated models into physical tactile domes for comparison and validation.

Our key intuition is that configurations that favor cross-talk will provide better localization: if an indentation anywhere on the dome’s surface produces a meaningful signal in as many Takktiles as possible, such a “signature” can be used to determine the location of the indentation using data-driven techniques. This can be considered an instance of super-resolution: we are trying to engineer overlapping receptive fields for each Takktile such that we can perceive stimuli in finer detail than if we treat each pressure transducer as an stand-alone taxel.

5.1 Tactile dome design

The tactile dome is designed to represent a generic, three dimensional surface such as an anthropomorphic fingertip or palm. A 3D-printed base made of ABS material acts as a mounting structure for both the soft volume and the Takktile pressure transducers. A second piece mates with this base to create the casting mold with a spherical surface. The useful area of the sensor is the section of a 54 *mm* diameter sphere subtended by a cone with a 90 degree aperture, resulting in a surface of approximately 1300 mm^2. This design is illustrated in Figure 5.1.

The tactile dome is cast on the base using Vytaflex 20, the same rubber urethane used on the Takktile to create a cohesive bond. Prior to casting, the solution is degassed to ensure that the tactile dome has consistent, isotropic properties. The two constructed physical sensors have a hole in the ABS base where the solution is poured while the assembly is upside down. The solution is cured for 24 hours at room temperature and then placed in an oven at 65° C for 8 hours. The hole used to pour the solution is then plugged using a matching ABS piece and epoxy.

We aim to find a sensor configuration that achieves high accuracy for touch localization using only five Takktile pressure transducers. To this end, we explore 10 possible configurations, using both simulation and fabrication of real sensors. We will discuss all of these configurations in detail in the following sections. First we introduce our data collection and analysis protocols below, which are the same regardless of the sensor configuration.

5.2 Data collection

Our goal is to find a data-driven mapping between the five pressure readings and the location of an indentation. To collect training data, we use an indenter machine with five degrees of freedom (DOF) capable of probing at specified locations and depths along the dome's surface with varying angles from the surface normal (Figure 5.2). The indenter machine is composed of a planar stage (Marzhauser LStep) where we attach our tactile dome on top of a rotating base. We mount a position controlled linear actuator (Physik Instrumente M-235-5DD) on a revolute joint directly above the dome. The linear actuator is equipped with a 6*mm* diameter aluminum hemispherical tip. The only unaccounted DOF is a revolute joint around the tool tip axis. In this study all indentations are performed with the linear actuator positioned normal to the dome's surface.

To collect training data, we sample the tactile dome at equidistant locations along its surface. To achieve this uniform distribution over a spherical surface, we use a mapping scheme [126] to project a two dimensional regular grid (A, B) onto the dome's hemispherical surface (x, y, z). Using $A, B \in [-15, 15]$ results in a mapping that almost completely covers our three dimensional

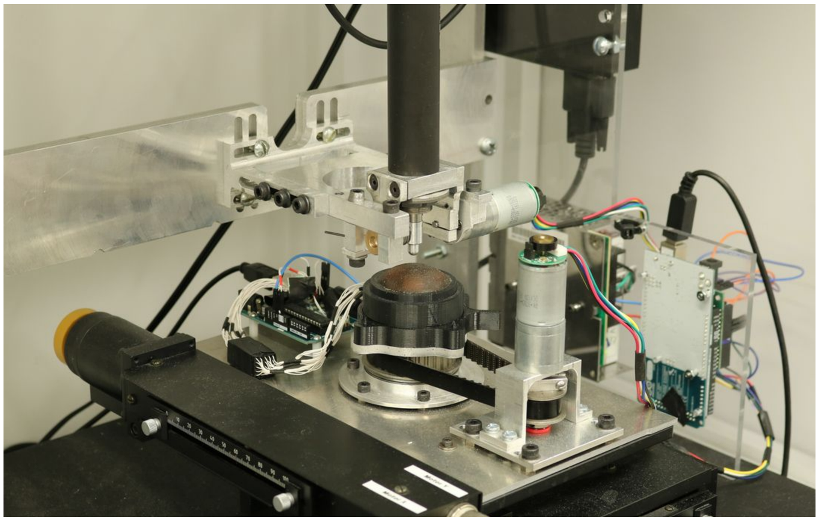

Figure 5.2: Our indenter machine is composed of a planar stage and a linear actuator. The tactile dome can rotate on top of the planar stage and the linear actuator can pivot up to 60 degrees on an axis parallel to the stage. These additional degrees of freedom were built such that the tactile dome can be indented at any point with any angle with respect to the surface normal.

surface. Note that this (A, B) space is dimensionless. For more information about this mapping, refer to Appendix A. We use a 16x16 regular grid, hence we sample along 256 different positions on the surface of the dome for training. At each location, the probe is positioned normal to the surface and a first “non-touch” data point is recorded before the linear actuator tip contacts the dome’s surface. Subsequently, the actuator indents the dome and records data at the predefined depths from 0 to $3mm$ in $0.5mm$ intervals.

To collect a test dataset, we follow an identical procedure except indentation locations are randomly sampled from our two dimensional (A, B) space. We collect data on 100 random locations. The test dataset locations, while generated randomly within our (A, B) space, are repeated for all 10 sensor configuration cases (both real and simulated) for consistency.

For each measurement i, we record the data in a tuple of the form $\Phi_i = (A, B, d_i, r_i^1, ..., r_i^5)$ where (A, B) is the location of the indentation before being mapped to the dome’s surface, d_i is the depth of the measurement, and $r_i^1, ..., r_i^5$ are the readings of the five pressure transducers. These tuples are used as described in section 5.4.

5.3 Simulation

In addition to the methodology described above for building and using physical sensors, we have developed a corresponding simulation framework based on finite element analysis (FEA). The purpose of developing a simulated model of our tactile dome is to have the ability to iterate and evaluate sensor configurations to improve the localization performance without the need to build the physical tactile dome.

In the simulated case, we use a quasi-static, ABAQUS Standard FEA to generate both training and testing data. The indentations are performed with a 6*mm* diameter, hemispherical, rigid body at the same locations as on the physical tactile dome, normal to its surface. The indenter interacts with the tactile dome's surface with an estimated friction coefficient of 0.8. We perform a uniaxial tensile test to achieve accurate material properties for the specific batch of Vytaflex 20 used to fabricate the physical dome. This experimental stress-strain data is input into ABAQUS and the software's Marlow curve fitting model predicts the material properties.

To simplify the model, we make the following assumptions:

- The tactile dome's polymer is perfectly bonded to all of the components it interfaces with during casting.
- The compliances of the ABS base, Takktile housing, and Takktile circuit are ignored. These

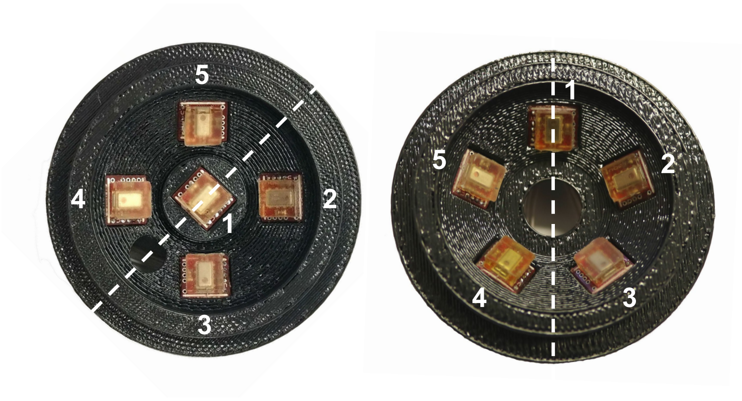

Figure 5.3: Top view of two distinct sensor configurations inside a tactile dome, each showing a dotted symmetry line and numbering for individual pressure transducers.

components are treated as infinitely stiff compared to the polymer.

- The Takktile chip samples pressure at its air-vent hole, which is an opening to the barometer's pressure-sensing Wheatstone bridge. The elastomer is assumed to have the same properties as Vytaflex 20.

The first two assumptions enable us to exclude the ABS base, Takktile housing, and Takktile circuit from the simulation in order to reduce computational time and complexity. To compensate, a zero-displacement constraint in the X-Y-Z directions is applied on the surfaces where the polymer interacts with these components. It should be noted that these surfaces are not fixed in rotation to ensure that the simulation is not over-constrained.

To reproduce the interaction between the tactile dome and the Takktile air-vent hole, five thin, cylindrical bodies are attached to the dome via a "tie" constraint, representing perfect bonding of Vytaflex 20. The opposing cylindrical faces are fixed in the X-Y-Z directions to mimic the

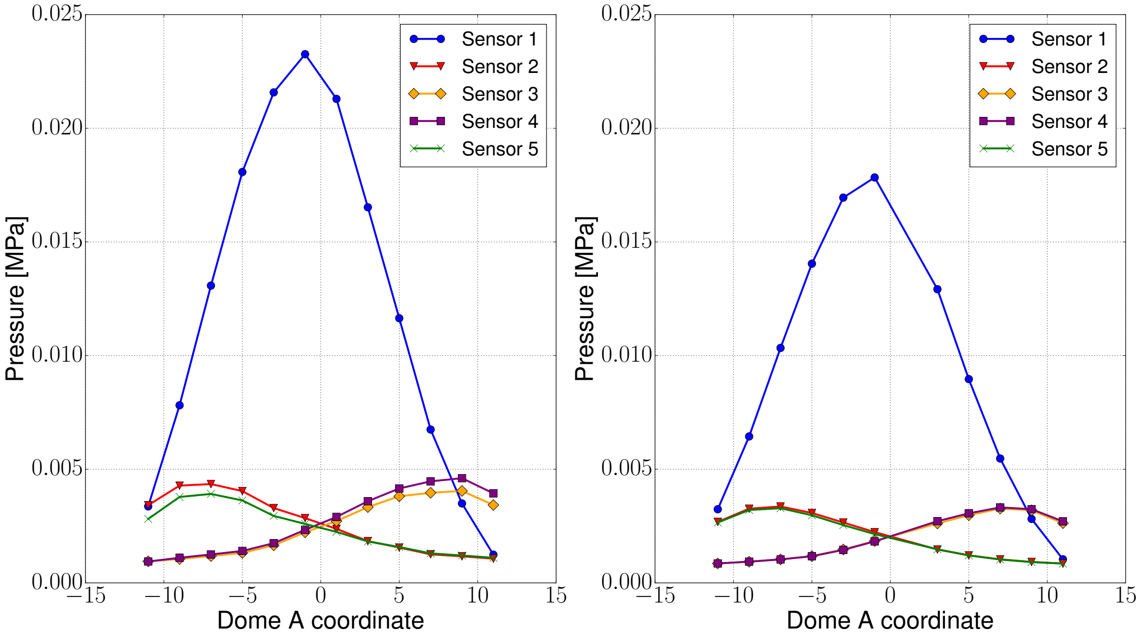

(a) C3D4H mesh

(b) C10D4i mesh

Figure 5.4: Comparison between simulations ran using a C3D4H mesh (5.4a) and a C10D4i mesh (5.4b) on Case 1. The graph represents the pressure distribution among the five Takktile pressure transducers as we indent along the symmetry line. Both graphs show similar trends with slightly different absolute values for the reported pressure.

attachment to the Takktile's internal strain gauge. The cylinders allow us to sample at a location that is not a boundary condition such that we generate a realistic output. We sample pressure data at the surface between the cylindrical bodies and the tactile dome.

In order to shorten the computational time required for the solution to converge, data is collected over half of the sensor and mirrored about the line of symmetry. The symmetry line corresponds in (A, B) space to the line A=-B for configurations with a central Takktile pressure transducer and to $A = 0$ for configurations with all Takktile pressure transducers arranged in a circumference (see Figure 5.3).

The dome and five bodies are modeled with a first-order mesh with hybrid elements due to the incompressible properties of Vytaflex 20 and the curved geometry. We ran a mesh convergence study using Case 1 and determined that a 10-node, C10D4i mesh yields similar trends as a 4-node C3D4H mesh (Figure 5.4). Additionally, the average time to simulate a single indentation using the C10D4i mesh is more than 10 times longer than using a C3D4H mesh; therefore, we use the 4-node mesh in order to decrease the simulation run time.

5.4 Data-driven localization algorithm

The goal of our localization algorithm is to learn the mapping from Takktile pressure signals $(r^1, ..., r^5)$ to the location of the indentation (A, B). For a given sensor configuration, we train a regressor to learn this mapping using a training dataset containing 256 datapoints, each corresponding to one location in the (A, B) grid. We then test performance on a test dataset, containing data from indentations at 100 random locations. For consistency, we use the same test set locations for all sensor configurations.

We use this procedure in exactly the same way on both physical and simulated domes. Real and synthetic data are treated equally, except for the fact that simulated training data is mirrored about the symmetry axis (to save simulation time), whereas real data is collected over the entirety of the (A, B) grid.

The predictor we use is a kernelized ridge regressor with a laplacian kernel. We have found that

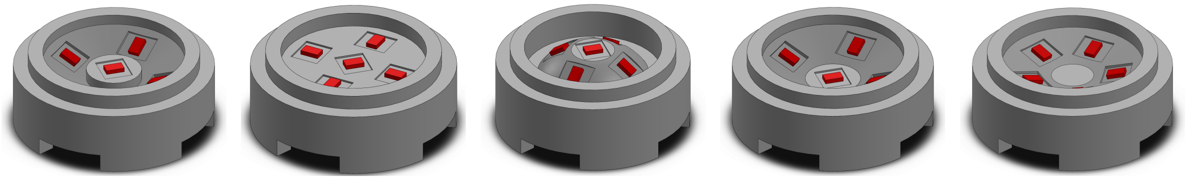

Case 1: Central 25° with platform Case 2: Central 0° Case 3: Central -25° Case 4: Central 25° without platform Case 5: Ring 15°

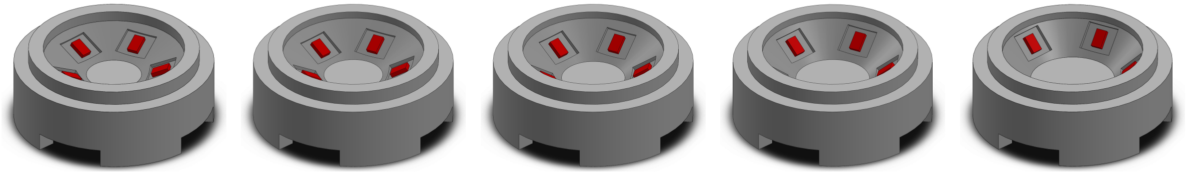

Case 6: Ring 25° Case 7: Ring 30° Case 8: Ring 35° Case 9: Ring 40° Case 10: Ring 45°

Figure 5.5: Trimetric view of all dome design cases. Takktile pressure transducers are shown in red color and the volume of soft material is not represented.

the laplacian kernel provides better results compared to the radial basis function kernel (comparison data not included here), and thus used the laplacian kernel for all results shown in this paper. We also perform cross-validation using the k-fold method with $k = 5$ and shuffling the data on each fold. The regressor hyper-parameters (the ridge regressor regularization term α and the laplacian kernel parameter γ) are chosen through an exhaustive grid search of 400 combinations: 20 values in logarithmic space for both α and γ ranging from 10^{-5} to 10^{1}. The metric used to decide on the best hyper-parameter combination is to minimize the median error of the localization prediction. All results are obtained using the scikit-learn Python package implementation of the kernelized ridge regressor.

5.5 Exploration of sensor configurations using simulation

Our data-driven approach allows complete freedom in choosing sensing terminal configurations inside the tactile dome and the simulation framework allows us to test and compare different configurations without building physical sensors. The space of possible configurations is so large that the process of selecting configurations to test must still be guided by intuition. In this study, we test 10 possible configurations, shown in Figure 5.5. The performance of each case is summarized in Table 5.1, showing median, mean and standard deviation for localization error in cartesian

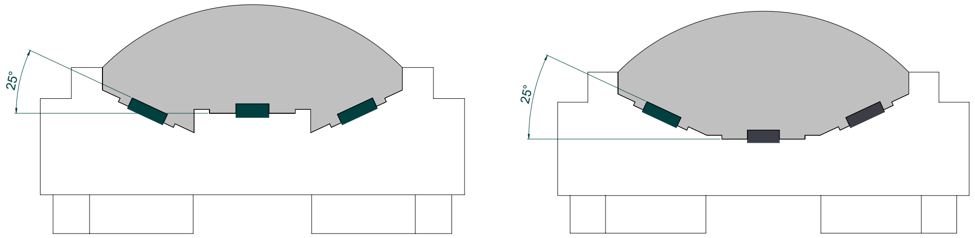

(a) Base with platform

(b) Base without platform

Figure 5.6: Cross section of the dome illustrating a base (white) with platform (5.6a, corresponds to Case 1) and one without platform (5.6b, corresponds to Case 4). The mounting angle for both cases is positive 25 degrees. Takktile pressure transducers are shown in black and the soft material is shown in gray.

coordinates over the 100 test indentations using the data corresponding to a depth of $2mm$. Localization error plots for each configuration are also presented in Figure 5.7 in (A, B) space for a more convenient 2D representation.

Our initial configuration (Case 1) is based on the intuition that we want to promote cross-talk: we want any given indentation to result in some measurable signal in as many Takktiles as possible. We define the “mounting angle” of the Takktile as the angle of the pressure transducer relative to the floor where the dome rests (see Figure 5.6). The angle is considered positive if the Takktile normal points towards the dome center. By this convention, we hypothesize that a configuration with positive mounting angles (concave) will provide better cross-talk when compared to one with negative mounting angles (convex). On a convex mounting scheme, the strain caused by an indentation on the edge of the dome can hardly propagate to produce a meaningful signal on Takktiles on the other side of the dome.

We test this hypothesis in Cases 1 through 3. These three cases use the same “central” configuration, but with mounting angles of -25, 0 and 25 degrees. For Case 1, we raise the central Takktile such that its distance to the dome’s surface is reduced. This is to adjust for the Takktile’s decrease in sensitivity as they are embedded deeper in the soft volume [54]. As a reference, this distance for Case 1 is equivalent to that of Case 2 (for the central Takktile). Our results confirm our initial hypothesis, with Case 1 showing the highest accuracy at $1.5mm$ median error. Moreover, Case

Table 5.1: Localization accuracy results

Case	**Median Err.**	**Mean Err.**	**Std. Dev.**
Case 1 simulation	1.5 mm	2.0 mm	2.2 mm
Case 2 simulation	1.9 mm	2.6 mm	2.4 mm
Case 3 simulation	2.1 mm	2.5 mm	1.9 mm
Case 4 simulation	1.2 mm	1.6 mm	1.5 mm
Case 5 simulation	1.4 mm	1.7 mm	1.4 mm
Case 6 simulation	1.2 mm	1.7 mm	1.4 mm
Case 7 simulation	1.0 mm	1.6 mm	1.6 mm
Case 8 simulation	0.9 mm	1.5 mm	1.7 mm
Case 9 simulation	1.0 mm	1.6 mm	1.6 mm
Case 10 simulation	2.6 mm	3.0 mm	2.3 mm
Case 1 real	1.4 mm	1.6 mm	1.2 mm
Case 8 real	1.1 mm	1.7 mm	1.9 mm

3 displays the worse performance, also in line with our hypothesis. Localization plots for Case 3 show small error only when indenting directly over the Takktile's locations. Case 1 presents overall better predictions, albeit with larger errors for indentations close to the dome's edges.

With our cross-talk hypothesis confirmed, we test two additional variations of Case 1 while maintaining the peripheral Takktiles mounting angle at 25 degrees. Case 4 removes the central platform and Case 6 explores a new "ring" configuration. As our results show, both of these changes yield practically the same improvement with a median error of $1.2mm$.

Cases 5 and 7 through 10 are used to optimize the mounting angle of the Takktile pressure transducers. Altogether we test angles of 15, 25, 30, 35, 40 and 45 degrees for the ring configuration. Note that as we increase the mounting angle, the Takktile's sampling hole distance to the dome's surface is also increased. In order to keep the Takktiles normals pointing at the dome's surface and to maintain the distance to the dome's surface, the radial distance at which we mount them increases with the mounting angle. Case 5, with an angle of 15 degrees, results in a decrease of performance when compared to Case 6 (25 degrees). Increasing the angle, however, does improve the overall performance, with Case 8 (35 degrees) showing the best localization accuracy at $0.9mm$ median error. Angles greater than 35 degrees present a drop in performance, as exhibited by Case 9 and 10.

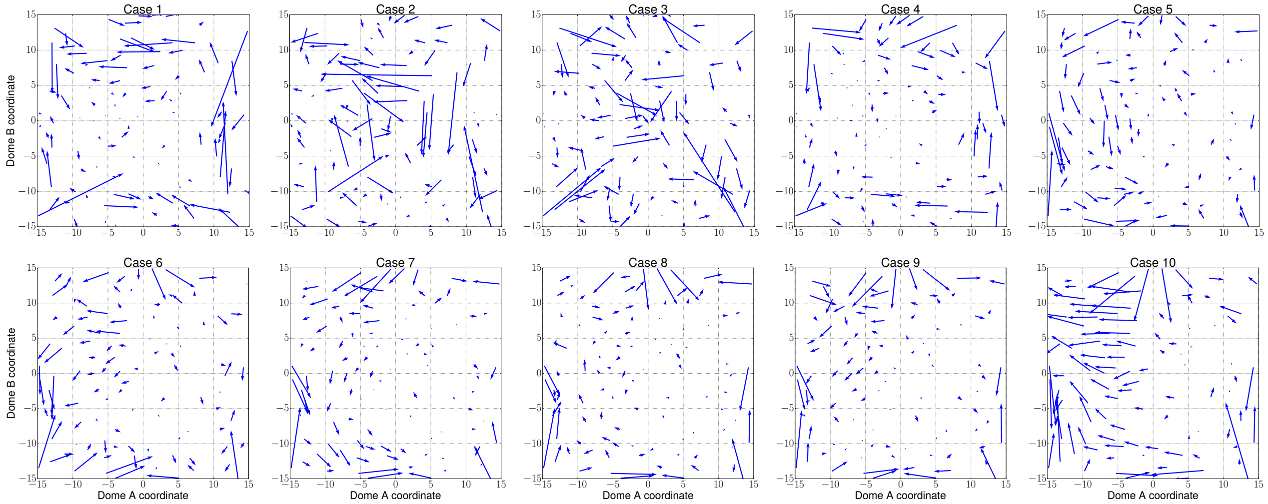

Figure 5.7: Simulation localization results for all ten defined cases of Takktile configurations. Each arrow represents one indentation in our test set; the base is at the ground truth location while the tip of the arrow shows the predicted location.

In general, the localization error plots in Figure 5.7 show that in our best performing cases, the predictions for indentations on the dome center are the most accurate whereas indentations at the very edge of the tactile dome display overall bigger prediction errors. Our hypothesis is that in these particular locations, the edges of the ABS base resolve the indenter force dominating the stress distribution and not enough Takktiles are excited to provide a better prediction.

5.6 Physical sensor testing and validation

In order to validate our simulation results, we build two physical tactile domes representing Case 1 and Case 8. We use two methods to compare the real sensor with the simulation. First, we look at the individual Takktiles response when we indent the dome along the symmetry lines defined in Figure 5.3. Second, we feed the real data to our localization algorithm and compare the localization error plots to evaluate their correlation both in terms of trends and numerical results.

Figure 5.8 shows these two evaluation methods for Case 1. The sensor response along the symmetry line displays the same trend for both the real data and the simulated data. Takktile number two in the real data shows some asymmetry with respect to Takktile four's response. This could be attributed to an incomplete degassing of this particular Takktile. For the localization error, both plots display a similar trend where large errors occur close to the dome edges. Numerically, the median error for the real case at $1.4mm$ is slightly better than what our simulation predicted ($1.5mm$), along with an improvement on both mean error and standard deviation.

For Case 8, the simulation shows a similar trend to the real data when indenting along the symmetry line, although it does not correspond as well as Case 1 (see Figure 5.9). It must be noted that this data represents an indentation along the axis $A = 1$, slightly offset from the symmetry line ($A = 0$), which we use to mirror the data obtained in simulation. While our real data performs slightly worse than our simulation predicted numerically, the sensor does outperform Case 1 with a median error of $1.1mm$, while the mean error is very similar with a larger standard deviation. The real and simulated localization plots display the same pattern in that large errors occur close to the edges of the dome.

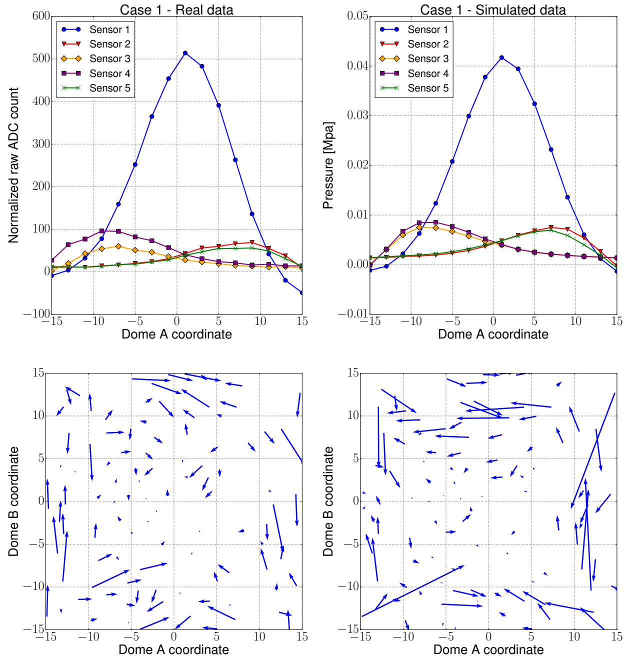

Figure 5.8: Takktile pressure transducers response when the dome is indented along symmetry line and localization plots comparison for Case 1. Left shows the data from the real sensor, right shows the simulation data.

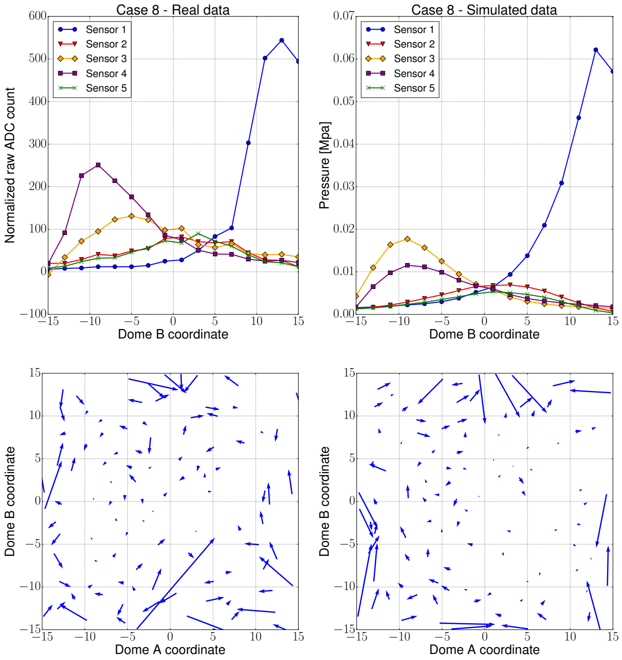

Figure 5.9: Takktile pressure transducers response when the dome is indented along symmetry line and localization plots comparison for Case 8. Left shows the data from the real sensor, right shows the simulation data.

5.7 Discussion

The main contributions of this chapter can be summarized as follows:

- We are the first to show that a purely data-driven method can use relatively few embedded sensing terminals (five) to achieve high accuracy contact localization (1.1 *mm* median error in the best case) over a large three dimensional surface (1300 mm^2). This reduces the overall cost of the sensor, minimizes the wiring, and simplifies future integration into hands.
- We explore the relationship between pressure transducer distribution inside a three dimensional volume, cross-talk between the sensing units induced by an indentation on the surface, and the indentation localization accuracy that results.
- We use finite element analysis to improve sensor performance by iterating over the design parameters in simulation. This eliminates the need to physically build a sensor to evaluate its relative performance. We validate the simulation against real implementations of multiple Takktile configurations and show how their placement affects individual pressure trends as well as overall performance.

Our hypotheses are therefore generally confirmed: our approach can accurately localize touch over curved, three dimensional surfaces. Our final design for the tactile dome, based on Case 8, exhibits 1.1 *mm* median error in localization accuracy with most large errors located at the very edge of the dome. It is likely that the base edges affect the stress distribution of the indentation. While not shown in this initial prototype, this trait might be avoided by a design with the Takktile's holding structure acting as a skeleton, and rubber cast on top of it, thus avoiding hard edges altogether and providing full coverage.

We also show that simulation tools, when available for the transduction method, can provide valuable insight to guide the design process of our sensors. The simulation allowed us to test the pressure transducers placement inside the volume of material and to effectively predict the final performance of the system. Our simulation exhibits the same trends as the real sensors in both pressure distribution among the embedded pressure transducers and overall performance of the localization algorithm. However, it is worth highlighting that even with simulation, it is impossible to completely explore the design space. We still rely on intuition to select candidate designs. The placement of sensing terminals can have counter intuitive effects on the final performance; for example, having a raised central Takktile in Case 1 does not provide better localization on the central region when compared to other cases.

The use of FEA simulation also opens up other possibilities: Would it be possible to use simulation to replace the our training process on the physical prototype? One of the main limitations of our data-driven methodology is the fact that the obtained model is constructed for the specific indenter shape used, with indentations constrained to directions normal to the sensor dome at fixed indentation depths. Therefore, it is uncertain what our model would predict if we were to use a different indenter shape, indent at several locations at once (multitouch), or at an angle other than the surface normal. While we expect that given appropriate training data, a data-driven algorithm will be able to learn to predict at least a subset of these parameters, the data collection effort must scale appropriately to capture all these different conditions. In order to substitute this data collection effort on the physical sensor, the simulation must be accurate enough replicating the sensing terminal signals on a quantitative level. In this study we use FEA analysis to analyze trends and patterns from a qualitative perspective and do not attempt to replicate perfectly the behavior of the real sensor, but this is a promising venue of research for our sensors.

Another important design parameter not explored in this study is the nature of the material used to fabricate the tactile dome. In this study we use Vytaflex 20 since it is the material used by the manufacturer to cast the Takktile pressure transducers. An interesting direction of research would be to study how different material properties, like hardness or Poisson's ratio, affect the pressure distribution for a given design. In humans, skin microstructures like intermediate ridges serve the function to enhance the tactile spatial acuity by magnifying the signals from the surface of the skin to the mechanoreceptors embedded in the dermis [11]. Specially engineered materials with microstructures such as this may also be of interest to manufacture tactile sensors.

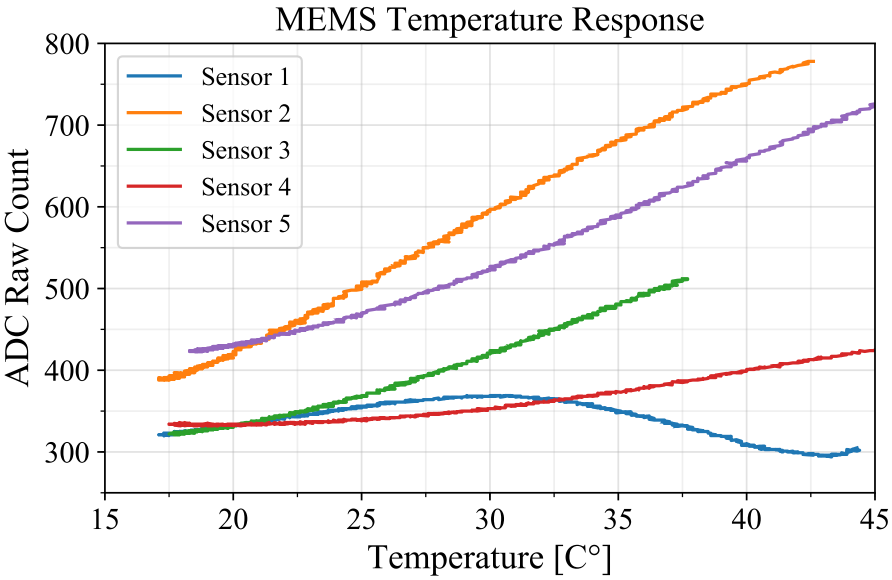

Figure 5.10: Temperature response of individual Takktile pressure transducers embedded inside our tactile dome. We placed the tactile dome corresponding to Case 1 inside a enclosed box with a heating element and proceed to record each Takktile's pressure and temperature readings as the tactile dome cooled down.

While the Takktile pressure transducers provide us with a signal to noise ratio far superior compared to the signals extracted from our piezoresistive sensor, we found them to be very sensitive to temperature changes. We show the temperature response of each individual Takktile on the prototype corresponding to Case 1 in Figure 5.10. We record the ADC reading and temperature measurement of each individual Takktile as the tactile dome cooled down after being placed in an enclosed box with a heating element inside. While it may be possible to compensate for linear and even non-linear responses, each Takktile showed different responses based on its location, with one unit demonstrating a non-monotonic response. An additional complication is that the temperature response was not consistent across various runs, although it is possible that after several heating and cool-down cycles the response might stabilize. This temperature sensitivity prevented us from obtaining a workable model to predict the applied contact force, which is why this capability was not discussed in this study. Perhaps the use of a rubber or elastomer with different thermal properties can help neutralize this issue, in which case it is likely the Takktile pressure transducers can be used to build a promising data-driven robotic finger with extensive coverage of curved surfaces.

However, we believe other transduction methods that allow us to exploit our all-pairs approach and therefore harvest a much larger number of tactile signals are worth investigating further. To that end, we will explore yet another transduction method in the next chapter: optics.

Chapter 6: Accurate contact localization and indentation depth prediction via optics

In this chapter we experiment with yet another transduction method exploiting our spatially overlapping signals method. We hope that the use of optics to build tactile sensors can provide us with repeatable, low noise signals amenable for our data-driven approach. Additionally, optics require simple electronics and are suitable for high frequency switching scenarios that result from sampling a large number of signals through time-multiplexing.

An important adaptation is needed for our method when using optics since each sensing terminal now has a defined role: they can be a light emitter (an LED) or a light receiver (a photodiode). As a result, sensing pairs can only be formed between an emitter and a receiver, making the total number of possible sensing pairs lower compared to our piezoresistive sensor shown in chapter 4. It must be noted that even though the number of sensing pairs as a function of number of sensing terminals grows at a slower rate, this growth is still quadratic and as a result we can still extract a large number of signals from each sensor.

An attractive quality of using optics as a transduction method stems from the possibility of guiding light through large distances with little attenuation, which can produce larger receptive fields in our method. The use of polydimethylsiloxane (PDMS) to build light waveguides is widely documented [127–129] for its low cost and ease of manufacturing.

Our approach is to build these sensors as a continuous volume of PDMS, with light emitters and receivers embedded along the perimeter and base. Indentation of the sensor area affects how light from the emitters is transported through this medium, producing a signal that is measured by the receivers. Throughout this chapter, we use indentation depth as a proxy for contact force, based on a known stiffness curve for the constituent material (see Figure 6.3).

Using these sensors we will show that our method can provide high accuracy in both localization and indentation depth prediction, as well as the capability of classifying different indenter geometries. The result is a tactile pad that exhibits desirable performance characteristics, while using a simple manufacturing method and low-cost components. As we will show in chapter 7, this fabrication technique and the data-driven signal processing approach lend themselves to constructing tactile sensors of irregular three-dimensional geometry, enabling easier integration into robotic fingers and palms.

6.1 Light transport and interaction modes

We first focus on a single emitter-receiver pair in order to discuss the underlying light transport mechanism in detail. The core transduction mechanism relies on the fact that as a probe indents the surface of the sensor, light transport between the emitter and the receiver is altered, changing the signal reported by the receiver (Figure 6.1). Consider the multiple ways in which light from the LED can reach the opposite photodiode: through a direct path or through a reflection. In particular, based on Snell's law, due to different refractive indices of the elastomer and air, light rays hitting the surface below the critical angle are reflected back into the elastomer.

As the probe makes initial contact with the sensor surface, the elastomer-air interface is removed from the contact area and surface normals are immediately disturbed. This changes the amount of light that can reach the diode via surface reflection. *This is the first mode of interaction that our transduction method captures.* It is highly sensitive to initial contact, and very little penetration depth produces a strong output signal.

As the depth of indentation increases, the indenter starts to also block light rays that were reaching the photodiode through a direct, line-of-sight path. *This is our second mode of interaction.* To produce a strong signal, the probe must reach deep enough under the surface where it blocks a significant part of the diode's surface from the LED's vantage point.

We note that other light paths are also possible between the emitter and receiver. The interface between the clear elastomer and the holding structure (the bottom and side walls of the cavity) can

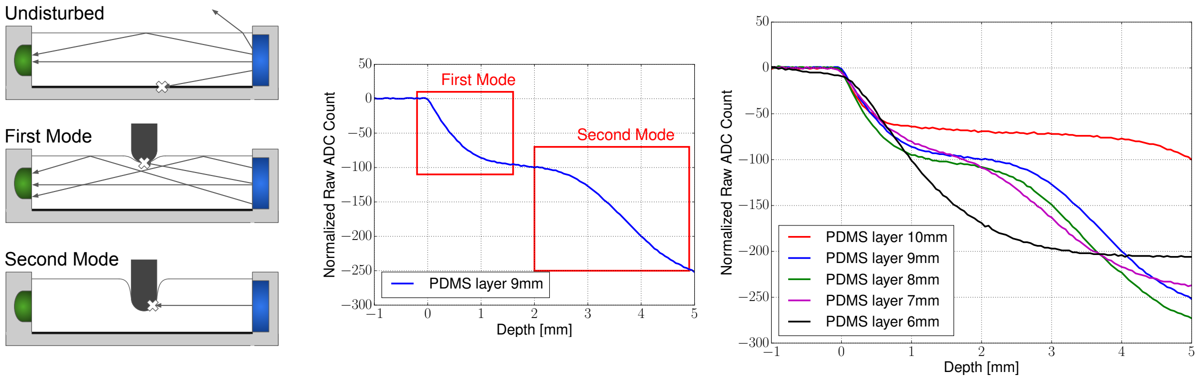

Figure 6.1: **Left and middle:** interaction modes. The first mode of detection happens upon light contact and manifests as a sudden drop in the signal. The second mode is activated with a heavier contact, in this particular case after a depth of approximately 2mm. **Right:** we investigated this behavior for different heights of the PDMS layer, in order to select one for which these two modes are contiguous.

also give rise to reflections. While we do not explicitly consider their effects, they can still produce meaningful signals that are captured by the data-driven mapping algorithm.

We would like our sensor to take advantage of both operating modes described above, noting that one is highly sensitive to small indentations while the other provides a strong response to deeper probes. *We thus aim to design our sensor such that these two modes are continuous as the indentation depth increases.* The goal is to obtain high sensitivity throughout the operating range of the sensor. The key geometric factor affecting this behavior is the height of the elastomer layer, which we determine experimentally.

To investigate this factor, we constructed multiple 3D printed square molds with LEDs (SunLED XSCWD23MB) placed 20 *mm* in opposition from the photodiode (Osram SFH 206K), with PDMS filling the cavity. Work by Johnson and Adelson [66] shows PDMS and air have approximate refractive indexes of 1.4 and 1.0 respectively, with a critical angle of 45 degrees. Each mold was filled with PDMS to achieve a different layer thickness and then indented to 5 *mm* depth in a midpoint location between the LED and the photodiode. Results are shown in Figure 6.1. We note that prototypes with PDMS layers over 10 *mm* exhibited a dead band: after a certain threshold depth the photodiode signal does not change as we indent further down until you indent deep enough to activate the second mode. In contrast, the 7 *mm* layer provides the best continuity between our two modes, while the 8 *mm* layer gives good continuity while also producing a stronger signal when indented. We thus built all our subsequent sensors with an 8 *mm* PDMS layer.

6.2 Sensors construction

This chapter presents two similar planar optical tactile sensors. Our first optic sensor prototype was built using simple Through-Hole Technology (THT) LEDs and photodiodes, placed exclusively around the perimeter of a square PDMS filled cavity that acts as a waveguide. This prototype is shown in Figure 6.2, Left. For our second sensor prototype, we used Surface-Mount Technology (SMT) components. We developed prototype boards containing two LEDs and two photodiodes each, with all wiring for the four components combined through a single connector. Compared to using through-hole components, this packaging simplified the manufacturing process in order to include terminals on the base of the sensor in addition to those around the perimeter. This prototype is shown in Figure 6.2, Right.

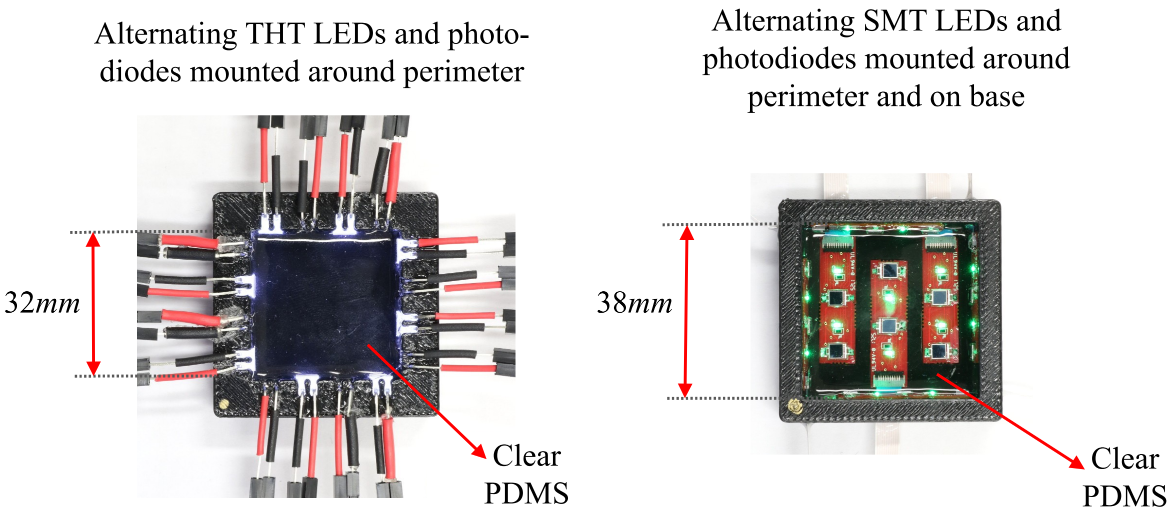

Figure 6.2: **Left:** optical sensor where alternating through-hole technology (THT) LEDs and photodiodes are edge-mounted and the cavity is filled with a clear elastomer. **Right:** optical sensor with surface-mount technology (SMT) LEDs and photodiodes, mounted both along the perimeter and on the base.

THT Optical Sensor construction

Our sensor is comprised of 8 LEDs and 8 photodiodes arranged in an alternating pattern and mounted in sockets along the central cavity walls. Any LED is thus able to excite multiple photodiodes. For this sensor we used through-hole technology (THT) components for ease of prototyping. We used a 5 x 5 x 7.2 *mm* sized LED model SunLED XSCWD23MB with peak wavelength 460 *nm* and a Osram SFH 206K photodiode with peak sensitivity at 850 *nm* and a 2.65 x 2.65 *mm* sensitive area. To build the sensor we use a 3D printed square mold with exterior dimensions of 48 x 48 *mm*. The cavity in the mold is 32 x 32 *mm*, which is filled with PDMS at a ratio of 1:20 curing agent to PDMS. The resulting mapping of indentation depth to compression load is presented in Figure 6.3.

As this sensor only has terminals around its perimeter, the base simply consists of 3D printed ABS plastic. However, we found that the clear elastomer and the holding plastic exhibit bonding/unbonding effects at a time scale of 5-10s when indented, creating unwanted hysteresis. To eliminate such effects, we coat the bottom of the sensor with a 1 *mm* layer of elastomer saturated with carbon black particles (shown in Figure 6.1 by a thick black line). This eliminates bottom surface reflections, and exhibits no adverse effects, as the clear elastomer permanently bonds with the carbon black-filled layer. As shown in Figure 6.4, this sensor exhibits little to no hystere-

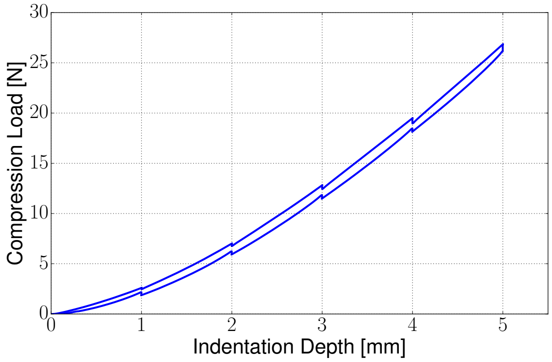

Figure 6.3: Load vs indentation depth for a 1:20 ratio of curing agent to PDMS, measured by advancing or retracting the probe in 1 *mm* steps with 10 second pauses using a 6 *mm* diameter hemispherical tip

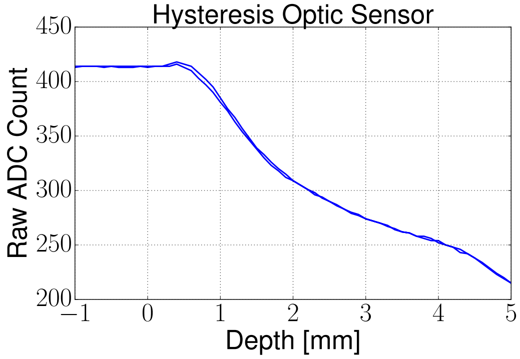

Figure 6.4: Shown is the response of a single terminal pair to an indentation up to 5 *mm* using a 6 *mm* diameter hemispherical indenter. There is no appreciable hysteresis, as the signal recorded is almost exactly the same when the probe advances and retracts from the material.

sis between an indentation and the subsequent retraction, in contrast to the piezoresistive sensor presented in chapter 4.

An Arduino Mega 2560 handles LED switching and taking analogue readings of each photodiode. The photodiode signal is amplified through a standard trans-impedance amplifier circuit, and each LED is driven at full power using an NPN bipolar junction transistor. The resulting sampling frequency with this setup is 60 Hz.

SMT Optical sensor construction

The surface-mount technology (SMT) optic sensor follows a similar fabrication method to the through-hole technology (THT) version. We initially 3D print out of ABS plastic a square mold with exterior dimensions of 48 x 48 *mm*. The interior cavity in the mold is 38 x 38 *mm*. This sensor presents sockets both on its walls, as well as on its base to fit the small PCB boards where the LEDs and photodiodes are located.

Each PCB board measures 29 *mm* length and 8 *mm* width. The front of the PCB board holds two 1.6 x 0.8 *mm* LEDs (Kingbright APG1608ZGC, peak wavelength 515 *nm*) and two 4.0 x 4.5 *mm* photodiodes (OSRAM BPW34S E9601, peak sensitivity 850 *nm*) in alternate pattern. Additionally, the front holds an FFC connector to interface with our measuring circuit. The back of the PCB board holds an operational amplifier (Analog Devices AD8616) on a trans-impedance amplifier configuration. Overall this sensor uses 7 PCB boards, 4 being located on the mold's walls and the remaining 3 being placed on the mold's base. This represents a total of 14 LEDs and 14 photodiodes.

For the same reasons as in our THT optic sensor, before installing the PCB boards, we coat the base of the sensor with a 1mm layer of PDMS saturated with carbon black particles. After curing this layer, we cut out the carbon black infused PDMS on the sockets so that we can place the boards inside them. For all PCB boards we use a few drops of glue to place them inside their sockets. The flexible flat cables used to connect to each individual board are routed through small holes on the walls of the 3D printed mold. After connecting each board, these holes are sealed using epoxy. At this point, we fill the mold cavity with the elastomer at a 1:20 curing agent to PDMS ratio.

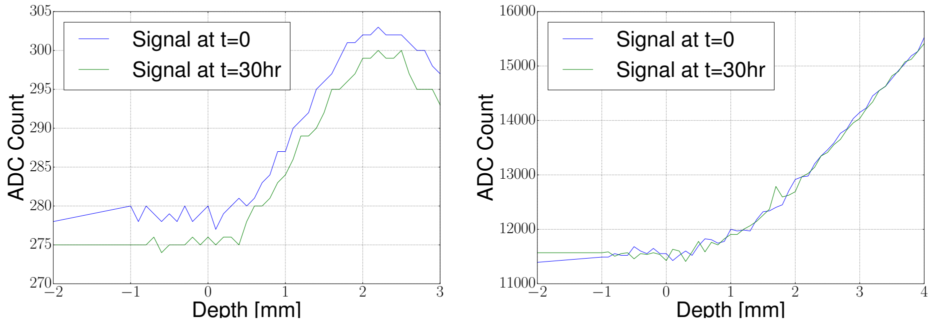

Figure 6.5: Signal comparison over time for two versions of our optics-based sensors, with THT components (Left) and SMT components (Right). In each case, we performed 60 consecutive indentations with the 6 *mm* diameter hemispherical tip in a single sensor location, with the indentations spaced 30 minutes apart. Each plot shows the signal from the first and last indentation in the respective set.

A microcontroller (NXP LPC1768) handles switching the LEDs and taking analogue readings of each photodiode. As a result of this microcontroller being orders of magnitude more powerful than the Arduino Mega, the sampling rate to collect and report all signals is approximately 100Hz.

An important result of this manufacturing process is the absence of drift over large time scales and large numbers of intermediate indentations. Figure 6.5 shows a comparison of individual signals over time for both versions of the optical sensor. The THT sensor exhibits a drift in the signal while the SMT sensor shows no similar phenomenon. We attribute this change to the use of SMT LEDs with much smaller surface area, that do not exhibit unwanted bonding/unbonding behavior with the elastomer.

6.3 Data collection

For data collection we use the exact same setup as described in chapter 4, section 4.2 to indent the surface of the sensor in a normal direction to the sensor surface.

When collecting data, we read signals from all the photodiodes as different LEDs turn on. This process is multiplexed in time, meaning that we turn on an LED, proceed to take readings from all possible photodiodes and then move on to the next LED until we have sampled all possible pairs. Additionally, we also take a reading of all photodiodes when all the LEDs are off. This allows us to measure the ambient light captured by each diode and subtract it from all other signals, so that the sensor can perform consistently in different lighting situations.

The main difference compared to the piezoresistive sensor is that we treat indentation depth as an additional variable. At each location we use the following protocol. We consider the sensor surface to be the reference level, with positive depth values corresponding to the indenter tip going deeper into the sensor. We collect data at both negative and positive depths. For depths between $-10\ mm$ and $-1\ mm$, we collect one data point every $1\ mm$. The indenter then goes down to a depth of $5.0\ mm$ (exception to this is when using different indenter geometries) taking measurements every $0.1\ mm$. The same procedure is mirrored with the indenter tip retracting.

THT sensor data collection.

This sensor contains 8 LEDs and 8 photodiodes. Each measurement i results in a tuple of the form $\Phi_i = (x_i, y_i, d_i, p^1_{j=1}, .., p^8_{j=1}, ..., p^1_{j=9}, .., p^8_{j=9})$ where (x_i, y_i) is the indentation location in sensor coordinates, d_i is the depth at which the measurement was taken and $(p^1_j, .., p^8_j)$ correspond to readings of our 8 photodiodes as we turn each LED on: state $j \epsilon [1, 8]$, from which we subtract the ambient light captured by each diode when all LEDs are turned off (state $j = 9$). We thus have a total of 75 numbers in each tuple Φ_i.

Similar to the the procedure described in chapter 4 section 4.2, we use a *grid indentation pattern* for training data and a *random indentation pattern* for testing. Taking into account the diameter of our tip, plus a $3\ mm$ margin such that we do not indent directly next to an edge, our grid indentation pattern results in 121 locations distributed over a $20\ x\ 20\ mm$ area ($11x11$ grid). We allow for a bigger margin compared to the resistive sensor since the components are mounted directly on the walls of our mold.

To train our predictors we collected four *grid pattern* datasets, each consisting of 121 indentations, and each indentation containing 161 datapoints at different depths. Aiming for robustness to changes in lighting conditions, two of these datasets were collected with the sensor exposed to ambient light and the other two datasets were collected in darkness. The feature vector used for training has a dimensionality of 64. For testing, we collected two datasets using the *random*

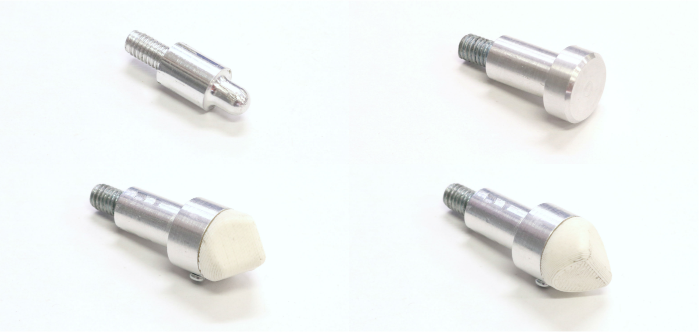

Figure 6.6: The four different indenter types used for our classification: hemispherical, flat, corner and edge tips. The edge tip (lower right) was used with orientations of 0, 120 and 240 degrees.

indentation pattern, one collected in ambient light and another collected in the dark, with 100 indentation events in each. Results for this sensor are presented in section 6.4 through 6.7.

SMT sensor data collection.

We collect data on this sensor in the same manner as for the THT sensor. One difference is that we now use 14 LEDs and 14 photodiodes. We continue to read a baseline signal with all LEDs turned off which we subtract from all other signals to make the sensor robust under changing ambient light conditions.

The primary difference with this sensor is that we now repeat this data collection process for multiple indenter tips. To mimic geometries which are likely to be encountered in common workspaces, we manufactured the following indenter tips: circular planar with 15 *mm* diameter, 90° edge with 15 *mm* length, and a square corner with maximum width 15 *mm* (Figure 6.6) We take separate datasets with the edge tip oriented at three positions, each 120° apart. We also include the 6 *mm* diameter hemispherical tip which was used in previous sections. This results in 6 different indenter geometries.

Due to force constraints on our indentation actuator, every tip does not reach the same maximum indentation depth. The planar tip reaches a maximum depth of 1.2 *mm*, the edge tip reaches a maximum of 3.0 *mm*, and all other tips reach a maximum depth of 4.0 *mm*.

Each measurement i now results in a tuple of the form $\Phi_i = (t_i, x_i, y_i, d_i, p^1_{j=1}, .., p^{14}_{j=1}, ..., p^1_{j=15}, .., p^{14}_{j=15})$ where $t_i \in \{1, .., 6\}$ identifies the tip used for the indentation, (x_i, y_i) is the indentation location in sensor coordinates, d_i is the depth at which the measurement was taken and $(p_j^1, .., p_j^{14})$ correspond to readings of our 14 photodiodes as we turn each LED on: state $j \in [1, 14]$, from which we subtract the ambient light captured by each diode when all LEDs are turned off (state $j = 15$). We thus have a total of 214 numbers in each tuple Φ_i.

We again use a *grid indentation pattern* for training and a *random indentation pattern* for testing. This sensor has a 38*x*38 *mm* PDMS surface. Taking into account our larger tip radius (7.5 *mm*) and a 3.5 *mm* margin, our indentation pattern results in 81 locations distributed in 2 *mm* intervals over a 16 *x* 16 *mm* grid. For testing, the *random indentation pattern* consists of 100 indentation events scattered within the same area.

Our objective for this sensor is twofold: to determine whether our signals contain sufficient information to reliably classify the tip geometry with which the sensor is being contacted; and to explore our sensor's ability to identify contact depth and location regardless of tip geometry. To train our models we use a single dataset for each tip, each collected in the dark. The feature vector for training has a dimensionality of 196. Results for this sensor are presented in section 6.8.

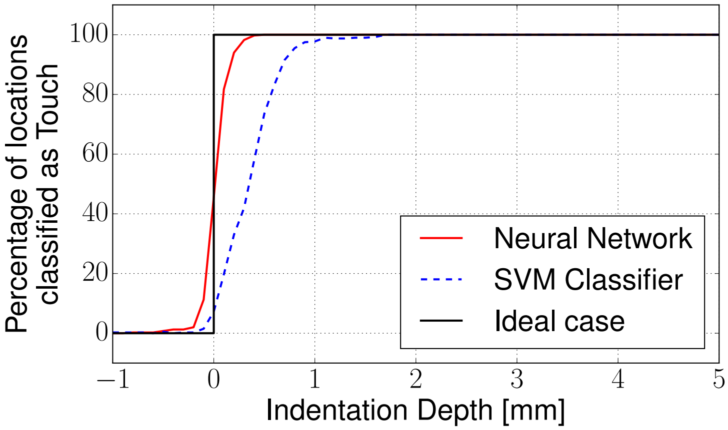

Figure 6.7: Touch classification results over all locations in our test dataset. Values in the graph represent the percentage of locations in our test dataset where touch was predicted for an indentation at a given depth.

6.4 Touch classification

The first step before predicting location and depth is to use a classifier to determine if touch is occurring; this classifier is trained on both data points with $d_i < 0$ and $d_i \geq 0$. Note that these results correspond exclusively to our THT optic sensor.

We tested two different classification methods: a linear SVM and a Neural Network (NN) with one input layer, one hidden layer (1024 nodes, ReLU activation function) and one output layer (1 node, sigmoid activation function). Results for both classifiers are presented in Figure 6.7. For any given depth, we show the percentage of indentations (over all of our test locations) that are classified as touch.

For an indentation depth of 0.1 *mm* the NN classifier correctly classifies 82% of the events as "touch", increasing to 94% at 0.2 mm and hitting 98% at 0.3 *mm*. The price we pay is an 11% misclassification rate at -0.1 *mm* depth (slightly above the surface). The SVM classifier rarely interprets cases above the surface as touch, but starts reliably predicting touch (above 80% of cases) at a depth of 0.5 *mm* or higher, hitting 99% after 1 *mm*. Overall, using the NN classifier, and according to the elasticity profile of our material (see Figure 6.3), we detect touch with 82% reliability for a force of 0.11 N (0.1 *mm* indentation) and 98% reliability at 0.55 N (0.3 *mm*) or higher.

6.5 Location and depth regression

If the classifier predicts touch is occurring, we use a second stage regressor to predict values for (x_i, y_i, d_i). This regressor is trained only on training data with $d_i \geq 0$. We use a kernelized ridge regressor with a Laplacian kernel and use half of the training data to calibrate the ridge regression tuning factor λ and the kernel bandwidth σ through grid search. However, the computational requirements of training a ridge regressor with a non-linear kernel require downsampling of our training data: for each indentation, we only trained on indentation depths in 0.5 *mm* increments starting from the surface of the sensors. Results presented in this section were obtained with

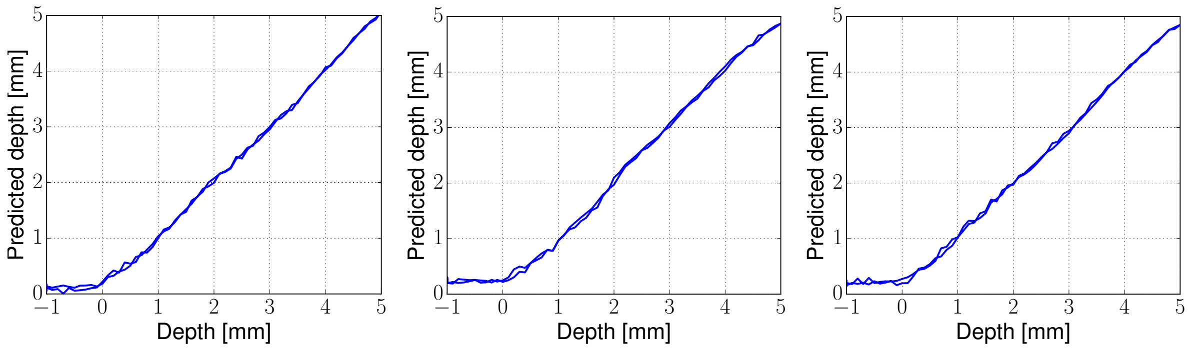

Center

Edge

Corner

Figure 6.8: Regression results for depth prediction at three of the random locations in our test datasets, close to the center (sensor coordinates 16.5,19.1), an edge (6.4, 18.3) and a corner (10.9, 6.2).

$\lambda = 2.15e^{-}4$ and $\sigma = 5.45e^{-}4$. Note that these results correspond exclusively to our THT optic sensor.

The metric used to quantify the success of our regressor is the magnitude of the error for both the localization and depth accuracy. Detailed numerical results for both of these metrics, and for both ambient light and dark datasets, are presented in Table 6.1, aggregated over our entire test sets.

To provide more insight into the behavior of the sensor, we present additional visualizations for the error in both depth and location. The results for depth can only be visualized for specific locations. Figure 6.8 shows the performance at three different locations in our ambient light test dataset. Since this regressor is trained only on contact data, it is not able to predict negative depths which causes error to be greater at depths close to 0 *mm*. At 0.5 *mm* and deeper, the depth prediction shows an accuracy of below half a millimeter.

Localization results on the light dataset can be visualized in Figure 6.9 for a few representative depths. At depth 0.1 *mm* the signals are still not good enough to provide accurate localization, but as we indent further down localization improves well beyond sub-millimeter accuracy.

Table 6.1: Localization and depth accuracy

Ambient Light Dataset

Depth (mm)	**Localization Error** (mm) Median	Mean	Std. Dev	**Depth Error** (mm) Median	Mean	Std. Dev
0.1	2.18	2.36	1.50	0.16	0.16	0.07
0.5	0.71	0.83	0.61	0.05	0.06	0.04
1.0	0.64	0.74	0.53	0.04	0.06	0.05
2.0	0.42	0.50	0.31	0.04	0.04	0.03
3.0	0.36	0.41	0.25	0.03	0.04	0.04
5.0	0.31	0.35	0.22	0.08	0.09	0.06

Dark Dataset

Depth (mm)	**Localization Error** (mm) Median	Mean	Std. Dev	**Depth Error** (mm) Median	Mean	Std. Dev
0.1	3.50	3.83	2.20	0.18	0.18	0.07
0.5	1.10	1.33	0.98	0.05	0.05	0.04
1.0	0.77	0.84	0.53	0.05	0.06	0.04
2.0	0.54	0.65	0.45	0.04	0.05	0.04
3.0	0.41	0.48	0.32	0.03	0.05	0.04
5.0	0.31	0.39	0.28	0.08	0.10	0.07

6.6 Signal removal analysis

Given the nature of our spatially overlapping signals method, it is of special interest to analyze the relationship between the number of sensing terminals and the resulting accuracy in touch localization and depth prediction. Here, we use the term “sensing terminal” to refer to either an LED or photodiode in a generic way. Our hypothesis is that a higher number of sensing terminals will yield higher accuracy, but how we distribute these terminals to over the intended sensing area also plays an important role in determining performance.

We consider four different cases for our optical sensor. In each case, we discard the signals from a subset of terminals of the base configuration (which has a total of 16 terminals). We compare these cases between themselves, and against the base configuration. We use the localization and depth error at a depth of 2 *mm* for the sake of readability (other depths follow the same trend). Note that the following results correspond exclusively to our THT optic sensor.

The four cases are presented in Figure 6.10. Cases 1 and 2 have four sensing terminals removed (4 LEDs in Case 1, 2 LEDs and 2 photodiodes in Case 2). However, they present different distribution of terminals along the edge of the sensing area. Cases 3 and 4 each have eight terminals removed (4 LEDs and 4 photodiodes), again with different spatial distributions. Localization results are also shown in Figure 6.10. (Comparative performance for the base case is in Figure 6.9 at 2 *mm* depth.) Accuracy in both localization and depth predictions is also summarized in Table 6.2.

Results show that a higher number of sensing terminals always results in a lower median error for localization accuracy and for depth accuracy. Additionally, we make two observations on this data. First, performance tends to increase or decrease uniformly, over the entire surface of the sensor, rather than locally, in the vicinity of additional terminals. Case 2 shows no noticeable difference in performance along the top vs. bottom edges; Cases 3 and 4 show similar performance

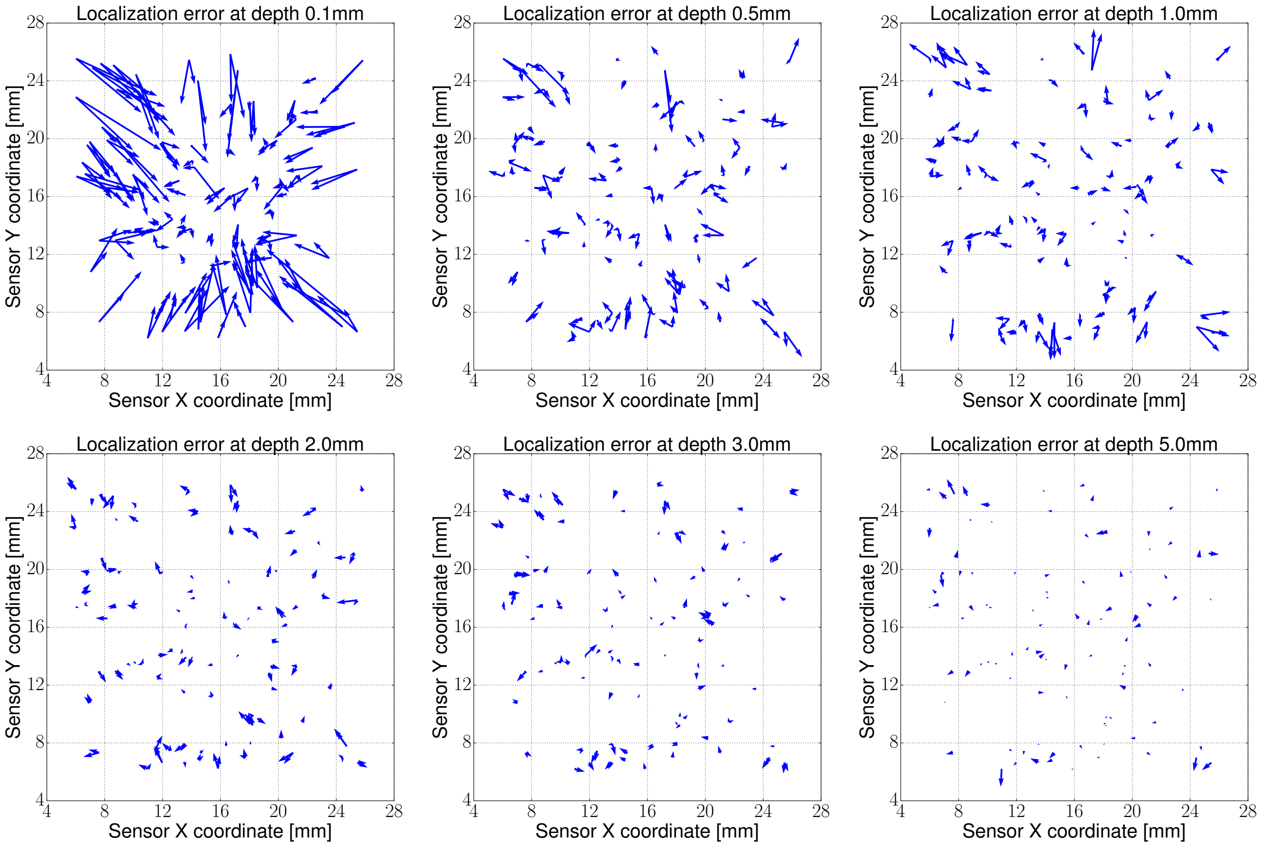

Figure 6.9: Localization results for ambient light test dataset. Each arrow represents one indentation in our test set; the base is at the ground truth location while the tip of the arrow shows the predicted location.

along edges and corners despite different terminal placements.

Second, for the same number of terminals, a more homogeneous distribution uniformly increases general performance. Numerical results show that case 1 performs better than case 2 in both metrics with the same number of sensing terminals, but with a more homogeneous distribution of the receptive fields for the sensing pairs. Following the same pattern, case 3 also outperforms case 4. Both of these phenomena could be due to the fact that our intuition with respect to how the light travels through the elastomer and what the receptive fields for a given pair look like might be a bit too simplistic. As we rely on a purely data driven method, all of these complex interactions are captured at training time. Future studies can provide more insight as to how to optimize the

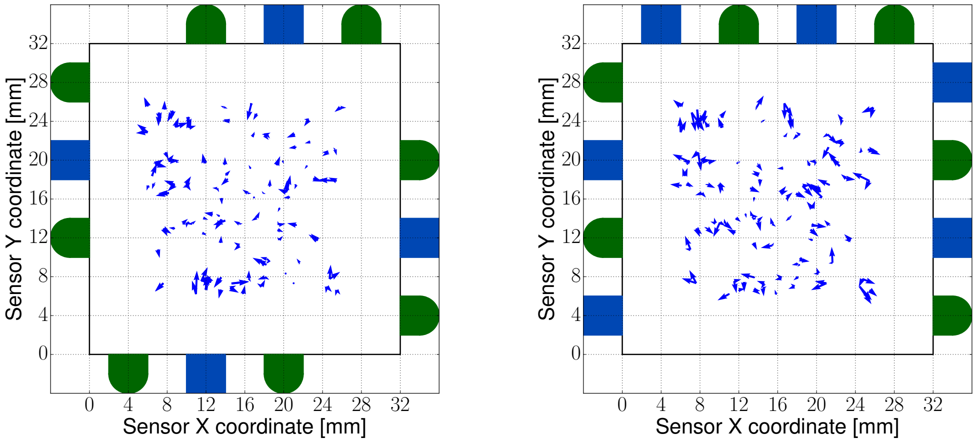

(a) Case 1 (b) Case 2

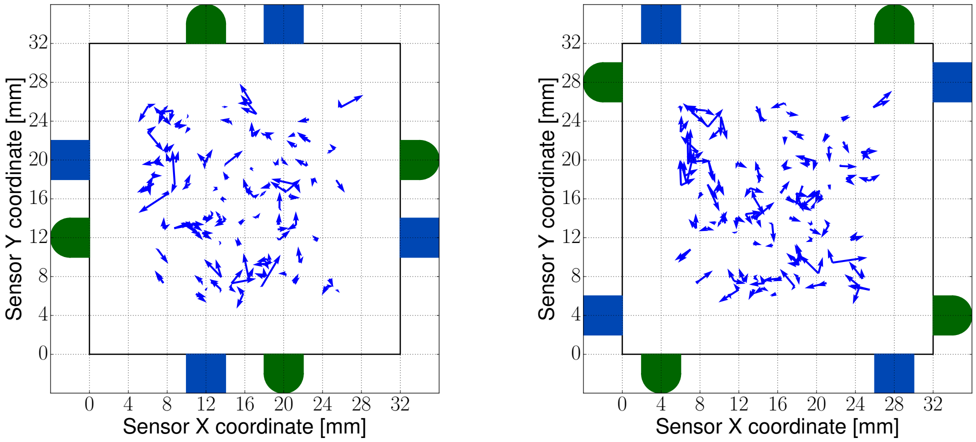

(c) Case 3 (d) Case 4

Figure 6.10: Localization error at 2 *mm* indentation depth for cases where sensing terminals have been removed from our base configuration. Green semicircles (diodes) and blue squares (LEDs) indicate the terminals present in each case.

Table 6.2: Performance based on number and distribution of sensing terminals (localization at 2 *mm* depth). Baseline (first row) consists of using all available terminals.

Cases	**Localization Error** (mm)			**Depth Error** (mm)		
	Median	Mean	Std Dev	Median	Mean	Std Dev
Baseline	0.42	0.50	0.31	0.04	0.04	0.03
Case 1	0.62	0.69	0.41	0.06	0.08	0.07
Case 2	0.70	0.80	0.49	0.11	0.13	0.11
Case 3	0.86	1.02	0.67	0.12	0.15	0.11
Case 4	1.11	1.24	0.75	0.17	0.21	0.17

distribution of the sensing terminals to aid the design of our sensors.

6.7 Multistage training for larger sensors

An important question regarding our approach is its ability to scale to larger sensor sizes. With our current geometry, increasing the dimension of the sensor side leads to a proportional increase in the distances between sensing elements (as long as they are still distributed only on the border), and a quadratically increased sensing surface area.

To investigate these effects, we constructed a second THT optical sensor with a 45 *mm* side. Accounting for the tip diameter and the safety margin (as before), this implies a 1024 mm^2 sensing area, a 2.56 *X* increase compared to the sensor shown in Figure 6.2, Left. All other aspects of the design where unchanged, including the number of terminals and their distribution in the sensor.

We applied the exact same data-driven mapping algorithm described in the previous section. We recall that the core learning algorithm used is an kernel ridge regressor trained to simultaneously predict indentation depth and location. We thus refer to this method as "single-stage training"; the results on the larger sensor are shown in Table 6.3. As expected, we notice a performance degradation compared to the smaller sensor, even though localization error is still below 1 *mm* at indentation depths of 2 *mm* or higher.

One possibility to recover some of the performance drop would be to increase the amount of training data; however, given the larger surface size, this becomes prohibitively expensive from a computational standpoint if training a single regressor. To account for this, we split our training

Table 6.3: Localization error (mm) for large sensor

Depth (mm)	**Single stage training** Median	Mean	Std. Dev	**Multistage training** Median	Mean	Std. Dev
0.1	2.22	2.63	1.87	1.72	2.15	1.65
0.5	1.67	1.95	1.29	1.27	1.48	1.03
1.0	1.36	1.50	0.92	1.17	1.32	0.84
2.0	0.94	1.06	0.64	0.53	0.68	0.43
3.0	0.74	0.81	0.47	0.63	0.75	0.49
5.0	0.94	1.06	0.64	0.53	0.60	0.38

/ testing procedure into specialized stages. First, we trained an linear regressor to exclusively predict the depth of the indentation. Second, we used five separate regressors to predict indentation location, each trained for specific range of depths. Each of these regressors was trained on a 1 *mm* slice of indentation depths, centered at 0.5, 1.5, 2.5, 3.5 and 4.5 *mm* respectively.

The corresponding multistage testing procedure is as follows: first, the specialized depth regressor predicts indentation depth, referred to as d_p. Then, based on this result, the test tuple is sent to the localization regressor whose range covers d_p. In turn, this chosen regressor predicts the location of the indentation, which completes our prediction.

The advantage compared to single-stage prediction is that each localization regressor is only trained on a subset of the data - the slice corresponding to its assigned depth range. We can thus afford to increase the resolution of our training samples by a similar amount with no effect on the training time. Taking advantage of this, we trained our predictors using training data sampled at every 0.1 *mm* in depth (as opposed to 0.5 *mm* in the previous section). The results of this multistage approach (with more training data) are also shown in Table 6.3.

We notice that adding more training data increases performance at all depths and approaches the results obtained for the smaller sensor. Overall, we believe these results show that our approach can scale to larger sensor sizes, and that training variants that allow for more data can, up to a point, help mitigate performance loss. Of course, if the sensor size keeps increasing, we expect to run into computational limits that could require a completely different learning approach. However, we believe that the dimensions demonstrate here are in line with the requirements of our desired application, integration into robot fingers for human-scale manipulation.

6.8 Robustness to indenter geometry

Our THT optic sensor combines sub-millimeter localization accuracy (in many cases improving to half-millimeter) with indentation depth determination within a tenth of a millimeter. Still, these results have all been obtained with a single indenter tip, used for both training and testing. Our method builds a forward model of the sensor based on the training data provided, but real world conditions will likely differ from those encountered during training. For this reason we are interested in investigating the robustness of this method when indented with a new indenter geometry that it has not been trained on.

Additionally, we have found that our THT sensor, while showing no discernible hysteresis over time scale on the order of seconds, does exhibit signal drift over periods of hours and large numbers of repeated indentations (see Figure 6.5). Visual inspection showed that, after repeated indentations and over long periods of time, the transparent elastomer begins detaching from the surface of the LEDs, which affects light propagation. We address this issue with the SMT version of our sensor.

Discriminating between indenter geometries.

To perform this classification we use a Neural Network with one input layer, one hidden layer (1024 nodes, ReLU activation function), and one output layer (6 nodes, softmax activation function). The classifier is trained and tested on all six datasets (corresponding to each indenter geometry), with both $d_i < 0$ and $d_i \geq 0$. The primary metric for evaluating classifier performance is accuracy; that is, the ratio of the number of data points correctly classified to the total number of data points. This performance is shown as a function of indentation depth in Figure 6.11.

In the limit of negative depths, the classification accuracy converges to the expected 16.6%, or 1/6 random chance. The accuracy increases with indentation depth and achieves a maximum of 98.5% at 4.0 mm.

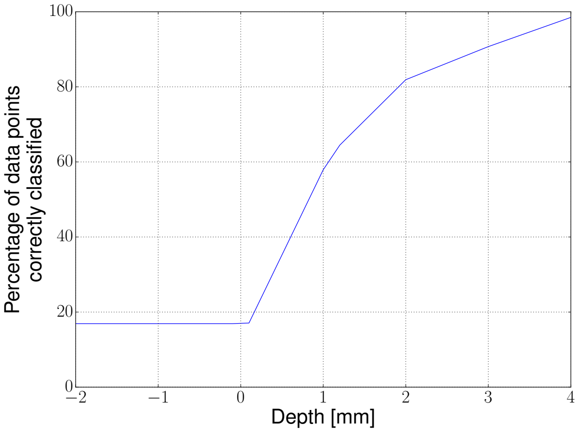

Figure 6.11: Tip classification results over all locations in our test dataset as a function of indentation depth. Values in the graph represent the percentage of data points in our test dataset whose tip geometries were correctly classified.

Location and depth regression with multiple indenter geometries.

The goal here is to determine our ability to identify contact location and indentation depth regardless of indenter tip geometry. To do this, we use a kernelized ridge regressor analogous to that presented in section 6.5. We train this regressor on all six datasets. Due to the size of this combined dataset and the computational requirements of training this regressor, we undersample our data based upon depth, maintaining higher granularity near the sensor surface. Results presented in this section were obtained with $\gamma = 10.0e^{-7}$ and $\alpha = 0.01$. The results of testing this regressor on all six datasets are tabulated in Table 6.4. Compared to the localization and depth regression performance of the optics-based sensor shown in Table 6.1, we see improved performance at low depths and weaker performance at larger depths. However, we consider these results to be well

Table 6.4: Localization and depth accuracy for all indenter geometries.

Depth	**Localization Error** (mm)			**Depth Error** (mm)		
(mm)	Median	Mean	Std. Dev	Median	Mean	Std. Dev
0.1	1.58	1.81	1.17	0.17	0.18	0.10
0.5	1.35	1.53	1.00	0.10	0.12	0.09
1.0	1.13	1.38	0.95	0.10	0.13	0.10
2.0	0.96	1.21	0.90	0.18	0.22	0.17
3.0	0.91	1.14	0.85	0.28	0.33	0.24
4.0	1.11	1.27	0.78	0.63	0.66	0.32

Table 6.5: Localization and depth accuracy with individual tips removed from training. All results are shown for an indentation depth of $2mm$, with the exception of the Planar tip for which results are shown at $1mm$ depth.

Tip Removed	**Localization Error** (mm)			**Depth Error** (mm)		
	Median	Mean	Std. Dev	Median	Mean	Std. Dev
Planar	1.30	1.31	0.61	0.18	0.21	0.17
Edge 1	1.27	1.32	0.56	0.61	0.58	0.24
Edge 2	0.97	1.10	0.66	0.29	0.29	0.19
Edge 3	0.61	0.80	0.59	0.16	0.18	0.13
Corner	0.90	1.05	0.66	1.08	1.08	0.10
Hemisphere	1.10	1.36	0.91	0.51	0.51	0.11

within the operating margin for a practicable sensor.

Tip removal analysis.

In practice, a tactile sensor will encounter indentation geometries which have not been included in the training of its working model. In pursuit of robustness when faced with such a situation, we analyze our sensor's performance when testing on tip data not included in training. We train six regressors, each on a different five of the six possible tips. Each of these regressors is then tested exclusively on data associated with the missing tip. The results of this analysis are tabulated in Table 6.5. Overall, these results are on the same order as those seen when all tips are included (Table 6.4), suggesting the ability of our sensor to accurately predict on indentation geometries not formerly encountered.

6.9 Discussion

The main contributions of this chapter can be summarized as follows:

- We leverage multiple modes of interaction between an indenting probe and a light-transporting medium in order to increase depth prediction accuracy throughout the operating range. Indentation of the medium affects light transport in at least two ways. First, during initial contact, the probe alters the geometry of the surface and changes the refraction of the light rays. Second, as indentation becomes deeper, the probe blocks direct paths between emitters and receivers. We design our sensor to use both modes in continuous fashion, resulting in a good sensitivity throughout a wide range of indentation depths.

- We show purely data-driven sensors capable of determining with very high accuracy both the location and and the depth (proxy for force) of an indentation anywhere along an elastomeric surface. We also demonstrate the ability to classify different indenter shapes and show that our sensors can be trained to provide accurate localization and depth predictions even when encountering new indenter geometries.

Our THT optical sensors achieve sub-millimeter localization accuracy over 400 mm^2 and 1024 mm^2 workspaces, for indentation depths ranging between 1 and 5 mm. These sensors also demonstrate prediction of indentation depth accurate to within 0.1 mm for a large part of its operating range. The SMT optic sensor can localize contacts with an accuracy of approximately 1 mm regardless of the indenter geometry over a 574 mm^2 workspace. To achieve similar accuracy, the traditional sensor matrix approach would require numerous individual taxels with complex manufacturing, wiring and addressing techniques. In contrast, we use and as few as 16 and 28 terminals for the THT and SMT optic sensors respectively.

We have also shown on our SMT optic sensor that our data-driven approach can be robust to different indenter geometries. The sensor can distinguish between different indenter types and, maybe even more importantly, provide accurate localization and depth predictions even when using a previously unseen indenter. This result is of particular importance, since we can only train a finite number of indenter geometries, but the sensor will inevitably encounter new geometries when deployed in the real world.

In general, we have found optics to be a more robust transduction method compared to piezoresistivity. The sensitivity and accuracy of the optic sensors are superior to those of the resistive sensor. The signals extracted from the resistive sensor present a lower signal to noise ratio (SNR) and are inherently less sensitive when subjected to small strains compared to the optic counterpart. A small deformation on the optical sensor can result in a big signal change product of the frustrated total internal reflection effect, as well as the change in surface normals. Additionally, the resistive sensor, as reported in the literature [14] and confirmed by our experimental data, is affected by hysteresis and must rely on baseline measurements. In terms of wiring, if optic components are deployed on a board - rigid or flexible - then common buses can be used for power and ground, greatly reducing the wire count for the sensor.

When comparing the optic sensors with the MEMS tactile dome presented in chapter 5, the possibility of using "pair measurements" with optics provides a clear advantage when it comes to the richness of data we can extract. Moreover, optical signals are more robust to external factors such as temperature, where the Takktile requires manual compensation for each individual sensor based on its particular temperature response. Takktile sensors digital nature and integrated signal conditioning circuitry, along with the possibility to connect multiple chips to a standard digital bus interface still makes them very attractive to build tactile sensors.

In this chapter, we demonstrate for the first time the ability to predict the indentation depth (a proxy for force). This capability is of great importance to build useful tactile feedback systems for manipulation tasks. The accuracy of depth predictions obtained with our optical sensors is very promising and can be traced back to the very nature of this transduction method. By leveraging the multiple modes of interaction between an indenter and the waveguide, we can obtain a sensor that is highly sensitive to both small and large forces. It must be noted that it is possible to adjust PDMS stiffness by changing the the ratio of curing agent to PDMS: the material is stiffer as we use more curing agent in the mixed solution before curing. Changing the stiffness of the material allows us to balance how much force is needed to achieve a certain deformation on the material. In turn, if our signals are sensitive to the underlying material deformation, this enables the tuning of the sensor dynamic range. Stiffness and PDMS layer thickness should be adjusted in conjunction to maintain a near-linear response since a stiffer PDMS layer will require a larger force to activate the second detection mode.

As was shown in this chapter, the distribution of the sensing terminals plays a fundamental role in the sensor performance. At this point the distribution for our sensors was decided based on intuition and simple heuristics in terms of covering the sensing area homogeneously. In the previous chapter we showed the use of simulation tools to aid the design of the sensor in terms of evaluating relative performance of different configurations without the need to build a physical sensor. Commercial FEA software allowed us to make that analysis with a strain-based transduction method. However, no equivalent software is available that could easily simulate our optical signals. Developing such a simulation could prove invaluable for us to further optimize this method.

A limitation shown in this chapter is the increasing computational cost of training traditional regressors (regularized linear regressors with non-linear kernels) as we increase the number of terminals in our sensors. The high dimensionality of our feature vector and the need for larger amounts of training data was addressed here with undersampling of our training data or using a multi-stage approach with specialized regressors. As we will see in the following chapter, a better solution is to transition to regressors based on neural networks which can handle the higher dimensionality that we encounter as our sensors grow more complex.

One of the key aspects we have yet to address is the adaptation of this method to arbitrary, non-planar geometries encountered in robot hands. We will tackle this in the following chapter.

Chapter 7: The DISCO Finger: Overlapping light signals in a multicurved sensorized surface

While our method is designed to be used with soft materials that can cover curved surfaces, the piezoresistive and optical prototypes shown in chapters 4 and 6 respectively were executed over planar surfaces. In this chapter, we will focus on the evolution of our optical sensor for three dimensional multicurved surfaces. We present a robotic finger exhibiting high tactile acuity over complex, multicurved surfaces, with no "blind" edges or corners, in a self-contained package with few wires, and ready for integration into complete manipulators. The result is what we call the DISCO Finger; an acronym for "Distributed Interleaved Signals for Contact via Optics".

Previous prototypes could be characterized as tactile "pads" because of their overall shape and lack of consideration for packaging. Here, we focus on optimizing for coverage, shape and packaging to build not a tactile sensor, but a *tactile finger*. From a coverage and shape standpoint, we believe it is paramount that a robotic finger provides a large sensitive area without hard edges or corners that can become blind spots. While not shown here, such a finger would allow to continuously sense rolling contacts, an important capability for in-hand dexterous manipulation

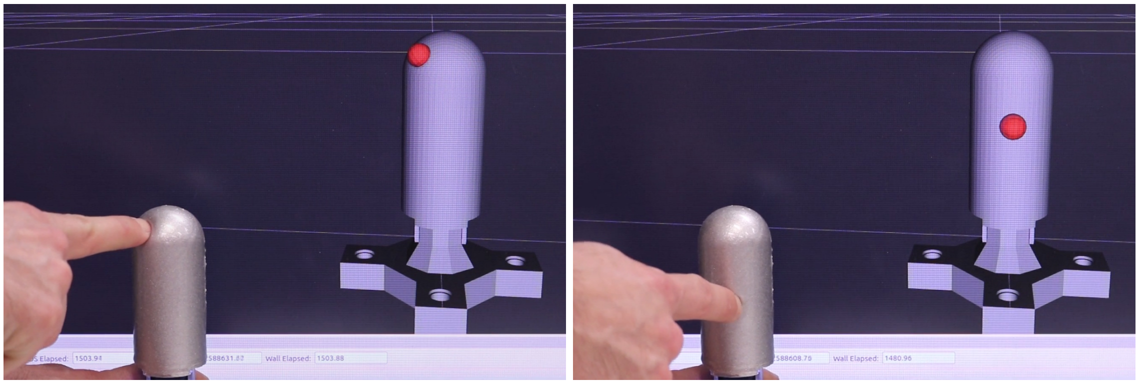

Figure 7.1: Touch localization and force detection for the DISCO Finger. Location of red sphere shows predicted touch location, and sphere radius is proportional to predicted normal contact force.

tasks.

The DISCO Finger (Figure 7.1) comprises a hemispherical tip attached to a cylindrical body. The sensorized areas of the finger include the complete hemispherical tip, and half the circumference (180°) of the cylindrical body. The finger comprises 32 LEDs and 30 photodiodes, giving us a total of 960 signals. As the finger makes contact with an external surface, many of these signals change, with the sign and magnitude of the change for each signal depending on the deformation of the transparent medium, as well as the relative position of the different LED and photodiode pairs.

We make use of this rich dataset with a purely data-driven approach, enabled by recent advances in machine learning allowing us to train regressors and classifiers on high-dimensional feature spaces, as is the case for this tactile finger. We use this data to train models for predicting contact location(s) and normal force based on the optical signals recorded by the finger. We use deep neural networks for both regression (for location and force) and classification (multitouch detection).

In this chapter we demonstrate the DISCO finger accuracy for contact localization, normal force prediction and robustness when encountering new indentations geometries. Additionally, we show it is possible to discriminate two independent contact locations, a new capability for our method. The result is a fully integrated tactile system packaged as a ready-to-use soft robotic finger with extensive coverage. We believe a robotic finger with such characteristics has not been demonstrated before and is a major step towards providing robot hands with tactile feedback capabilities.

7.1 Finger design and manufacturing

Finger geometry

We start with a 3D printed skeleton (Form2 Formlabs printer, standard clear resin) designed to be the distal link in a robot finger. This skeleton provides a base on which we will mount our individual sensing terminals (LEDs and photodiodes). The geometry of our finger is informed by the requirements of the task as well as intuition. We chose the outer geometry (including the

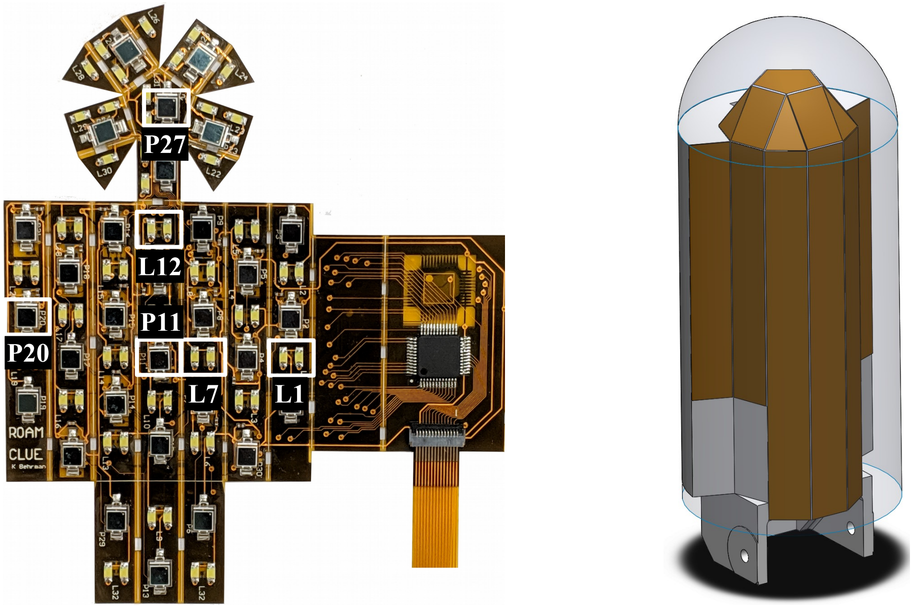

Figure 7.2: Flexboard with LED and photodiodes, as well as CAD showing flexboard wrapping on rigid finger skeleton and covered by 7 mm transparent layer. Three LEDs (L1, L7 and L12) and three diodes (P11, P20 and P27) are identified, as they will be referenced in later figures.

transparent layer) to be appropriate for a finger operating clutter, maximizing the sensorized area while avoiding sharp edges and corners, which are not conducive to creating stable contacts. The outer shape thus consists of a 36 mm diameter hemisphere, mounted on a cylindrical base of the same diameter and 72 mm height.

Our goal for the functional area of the finger (the area where touch can be sensed) was to avoid any blind spots in areas likely to make contact. We thus selected as an active area the complete tip hemisphere, as well as 180° around the circumference of the cylindrical body. The only "unsensed" area of the finger is the back (half the circumference) of the cylindrical part. The transparent waveguide layer extends throughout the sensorized area of the finger. Based on previous experiments on planar prototypes [130], we selected 7 mm as the thickness of the transparent layer.

The rigid skeleton acts as a foundation for the transparent layer, as well as a support for the LEDs and photodiodes. All the electronic components are mounted on the flexible circuit board (flexboard) shown in Figure 7.2. Since most of the components require locally flat mounting areas, the flexboard alternates flat strips (enforced with stiffeners) with flexible "creases", leading to an

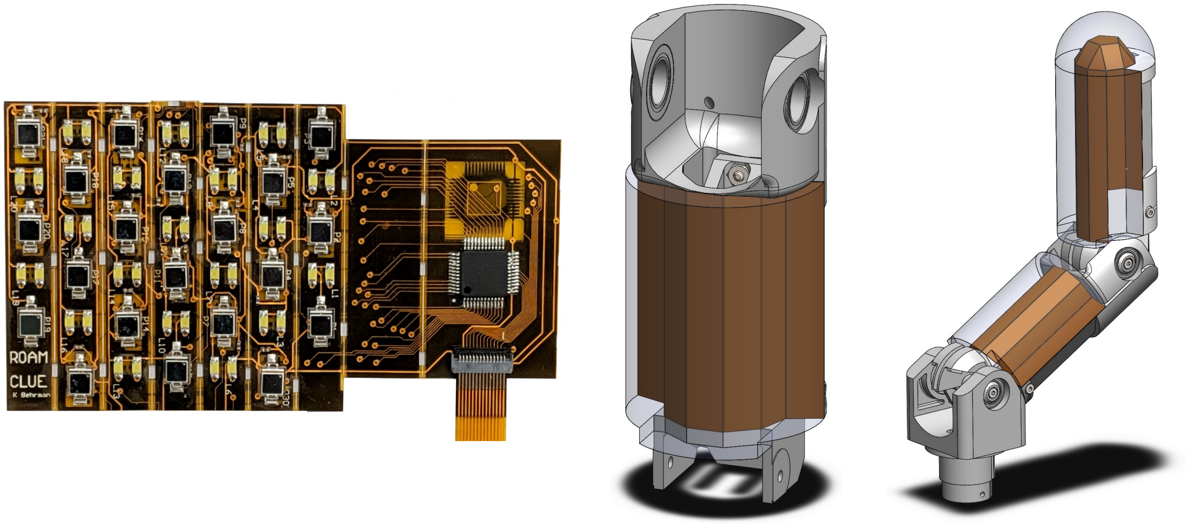

Figure 7.3: **Left:** We can cut off the top and bottom sections of our flexboard and maintain full functionality of the remaining components. **Middle:** The resulting flexible board can be used to build a tactile proximal link. **Right:** An articulated robotic finger design with tactile sensing on both proximal and distal links.

origami-like design. The rigid skeleton is designed with flat facets to accommodate this flexboard geometry. These flat faces follow the smooth curvature of the finger surface above, and thus the electronic components radiate and receive most light in the same direction as the surface normal. Two faces are the exception to this rule, as they are oriented in a way that LEDs will radiate light parallel to the surface instead of normal to it. Light emitted in this way can travel all the way to the other side of the finger as it bounces through the reflective coating, providing us with a subset of signals with larger spatial coverage.

Additionally, we have designed the flexboard such that the top and bottom sections can be cut off while maintaining full functionality of all the remaining components. The flexboard folds along the proximal rigid skeleton in a similar fashion as in the distal link case as shown in Figure 7.3, Center. Figure 7.3, Right demonstrates a complete 2-link robotic finger system using our flexboard design. The fact that we can utilize the same flexboard design for both the distal and proximal links helps reduce the manufacturing costs and makes our hardware design process more streamlined by not having to maintain different designs for each link. For the rest of this chapter we will focus on analyzing the distal link design as a stand-alone robotic finger.

Figure 7.4: DISCO Finger through various stages of construction. We 3D-print a rigid skeleton, on which we attach a flexible circuit board with light emitters (LEDs) and receivers (photodiodes). We then mold a 7 mm thick transparent layer acting as a waveguide. Finally, we add a thin reflective outer layer.

Manufacturing

The first manufacturing step is to glue the sensor board to the skeleton. We use a cyanoacrylate adhesive to bond the flexboard to the skeleton and then we connect a 380 mm flat flexible cable (FCC) to the backside of the finger. Once the flexboard is bonded, we treat all the surfaces with silicone primer (MG Chemicals SS4120) to promote bonding of the transparent waveguide layer to the skeleton and sensor board.

The next step is to cast the transparent layer, for which we use Polydimethylsiloxane (PDMS). We use a two-part mold that the skeleton fits inside, and which provides the outer geometry of the finger. The stiffness of the elastomer can be adjusted by changing the ratio of curing agent to PDMS. We prepare the main layer of elastomer with a ratio of 1:30, which we empirically observed to produce a stiffness of approximately 2.8 N/mm. It is desirable for this first layer to be soft because our signals are proportional to surface deformation; thus, the softer the material, the less force is required to achieve a deformation that our electronics can detect. The material stiffness should be tuned such that it is soft enough to produce noticeable deformation with small forces, but stiff enough that forces encountered during normal manipulation tasks will not damage the underlying sensor board.

After mixing the PDMS with the curing agent, we degas the solution until no more air bubbles are visible. We pour the solution into the previously prepared mold, which has been treated with a release agent (Mann Ease Release 200) and degas once again to eliminate any bubbles that may have formed while pouring the solution. We cure the PDMS in an oven at 80 C for 6 hours. After the curing process is complete, we gently remove the finger skeleton from the mold to obtain a fully clear finger as shown in Figure 7.4.

To complete the finger, we add a thin outer layer with a dual purpose: this layer reflects back into the transparent elastomer light that otherwise might refract out, and blocks ambient light. Drawing inspiration from the GelSight sensor [66], we use a reflective powder (Bronzing Powder #242 from Douglas and Sturgess) which contains copper, zinc and stearic acid. After demolding the finger we use a soft makeup brush to apply the reflective powder onto the PDMS surface, then add an additional thin PDMS layer. This additional layer has a 1:10 ratio of curing agent, as well as 1% by weight reflective powder mixed in. We use a stiffer material in this exterior layer to replicate human fingers, where the skin is much stiffer than the flesh underneath. We add this layer via dipping the finger in a vat, followed by curing at 80° C for 40 minutes. The process of adding the reflective powder onto the PDMS, followed by an extra PDMS layer to protect it is repeated two more times.

Sensor board and electronics

The flexboard contains 57 individual LEDs (Bivar SM0805UWC, chosen for their high intensity and Lambertian distribution), 30 photodiodes (Osram BPW 34 S E9601), 15 operational amplifiers (AD8616) on the backside, two 32 channel multiplexers (ADG732) and one FFC connector with 14 positions (Hirose FH34SRJ-14S). Many of the Bivar LEDs are grouped in pairs, comprising 2 units placed 2 mm apart and wired together. Such a pair is the logical and functional equivalent of a single LED with a larger surface area. We refer to such pairs as simply "one LED" for the rest of the chapter. Using this convention, our board comprises a total of 32 "logical" LEDs. Since we only turn on a single LED pair at a time, and with each LED drawing 20 mA, our board uses a total of 200 mW power during operation.

Similarly, we selected our photodiode for its large active sensing area of 7 mm^2. We aimed for large surface areas in both our light emitters and receivers in order to obtain a smooth response as light paths are altered by the presence of an indenter (as opposed to a binary-like signal that occurs when a small area emitter or receiver is blocked or revealed). Each photodiode signal is amplified using a transimpedance amplifier with a feedback resistor of 249 kOhms.

In order to measure the light transmitted between each LED and each diode individually, we use one multiplexer to select which LED to drive and the other multiplexer to select which photodiode to read. We turn on one LED at a time, and read the signals from all photodiodes. We also take an additional reading of each photodiode with all LEDs turned off, in order to account for any traces of ambient light that might have penetrated our outer layer. In this iteration of the sensor, we can record all the ensuing 960 signals at a rate of 57 Hz.

Since we measure light transport between each LED and each photodiode, we want to ensure that the light emission from each LED is bright enough to reach distant diodes, but also that it does not saturate nearby diodes. We thus use an additional AD8616 operational amplifier to amplify the output of the Teensy digital to analog converter (DAC) such that we can control the brightness when driving each individual LED. For every LED/diode pair, we choose a dedicated amplification level such that the response of the diode in the undisturbed state of the finger is close to the middle point of the diode's output range in a process we call "equalization". This ensures that, in the presence of deformation, each of our signals has "headroom" to either increase or decrease, depending the position of the LED and diode relative to the indenter.

7.2 Surface parametrization

In previous planar sensors the encoding of a location was trivial using two coordinates representing the distance in millimeters of the location to an arbitrary origin point. In contrast, the surface of the DISCO Finger finger is a (multicurved) two-dimensional manifold (embedded in three dimensions).

A naive approach would be to encode locations using Cartesian coordinates (x, y, z). With this approach, we are asking our regressor to not only learn the mapping between the optical signals and the location of touch, but to also learn the surface manifold of our finger. We would also need to deal with predictions that inevitably will fall outside our manifold and require some sort of projection onto the finger surface. Perhaps a more suitable approach would be to use polar or spherical coordinates with the caveat of having special constraints based on if the location is part of the finger hemispherical tip or in the cylindrical region that make up the rest of the finger. However, both a polar or spherical mapping present singularities and distortions, as a regular grid in those 2D (polar) or 3D (spherical) subspaces will not translate to a regular grid on the finger.

With this in mind, we choose to parameterize the finger surface using a similar mapping to the one presented in chapter 5 with two dimensionless variables (A, B). We use the surface parameterization introduced by Roşca[126] for spheres, which we modified to also cover the cylindrical component of our finger (see Appendix A). The resulting parameterization, illustrated in Figure 7.5,

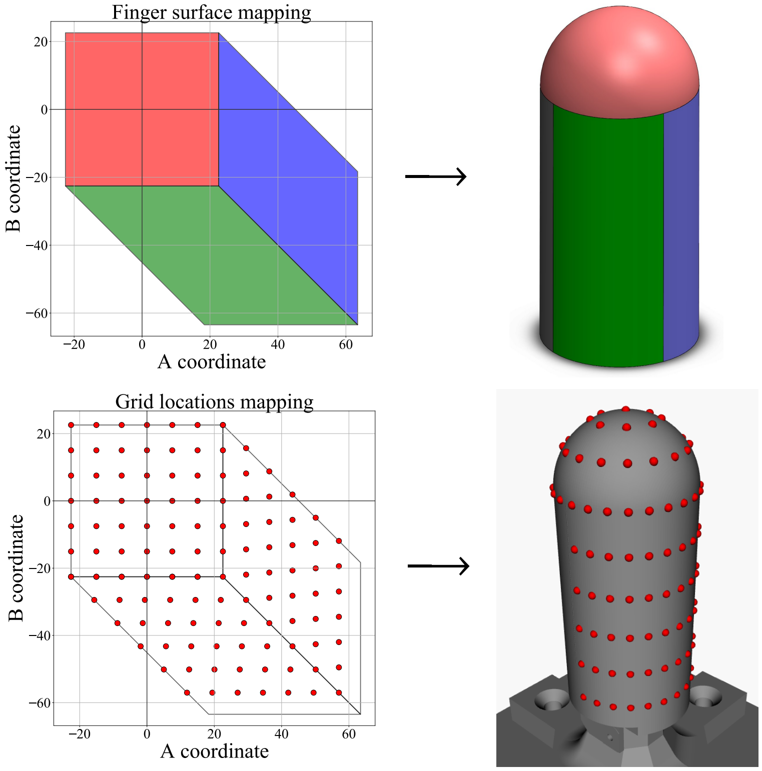

Figure 7.5: Finger surface parameterization into two-dimensional (A, B) space. **Top:** Finger is divided into three color-coded areas; each area maps to its corresponding color in (A, B) space. Parameterization is continuous throughout the functional area of the finger, has no singularities, and attempts to preserve local surface area. **Bottom:** A uniform grid in (A, B) space is mapped to a uniform grid on our finger sensorized area.

avoids singularities and aims to preserve distances uniformly across the sensorized surface of our finger. This trait is particularly attractive as it allows us to sample locations homogeneously in the AB subspace knowing this will result in an almost equally homogeneous distribution of locations on the finger surface. Figure 7.5, bottom shows the result of mapping a uniform grid in (A, B) space to the finger surface.

For the sake of readability, we will use this two-dimensional (A, B) space to show some of our results in terms of prediction error and signal behavior.

7.3 Light transport and hysteresis

Much like our previous optical sensor, the DISCO Finger is constructed using LEDs and photodiodes embedded in a clear elastomer which acts as a waveguide. In the previous chapter, we rely solely on total internal reflection to guide light inside the elastomer. This meant that light rays hitting the surface of the sensor at angles greater than 45 degrees would not be reflected back into the sensor.

Our design and geometry for the DISCO finger means that our sensing terminals radiate and receive most light in the same direction as the surface normal. To avoid the leakage of this light and to enhance the light guidance inside the finger, we decided to add a reflective coating which allows light to travel a considerable distance inside the finger. Each LED/photodiode pair has a signal associated to it, represented by the amount of light received by the respective photodiode from the respective LED, and a receptive field, represented by the area on the elastomer that can be disturbed to produce change on this signal.

Figure 7.6 illustrates the concept of a receptive field (in (A, B) space) for a number of representative LED/diode pairs using data collected from the finger. As these receptive fields overlap over the same areas of the finger, we can expect more signals to respond to a touch event in that particular location.

To evaluate hysteresis in our signals, we collected data when indenting the same area at slow and high speeds (as high as our instrumentation equipment allows). Figure 7.7 shows a represen-

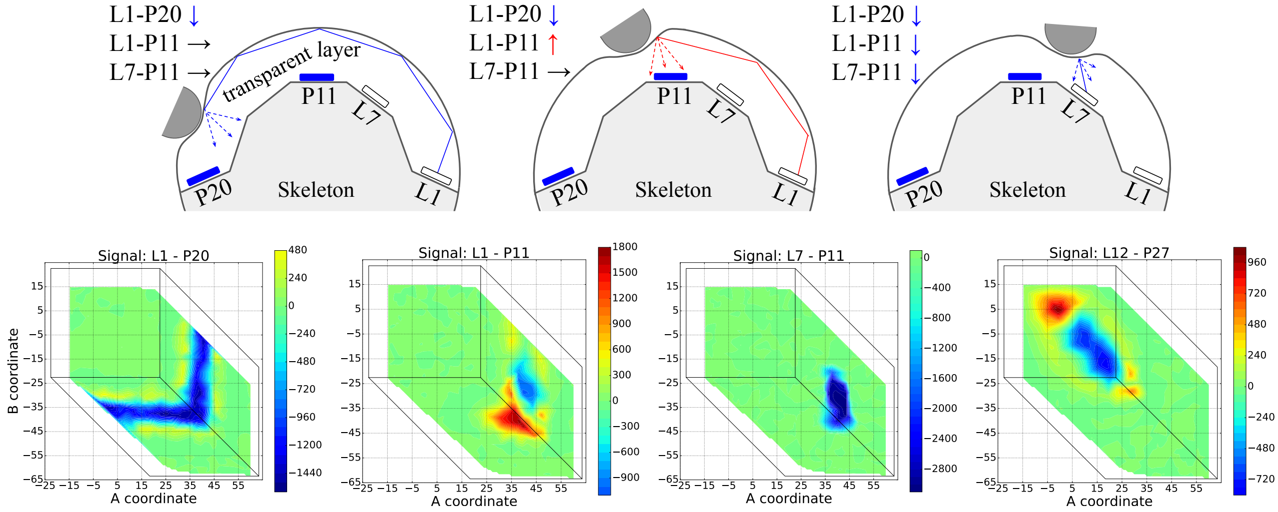

Figure 7.6: Receptive fields for tactile optical signals. **Top:** illustration of light transport through transparent layer. Each LED-photodiode pair provides one signal; indentations cause different signals to change in different ways. **Bottom:** Real data from our sensor showing how various signals are affected by indentations, based on location (using the (A, B) parameterization from Figure 7.2). For each signal, the heatmap shows the change in raw value caused by an 4 mm deep indentation with a hemispherical tip of 10 mm diameter. The flexboard locations of all LEDs and diodes referenced here are marked on Figure 7.2.

tative hysteresis plot, collected for raw signal L1-P20 on two indentation-release cycles performed at different velocities in the middle of the receptive field for that signal. This plot shows little hysteresis on our signal, but it is possible a more dynamic event could result in a more hysteretic response. We believe that most manipulation tasks that require incorporating any type of tactile feedback are likely to have slow dynamics such that the hysteresis inherent with using an elastomer based finger can be ignored.

7.4 Data collection

For our data collection we use a Universal Robot UR5. We design a custom end effector mounting for a linear actuator (Physik Instrumente M-235.5DD) which is fitted with a load cell at its end to record force measurements (Futek LSB205 10 lbs). At the other end of the load cell we can mount multiple tips with different geometries. Our data collection setup is shown in Figure 7.8.

To collect training and testing data we probe the finger at random locations with different tips

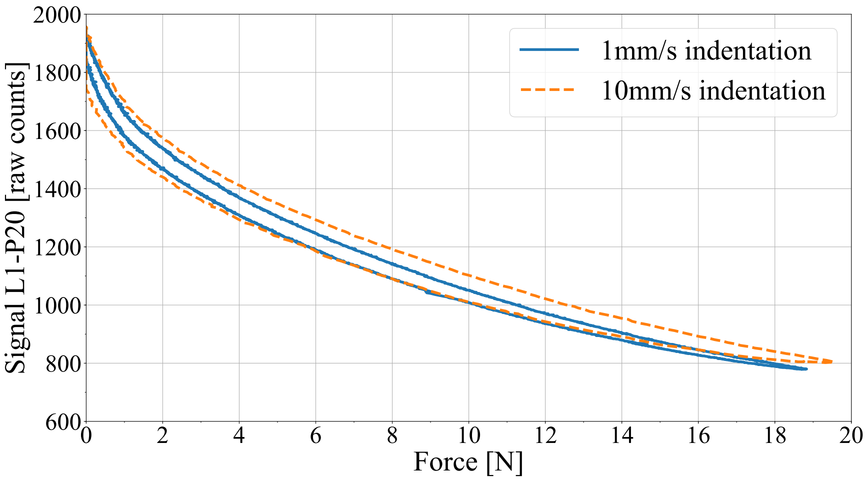

Figure 7.7: Hysteresis plot showing two indentation-release cycles performed at different speeds. In each case, the line with a larger raw signal corresponds to the indentation, and the line with a lower raw signal to the release.

mounted on our load cell. These random locations are sampled from the defined (A, B) region that represents our sensorized finger surface. It must be noted that all indentations for this study are normal to the finger surface. We define a dataset to contain 100 random locations spread throughout the region in (A, B) space, with the caveat that we enforce a minimum distance of 4 mm between locations to explore the full surface more homogeneously. (Any new randomly selected location is rejected if it closer than 4 mm to another sample in the same dataset.)

For every location in the (A, B) region we follow the same procedure. We use the parameterization described above to go from the (A, B) location to its corresponding Cartesian coordinates, and compute inverse kinematics for the robot to reach that point in space. The robot positions the indenting tip normal to the surface at a distance of 20 mm. At this point we advance the probe until we find the finger surface using the force measurements from the load cell. Having established the finger surface we start logging data from a depth of -1 mm (negative depths should be interpreted as the tip being above the surface) to 3 or 4 mm (depending on the tip being used) in 0.1 mm intervals. Indentations with the planar tip can only go to a depth of 3 mm to avoid exceeding the load cell maximum force rating (10 lbs). This procedure yields 51 measurements at different depths for every location, hence a dataset with 100 locations constitutes 5100 data points.

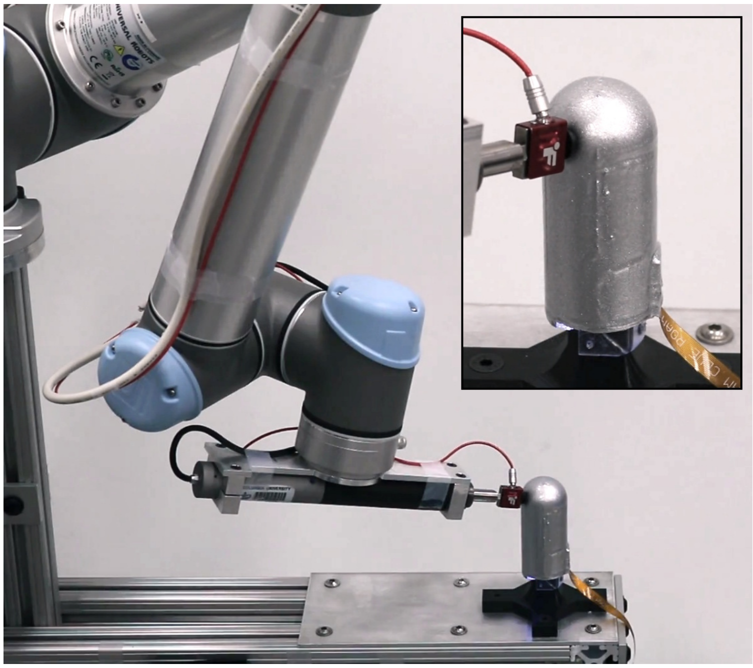

Figure 7.8: DISCO Finger data collection setup

Each measurement i results in a tuple of the form $\Phi_i = (a_i, b_i, d_i, f_i, tip, r_1, .., r_{990})$ where (a_i, b_i) is the indentation location in AB space, d_i is the depth at which the measurement was taken, f_i is the measured force in newtons, tip is the id corresponding to the indenter geometry used and $(r_1, .., r_{990})$ is the vector with dimension 990 containing all light measurements between all 32 LEDs and 30 photodiodes and an additional 30 measurements which correspond to turning off all LEDs and measuring any traces of ambient light received by each photodiode, which is then subtracted from the main 960 signals.

Using this dataset, we checked how many of these raw signals carry useful information. We consider a signal as useful if, in response to an indentation anywhere on the finger surface, the signal changes by more than three times its own standard deviation in the undisturbed state (used as a measure of noise). We found that 917 our of 960 signals exceed this threshold, confirming the hypothesis that our overlapping signals approach leads to a large number of useful signals.

To collect data where the finger is potentially touched in multiple locations, we revert to a manual procedure. We divide the cylindrical part of the finger into a 4×5 regular grid. For one data point, a human experimenter contacts the finger in either a single cell, or simultaneously in two cells, chosen at random. Contact is made in all cases with hemispherical indenters (10 mm diameter). Each measurement i thus results in a tuple of the form $\Phi_i^{multi} = (c_1, .., c_{20}, r_1, .., r_{990})$, where c_j is a binary signal indicating if cell j is being contacted, and the feature vector $(r_1, .., r_{990})$ comprises tactile finger signals as above. We note that contact forces are not measured in this case.

7.5 Learning algorithms

For all experiments on our finger, we use feed forward neural network architectures. The architectures are slightly customized to support the related task. First, we describe the architecture for contact localization and force detection, followed by the neural network for multi-touch detection.

For localization and force prediction, we use a multi-task neural network with five hidden layers. Each hidden layer uses batch normalization and the ReLU activation function. The first three hidden layers are shared between both tasks, with 512, 256 and 128 activation units respectively. Afterwards, each output has two individual hidden layers with 64 and 32 hidden units respectively (Figure 7.9). We use mean squared error as a loss function. The network is trained for 600 epochs with ADAMoptimizer, a batch size of 128 and an initial learning rate of 0.001. After 500 epochs the learning rate is decreased to 0.0001. For localization prediction, the training dataset is filtered to only use positive depth, because the network cannot be expected to predict location when touch is not occurring.

Collecting precise multi touch data would require two robotic arms operating on the same finger without colliding each other, simultaneously. In the absence of such a setup, we used a simpler manual procedure. We divided a section of the finger into a 4x5 grid cell (in total 20 cells) and collected data via manual indentation. The training process randomly selects one or two out of the 20 cells and shows their identity to the experimenter. The experimenter then indents the respective cells, and records the ensuing tactile data. We note that exact contact force is unavailable when using this procedure.

The resulting dataset is one order of magnitude smaller than the ones obtained with our automated process and, therefore, a simpler neural network is required. For multi-touch prediction,

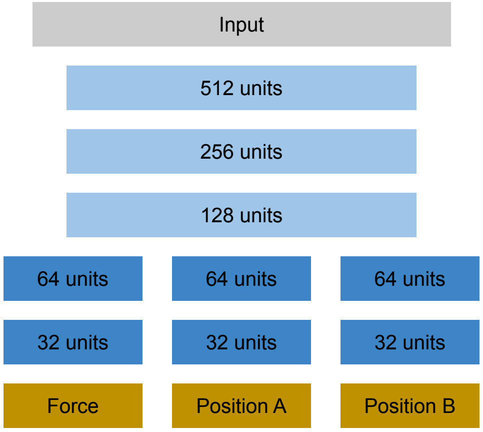

Figure 7.9: Neural network architecture. We use a multi-task neural network with five hidden layers. This sketch shows the number of neurons on each layer as the data flows from input to the final three values of interest: force and location, the latter being parametrized with values (A, B).

a two hidden layer feed forward neural architecture is used with 128 and 32 hidden units respectively. The hidden layers use the ReLU as activation function, but no batch normalization. The output consists of 20 independent binary predictions, each indicating the probability of touch for a certain cell. For this task, we used the sigmoid cross entropy loss. The network was trained for 400 epochs with ADAMoptimizer with a batch size of 128 and initial learning rate of 0.001, which was reduced to 0.0001 after 200 epochs.

7.6 Touch localization and force detection.

We first quantify the ability of our finger to predict the location of touch, i.e. where on the surface of the finger touch is occurring. We perform this test on a corpus comprising 4,896 indentations at 96 different locations and with different forces. Figure 7.10 shows the localization error at different force levels over the entire test set (mean and median). Note that while our prediction is made in the dimensionless (A, B) space, we first convert both the prediction and the ground truth location back to Cartesian (x, y, z) space in order to calculate the error in distance units (mm). We also note that the smallest force that our load cell can accurately detect is 0.2 N, and any force measurement below that value indicates either no contact, or very slight touch.

We observe that our finger quickly achieves sub-millimeter accuracy in touch localization, once

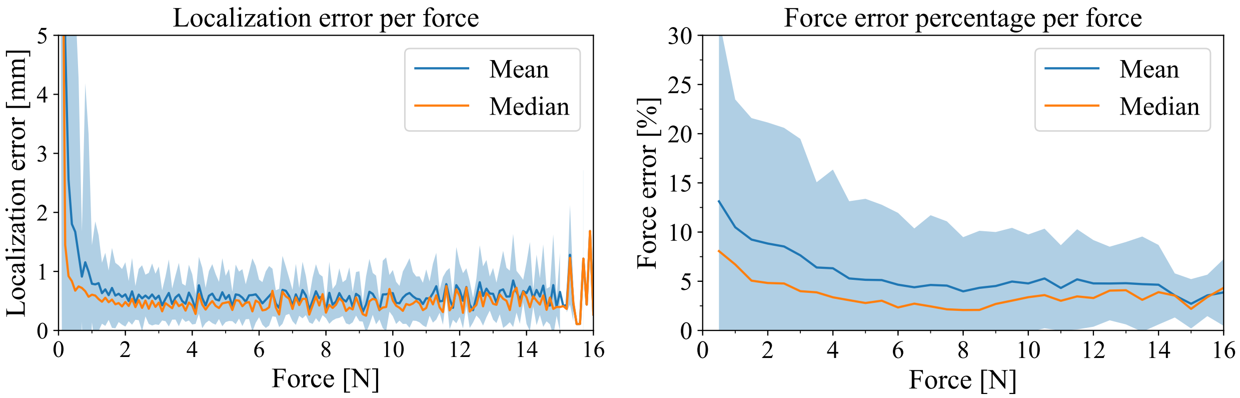

Figure 7.10: Aggregated localization and contact force prediction error. All plots show mean and median values, computed over all finger locations that we have tested. **Left:** absolute localization error, by measured contact normal force. **Right:** relative normal force prediction error as a percentage of measured normal force, by measured normal force.

the contact force exceeds 0.2 N. The error continues to decrease until a force level of approx. 1 N, at which point performance stabilizes throughout the rest of the range of forces we tested. At 0 contact force (no touch), the localization error is 30.3 mm (median), in line with a random chance guess.

We now turn our attention to the ability to also predict normal contact force. Using the same datasets as before, we train a neural network regressor to predict contact normal force, using load cell data as ground truth. The error as a percentage of the ground truth applied force is shown in Figure 7.10, for different contact forces.

We note that the relative error is below 10% (median) even for very light touches, and reduces to as low as 2% (median) in the middle of our range (around 8 N). At that point, relative error stabilizes around 3% (median) and 5% (mean) for the rest of the range, up to 16 N.

For more insights into how localization performance varies across its surface, we would like to study if the magnitude or direction of the error is affected by the area of the finger that is being touched. Figure 7.11 shows this error for every data point, grouped by force levels. For clarity, this data is shown in the two-dimensional (A, B) space, as illustrated in Figure 7.5 and formally defined in Appendix A. We notice that at no contact and below a force level we can reliably detect (0 to 0.2 N), errors are in line with random guesses. At low forces (0.2 to 0.5 N) most of the functional area

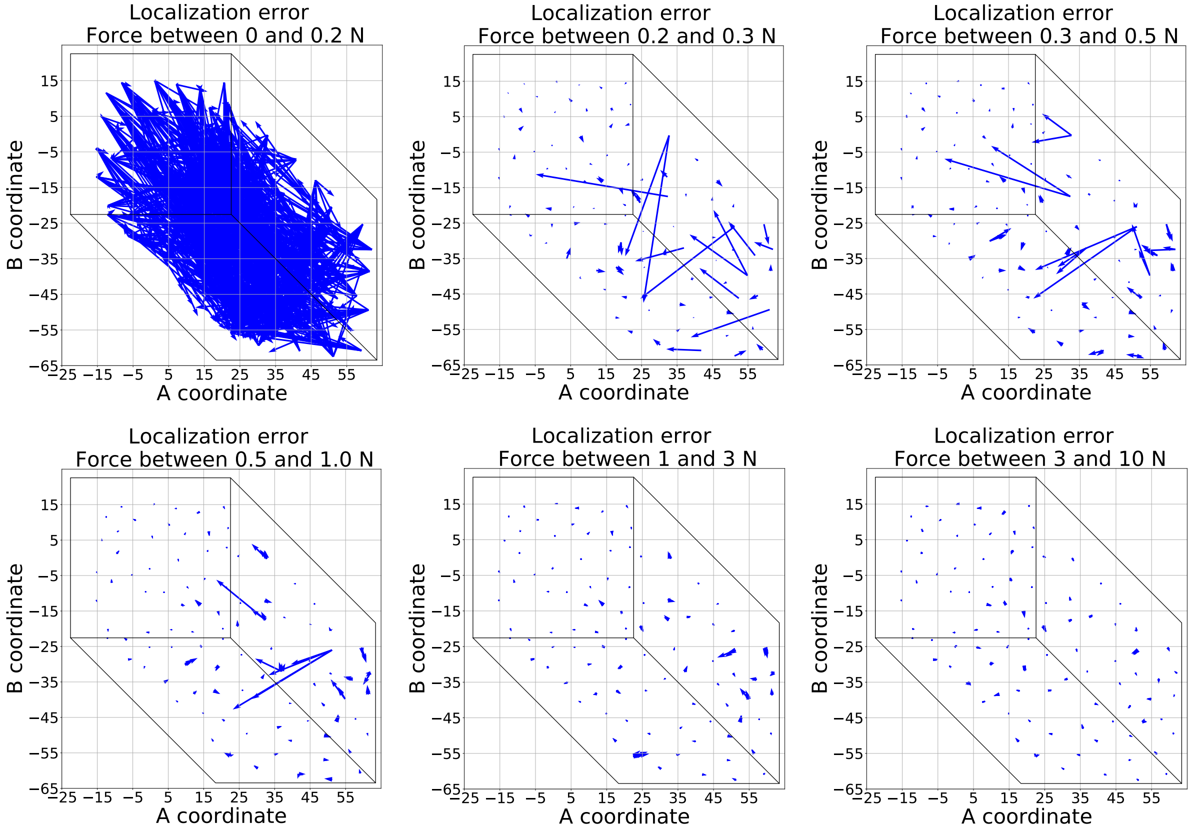

Figure 7.11: Localization prediction error for each test point, shown in the (A, B) space illustrated in Figure 7.5. For each test point, we render an arrow; the base of the arrow shows the true location of touch, while the tip of the arrow shows the predicted location; a shorter arrow thus corresponds to lower error. We bin test points together based on applied force, with each plot corresponding to data from one bin, as indicated in the plot title.

of the finger has good accuracy, with most large errors occurring along the edges of the cylindrical part. For forces beyond 1 N, larger errors have been eliminated throughout the functional area.

7.7 Robustness to indenter shape.

The results shown so far have been obtained by using a single indenter tip. What happens if the shape of the indenter varies? Furthermore, what is the performance level if, at test time, the finger makes contact with an indenter different from the one(s) using during training? These analyses would be indicative of performance in complex environments, where the robot might interact with objects of varying, and potentially unknown shape, and in various configurations.

To evaluate this performance, we collected data using multiple indenters. In addition to the 10

Table 7.1: Localization performance with multiple indenter shapes. For each indenter, we show localization error for two models: one trained without data from the indenter being tested ("Leave-one-out") and one trained with data from all indenters ("All inclusive"). We report performance aggregated over five force intervals; for each force interval, we report the mean and median localization error. Last two rows show performance averaged over all indenter shapes.

Tip	**Model**	Error (mm) for forces 0.2-0.3 N		Error (mm) for forces 0.3-0.5 N		Error (mm) for forces 0.5-1.0 N		Error (mm) for forces 1.0-3.0 N		Error (mm) for forces 3.0-10 N	
		Mean	Median	Mean	Median	Mean	Median	Mean	Median	Mean	Median
Edge (H)	Leave-one-out	13.0	7.5	8.3	4.0	4.2	2.5	2.5	1.7	3.7	2.1
	All inclusive	7.8	2.9	3.2	1.9	1.6	1.2	1.0	0.9	0.8	0.7
Edge (V)	Leave-one-out	12.6	13.0	6.8	6.3	3.8	3.3	3.0	2.9	1.8	1.7
	All inclusive	2.8	3.6	2.7	3.2	1.6	1.6	1.1	1.1	0.8	0.9
Planar	Leave-one-out	7.5	3.3	5.6	2.7	2.8	2.0	1.9	1.5	1.5	1.3
	All inclusive	1.2	0.9	0.9	0.8	0.7	0.6	0.6	0.5	0.6	0.5
Spherical	Leave-one-out	4.5	2.0	3.1	1.8	2.4	1.3	2.1	1.2	2.5	1.4
	All inclusive	1.2	0.9	0.9	0.8	0.7	0.6	0.6	0.5	0.6	0.5
Corner	Leave-one-out	2.7	1.6	1.7	1.3	1.4	1.1	1.2	1.0	1.4	1.1
	All inclusive	1.2	0.9	0.9	0.8	0.7	0.6	0.6	0.5	0.6	0.5
Average	Leave-one-out	8.1	5.5	5.1	3.2	2.9	2.0	2.1	1.7	2.2	1.5
	All inclusive	2.9	1.8	1.7	1.5	1.1	0.9	0.8	0.7	0.7	0.6

mm diameter hemispherical tip used so far, we added a planar tip (circular with a 15 mm radius), a sharp corner, and an edge used in two different orientations (horizontal and vertical), for a total of five different indentation geometries. We used this data to test localization performance with two different approaches.

First, in order to test performance for an indenter shape not seen during training, we used a leave-one-out procedure: for any indenter tip, we trained a regressor (similar to the one used before) on data from all the other tips in our set, but excluding the tip being tested. We then checked localization performance on the tip that had been excluded from training. The second approach aimed to test how performance generalizes over multiple indenter shapes, assuming data from each indenter is available for training. We thus trained one model on data from all five indenters, and tested this all-inclusive model on separate test data from each tip. Results for both conditions are shown in Table 7.1.

We notice that high localization accuracy generalizes to multiple indenter geometries. If data for all indenters is available for training, even light touch can be localized with <3 mm median accuracy for 4 out of 5 indenters, further reducing to sub-mm as contact forces increase. Even when the finger is contacted by a never-seen-before indenter, it can localize touch well, as long as the model has seen indenter shape variations in training. Performance increases with normal contact force, with 2 mm or lower median localization error typical for never-seen-before indenters once force exceeds 0.5 N.

7.8 Detection of multiple touch points

Finally, all of our results so far assume a single touch point on the finger. Such an assumption is applicable in some real-life cases (e.g. a hand manipulating objects that are convex or locally convex), but can be limiting. What happens if the finger is contacted in multiple locations?

We divided the cylindrical part of the finger into a 4x5 regular grid. We then collected a multitouch dataset using a manual procedure as stated in section 7.4. The signals from our finger were recorded, along with the ground truth identity of the cells being touched. We recorded a total of 1,987 data points using this procedure, which we split into a 1,635-point training corpus and a 352-point testing corpus.

Using this data, we trained a classifier to predict, based on the tactile signals, if each of the 20 cells was being touched. Thus, for each cell, this predictor output a continuous probability that the respective cell was being touched. We then tested the performance on our testing corpus. For each entry in the test set, we considered the classification as correct if, for every cell marked as touched or untouched in the ground truth data, the predicted touch probability was above or below 0.5, respectively. Over our complete testing set (comprising cases with both one and two simultaneous touches), the classification accuracy using this rule was 96%. When considering only cases where the finger was simultaneously touched in two locations, the classification accuracy was 93%. Figure 7.12 illustrates our data collection procedure for this case, and shows a number of representative examples for our touch predictor.

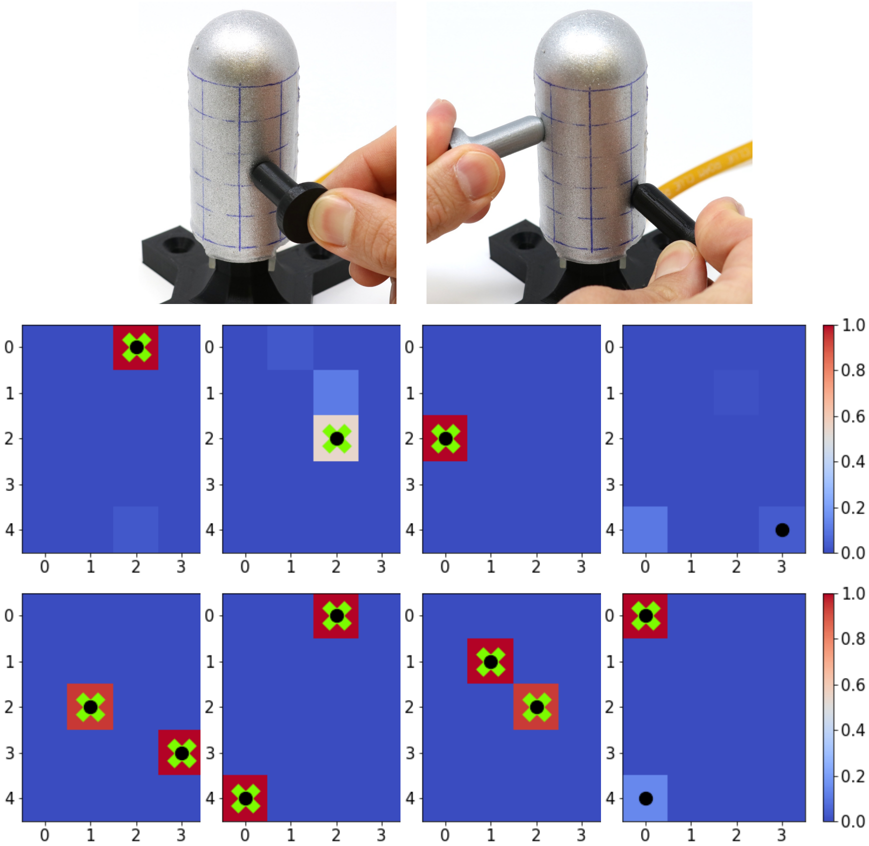

Figure 7.12: Multitouch prediction results.**Top:** finger with a 4x5 discrete grid marked on cylindrical area, and experimenter manually indenting one or two cells simultaneously; our model aims to predict the number and identity of indented cells. **Bottom:** examples of multitouch predictions from our model. Each image shows one test case; black dots indicate ground truth identity of indented cells. The color of each cell indicates the predicted probability of touch in that respective cell, using the color map shown in the right. Cells where the predicted touch probability exceeds 0.5 are marked by a green cross. Rightmost images in each row are examples of incorrect classifications.

7.9 Discussion

The main contributions of this chapter can be summarized as follows:

- We introduce the first multicurved robotic finger that can localize touch with sub-millimeter accuracy and also accurately determine normal contact force over a large (6107 mm^2) non-developable three-dimensional surface (such as a cylindrical body with a hemispherical tip), in a fully integrated, finger-shaped package.

- We show that our spatially overlapping signals methodology is able to capture multi-touch contact events, a capability we had not shown in our other data-driven sensors. This experiment shows that the rich optical signal dataset extracted from our sensor contains enough information to perceive more complex deformation states on the finger surface than a single indentation event.

Overall, the results confirm our main hypothesis: the overlapping optical signal set contains the information needed to determine both the location and normal force of the indentation with high accuracy, and throughout the multicurved functional surface of the finger. We can generally determine contact location with sub-millimeter accuracy, and contact force to within 10% (and often with 5%) of the true value. These results cover the complete hemispherical tip of our finger, as well as half the circumference of its cylindrical base. To the best of our knowledge, this level of accuracy, obtained over the multicurved non-developable surface of a finger-shaped package, has not been previously demonstrated.

Furthermore, these results exhibit low sensitivity to the shape of the indenter used for contact. By training with multiple shapes we can achieve predictors that perform well on never-before-seen indenters, keeping the localization error below 3 mm (and in many cases below 1.5 mm) for shapes not seen during training.

Finally, our method lends itself to packaging in a form suitable for integration into complete systems. This is due to both the overlapping signals approach (providing a very rich signal set, with cardinality quadratic in the number of individual sensing terminals) and our use of multiplexing-though-time (further reducing the wiring needs, while maintaining an operational frequency of 57 Hz). The results above were obtained with a self-contained finger with a compact wiring interface (single 14-wire FFC). Furthermore, our approach is characterized by simple manufacturing, and accessible cost (approximately $350 per finger in low quantities), all of which as critical enablers for integration into dexterous manipulators

To illustrate the possibility of integration into a complete robot hand, Figure 7.13 shows a dexterous robot hand using three fully integrated tactile fingers. A finger consists of a proximal

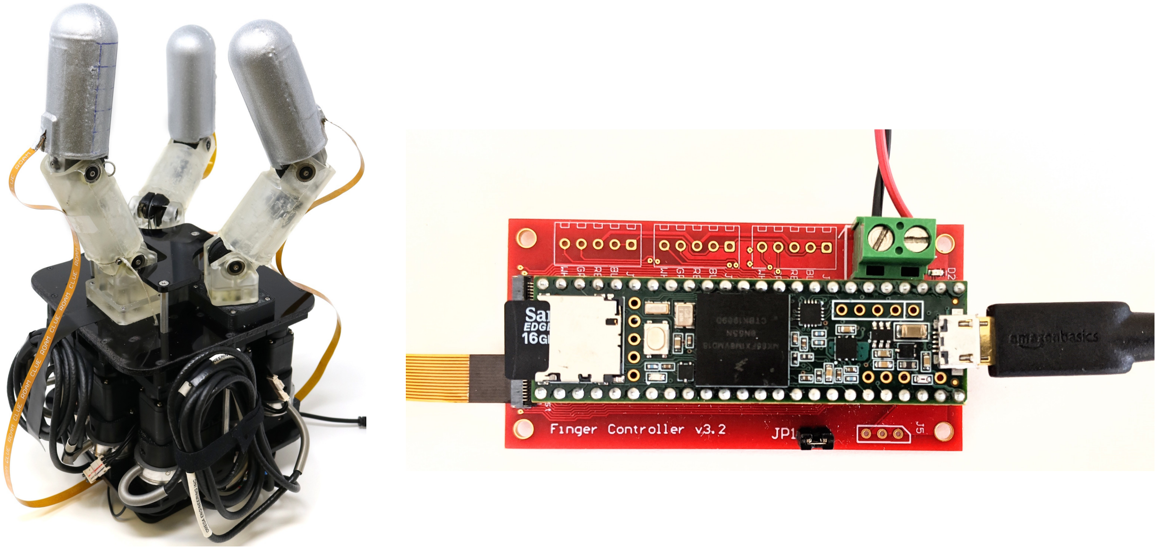

Figure 7.13: Sensor integration. A dexterous robot hand using three of the fingers presented in this chapter (Left). The sensors are fully integrated, with each finger connected to a finger controller board (Right) housed in the palm. The palm also houses eight motors, each equipped with torque sensors. The finger controller reads tactile signals, torque and handles communication with the servomotors. The controller communicates with a host PC through a USB cable using the rosserial protocol.

and distal links as demonstrated in section 7.1. Each finger is connected to a finger controller board housed in the palm. These finger controller boards are capable of servicing the two tactile links (each one connected to a different FFC connector). The finger controller reads all tactile signals, houses amplifying circuits for three torque sensors and handles communication with the servomotors that control that particular finger. This allows per-finger control based on both tactile and proprioceptive data running directly on the local control board; centralized control for all fingers must run on the computer that combines information from all three boards. The finger controller board uses the rosserial protocol to communicate to the host PC using ROS messages.

The performance level described above results from using a purely data-driven approach in the form of powerful regression and classification models, which allow us to extract information from a rich signal set without requiring analytical models. However, this approach also comes with inherent limitations. In particular, in order to explicitly predict a given characteristic of touch (such as location or a force component), one must explicitly train a predictor for it, using ground truth data. In the study presented here, this implies the use of an instrumented setup capable of measuring ground truth, and enough time dedicated to the collection of training data.

There are other characteristics of touch that we do not attempt to predict in this study. This includes shear forces and torsional friction. Given that, unlike pressure signals, our optical signals sense force only through deformation of the light-transporting medium, it is still unclear how sensitive they will be to shear (casual inspection does show signals are sensitive to shear). While other tactile sensors proposed in the literature do provide shear data, many of the most commonly used today do not (e.g. capacitive pressure arrays). Given touch location and normal force (both which our finger provides accurately), we believe that a complete system can partly compensate for the lack of contact shear force data by using torque sensing on the joints of the finger.

The most general way to encode information about a contact patch of arbitrary shape is as a pressure distribution over the entire finger surface. Such a method can generalize to an arbitrary number of simultaneous contacts. However, due to the difficulty of collecting ground truth data for such a predictor, we do not show this ability here. We believe however that the information characterizing the full state of the skin surface deformation is contained in the rich overlapping optical signal set. This hypothesis is also supported (though not yet fully confirmed) by the ability shown in this study to distinguish multiple touch locations.

The nature of soft contacts and the complexity of parameterizing touch are two of the main reasons why making effective use of tactile data has proven to be so challenging. With the DISCO Finger we offer the user the choice to train a model that extracts the tactile features believed to be the most relevant for a task (in our case, contact location and normal force). The possibility of processing the raw optic signals directly, without intermediate representations or “features” such as force or location can be very enticing, as it removes the necessity of collecting training data labeled with ground truth information. This approach would circumvents some of the inherent problems referenced above: it is unfeasible to fully explore at training time all of the contact situations a robotic finger might encounter when deployed. We believe the DISCO Finger makes for a very promising hardware platform to experiment with such end-to-end, model-free methods where tactile features are learned from raw signals at the same time as the task.

Chapter 8: Towards practical integration in robot hands

Despite the constant development of new tactile sensors, their use in practical applications is still limited. Many tactile sensors are built to work under controlled laboratory conditions with little consideration for deployment on real robots. In this chapter we focus on some important aspects that enable the use of our DISCO Finger in robot hands.

We present several improvements on the hardware aspect of our sensors, including changes to the amplification of the photodiode signals, design changes to the flexboard to improve reliability and the addition of a new outer opaque layer to keep ambient light out and further protect the reflective layer. On the software side, we show that it is possible to use previously trained forward models on newly built DISCO Fingers without the need to collect new training data. We also study the relationship between the number of signals used to build the forward model and the resulting localization and force prediction accuracy. Finally we demonstrate the stability over time of the forward model.

8.1 Hardware and manufacturing improvements

The design and manufacturing of our DISCO Finger poses several challenges from a packaging and reliability perspective. A concern when using a flexible circuit board stems from controlling bending stress along the areas where the components are placed. Excessive bending can cause the electronic pins to break off from the pads causing a complete failure in the circuit or an intermittent contact.

The first version of our flexboard uses both sides of the board to distribute the electronic components: the front side houses all optical components (LEDs and photodiodes) and the back side contains all the operational amplifiers needed to serve each photodiode. This scheme simplifies the board routing but complicates the manufacturing process as the backside of the board contains both components and the stiffener layer. Tooling limitations meant the components in the backside needed to be soldered manually. This caused reliability issues, as several prototypes developed intermittent or failed contacts during our own finger manufacturing.

To address this issue, we introduced a new design where all components are placed on the front side of the flexboard, leaving the backside to hold only the 300 µm thick stiffener layer (up from 200 µm in the previous design). This new design maintains 32 LEDs in the same locations but removes 2 photodiodes (for a total of 28) in favor of placing operational amplifiers in the central area of the board, as routing the board with all operational amplifiers in the periphery of the optical components was not possible. With this constraint in place, we analyzed the drop in performance when removing the signals corresponding to the removed photodiodes and found no significant difference. Ground planes were also introduced on both the front and back side of the board. Figure 8.1 shows the new flexboard design compared to the original.

Another issue with our original flexboard stems from the design of the transimpedance amplifier. All photodiodes have a capacitance value that is correlated to the reverse bias voltage applied.

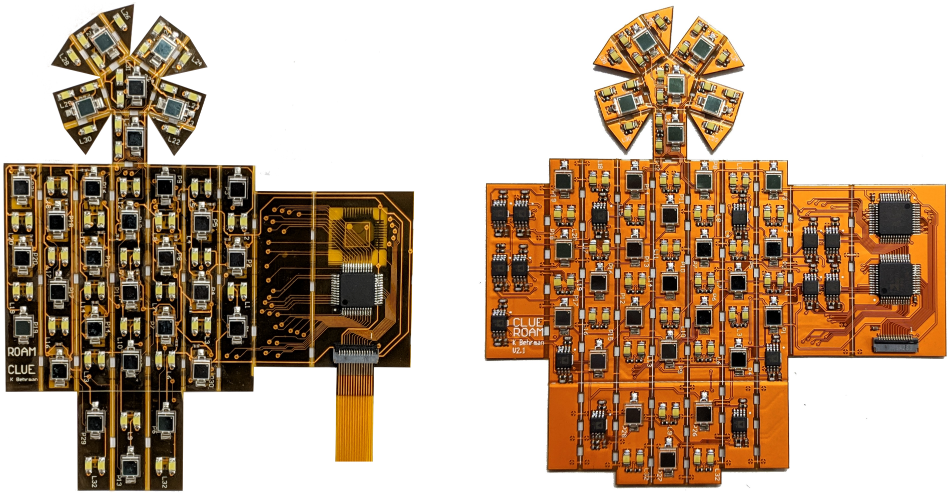

Figure 8.1: New flexboard design for the DISCO Finger (right) compared to our first iteration (left). All components are now placed in the front side of the board to allow a full stiffener layer on the backside to improve reliability. Two photodiodes had to be removed to accommodate operational amplifiers in the central area of the board.

The reverse bias increases the width of the depletion region and lowers the junction capacitance. In our design, the photodiode is operating in what is called "photovoltaic mode" where no external bias is applied. The input offset voltage in this mode is very low which allows large gains without any large output offset voltage. However, the capacitance across the input terminals of the operational amplifier introduces a low-pass filter in the feedback path which can cause stability issues. To improve stability a feedback capacitor is added as shown in Figure 8.2.

Our original design did not have this feedback capacitor and operated at a high gain that caused instability as shown in Figure 8.2. To get around this problem an in-line low-pass filter with a cutoff frequency at 100Khz was used on the FFC cable going from the DISCO finger to the controller board. On the new flexboard we incorporated a 4pF feedback capacitor which solved the instability and results in a settling time of approximately 8 us. This settling time is a big contributor to the system overall sampling frequency since the ADC conversion time is much lower at around 4 us. Future hardware revisions might consider the possibility of applying a reverse voltage to the photodiode to reduce the junction capacitance and enable higher frequency operation.

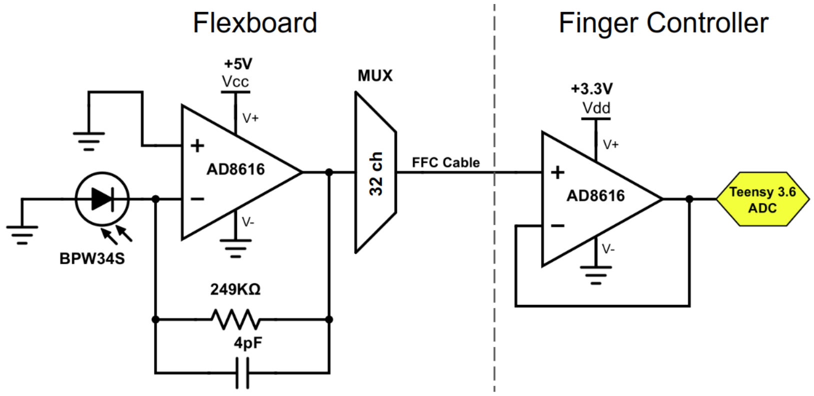

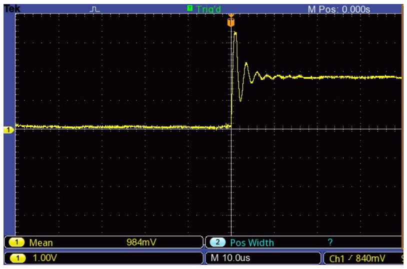

Step response without feedback capacitor

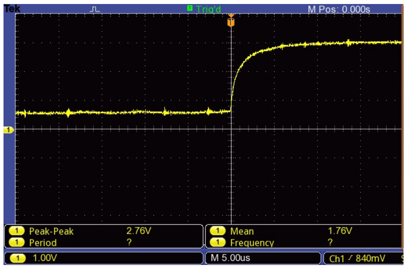

Step response with 4pF feedback capacitor

Figure 8.2: Transimpedance amplifier circuit used for our photodiodes and step response with and without feedback capacitor. Dashed line shows the divide of hardware placed on the flexboard and on the finger controller board.

Finally, another concern with our approach is related to how we deal with ambient light to make sure our DISCO Finger performs consistently across different lightning conditions. The reflective coating function is two-fold: it guides light inside the finger elastomer volume and it also blocks out external light to make sure the photodiodes output stays consistent to the level required during our equalization routine. Using a particle based reflective material makes it hard to achieve a truly opaque layer, especially because the reflective particles separate and let more outside light when strain is applied. This is the reason why, at each sampling time, we measure the ambient light which is then subtracted to obtain the feature vector that is the input to our model.

The subtraction of ambient light can only be effective if the photodiode response is completely linear. While photodiodes are very linear devices, phenomena like the amplifier input bias current can introduce non-linearities that are hard to account for. For this reason, we decided a simple but effective solution is to completely isolate our system from outside light by adding an extra black layer in our manufacturing process. To add this extra layer we use PDMS at a 1:10 curing agent ratio infused with 5% black silicone pigment from Smooth-On ("Silc Pig"). We add three layers via dipping the finger in a vat containing the black silicone followed by curing at 80° C for 40 minutes. The result is shown in Figure 8.3.

Figure 8.3: We add a black opaque layer of silicone to the DISCO Finger to remove any ambient light from leaking into the finger

8.2 Model transfer

Probably one the biggest limitations of our data-driven method is the need to collect ground truth data for model-based control methods that make use of explicitly derived contact parameters, such as contact location and normal force. The collection of this type of data requires specialized equipment and instrumentation as well as a significant time investment for the user. This can become prohibitively expensive if each individual finger requires its own training process. We are interested in investigating the possibility of transferring the forward model learned on one finger to another one with minimal loss of performance.

Each finger goes through an equalization process where we adjust the LED brightness for each individual LED-photodiode combination such that the photodiode output signal is close to the middle of the ADC range. This process takes place with the finger in an "undisturbed" state (no contact). For many pairs, even with the LED at full brightness, the output signal does not reach the desired equalization level, as not enough light reaches the photodiode. Manufacturing differences make it such that different LEDs and photodiodes can have different intensities and sensitivity respectively. Moreover, our own manufacturing processes can introduce more variability as the reflective coating can yield different light transport efficiency on different fingers. As a consequence, different fingers present different signal values at baseline.

The feature vector used in the previous chapter is composed of the absolute value reported by each LED-photodiode pair combination (960 signals) after the subtraction of an ambient light measurement. As different fingers present different a different feature vector at baseline, it is evident this scheme does not allow for the forward model to be transfered from a finger to another.

Using our latest design iteration, we propose using a differential scheme: the feature vector is constructed with the change in each signal with respect to a baseline measurement taken while the finger is undisturbed. With our new boards having 32 LEDs and 28 photodiodes, this results in a feature vector with a dimensionality of 896. As discussed in the previous section, we do not need to subtract ambient light with the added black opaque layer on the finger. Our hypothesis is that

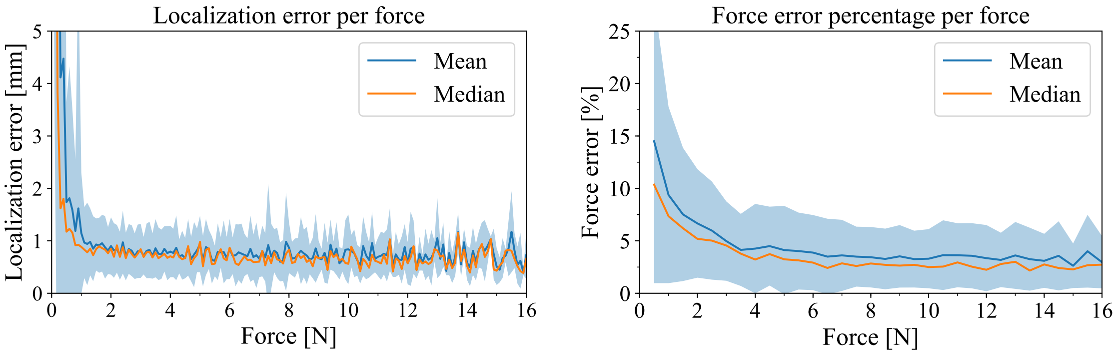

Benchmark performance: Trained on finger #16, tested on #16

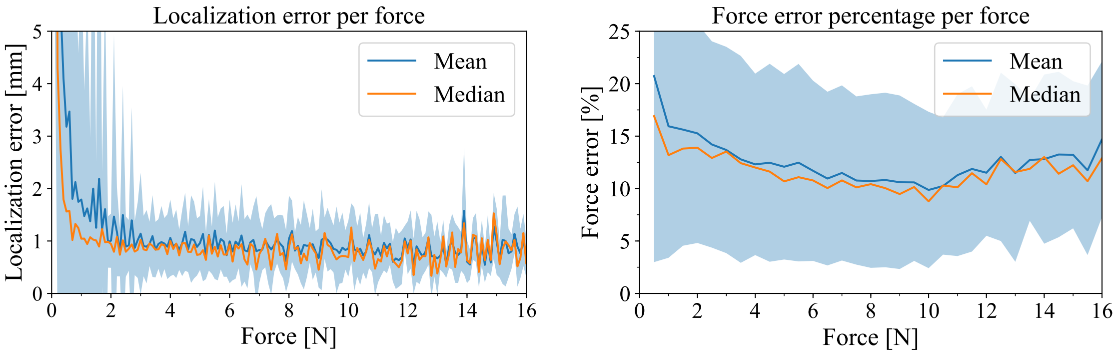

Model transfer performance: Trained on fingers #17, #19 and #22, tested on #16

Figure 8.4: Localization and force prediction accuracy. **Top:** Benchmark performance is given by a model constructed using training and test data collected on the same finger. **Down:** The transfered model is trained on three separate fingers and then tested on a forth finger.

this differential scheme will squash the difference in signal levels between fingers, allowing us to train a single model and deploy it across many fingers. It must be noted that some manufacturing differences between fingers do not necessarily manifest as a simple DC voltage offset. Any misalignment in how the flexboard is glued to the 3D printed skeleton or positional variations in how the components are soldered onto the flexboard will yield a different signal pattern instead of a level shift. However, we think it is possible to be robust to these misalignments (as long as they are small) if we collect training data across many fingers to capture these variations.

To test our hypothesis, we collect training data across four different fingers and compare the localization and force prediction accuracy between two different models. We will identify each finger with its unique ID : #16, #17, #19 and #22. The first model will be our benchmark and is trained using 12 datasets (as defined in section 7.4) from finger #16 and tested on a 13th dataset also from that finger. The second model is trained using 4 datasets from each finger #17, #19 and #22 and tested on finger #16. Figure 8.4 shows the resulting accuracy of both models. Compared to the results obtained on the previous chapter, our benchmark displays similar performance in localization and a slight improvement on the force error standard deviation. The model transfer performs very similar to the benchmark albeit with worse accuracy for small forces and a slightly higher standard deviation across all forces. Force error performance shows a significantly higher mean error, between 15 and 10%, compared to the benchmark.

8.3 Signal selection and sampling rate

In the previous chapter we investigated how many of the 960 signals carried useful information and found that 917 of them exceeded a value of three times its own standard deviation in the undisturbed state (in response to an indentation somewhere on the finger surface).

It is expected that maximum performance is likely achieved when sampling all signals. However, if we sample a subset of signals we can achieve a greater sampling rate while trading off some localization and force prediction accuracy. In this section we will investigate this trade-off as it can provide the final user the flexibility to opt for higher sampling rates based on the application requirements. We propose the use of signal energy as a proxy to measure the amount of information carried by a particular signal. The energy of a discrete signal x is defined as

$$\varepsilon_x = \sum_{n=-\infty}^{\infty} |x[n]|^2$$

Intuitively a signal with a high energy value is that one which responds strongly to numerous contact events along the finger surface. On the other side, a signal with a low energy value either only responds in certain locations or possibly has a weaker response across many locations. This would be the case for a signal where the LED is distant to the photodiode. For this study we will assume that higher energy signals have a higher contribution to the system final performance. To compute the energy of a given LED-photodiode pair we use all contact data points in our

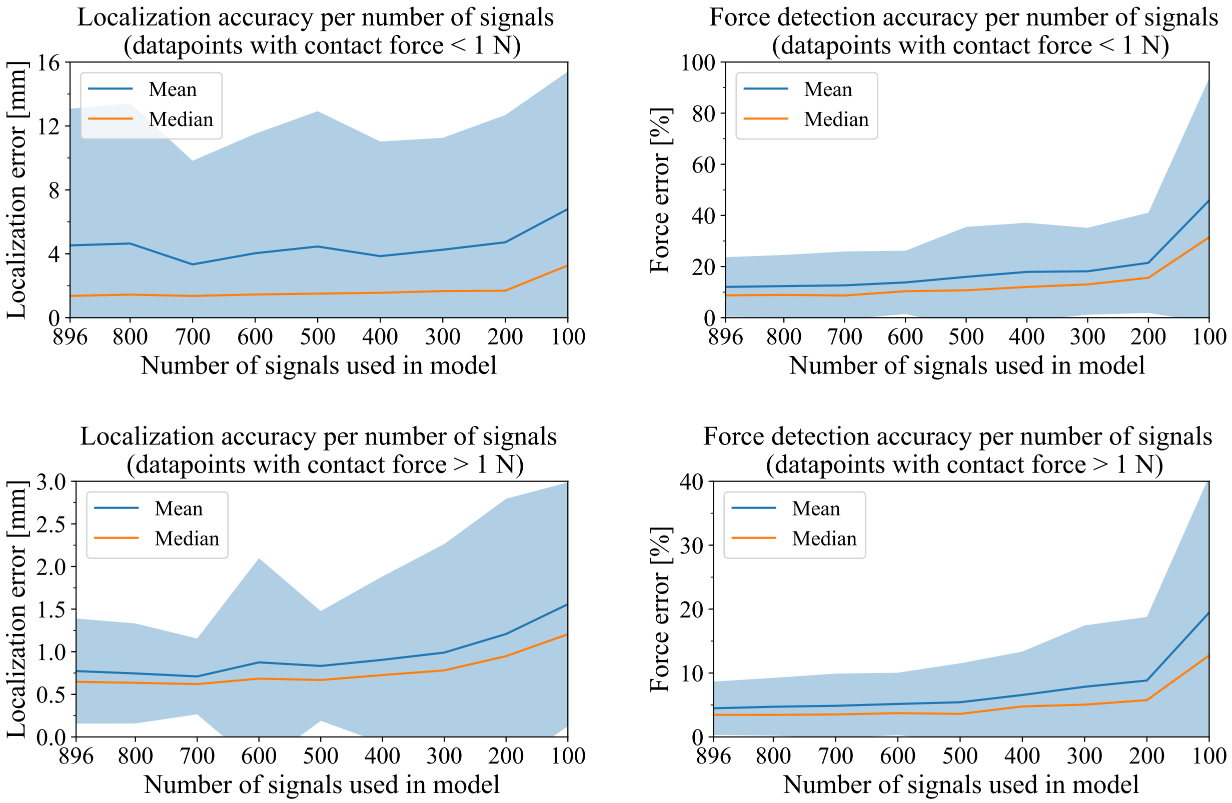

Figure 8.5: Localization and force prediction accuracy as a function of the number of signals used as features. Top and bottom plots show the performance for all datapoints corresponding to low and high contact forces respectively.

training datasets (we filter out non-contact datapoints). After we compute the energy of each LED-photodiode pair we build a ranking in descending order for energy value.

We train several models using progressively smaller subsets of the top ranked (highest energy) signals. We use the same datasets described for our benchmark in the previous section, using 12 datasets for training and a 13th dataset for testing (all corresponding to finger #16). The baseline we compare against is the performance when the model is trained using all 896 signals. In Figure 8.5 we report the aggregated mean and median error for localization and mean force percentage error across datapoints with contact forces lower and greater than 1 N in our test set. We report results separately for these two subsets of data (low and high force datapoints) to more accurately reflect how performance is affected on each case. Complete results for localization and force prediction accuracy per force can be found in Appendix B.

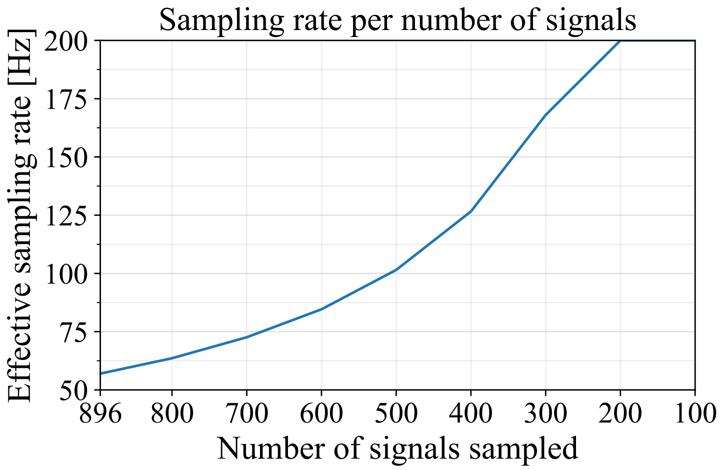

Figure 8.6: Sampling rate measured at the host PC connected to a finger controller board as we sample different numbers of signals. The sampling rate shown here is the effective rate at which the ROS messages arrive containing the values for each LED-photodiode pair in the DISCO Finger.

These results show us that exists some redundancy in our signals since a percentage of them can be ignored and still obtain acceptable performance out of the system. In particular, localization accuracy seems to be less affected by the removal of low energy signals, while force accuracy seems to follow a more linear relationship with the number of signals sampled. For each one of the models presented here, we also analyzed if the remaining signals resulted in the exclusion of hardware components (either an LED or photodiode). Interestingly, it is not until you use the top 100 ranked energy signals that you exclude enough signals to allow hardware components to not be used. For models with 200 or more signals, there is always at least one useful signal associated with each LED or photodiode (hence all hardware components are needed to achieve the signal subset that makes up the model).

Figure 8.6 shows the resulting effective sampling rate for the different subsets of signals. The sampling time for the ADC module is linear in the number of signals, however we show the effective sampling time measured on the host PC which receives the ROS message containing the values for all the signals. Inefficiencies in the rosserial protocol (which we use to communicate between the finger controller board and the host PC) make it impossible to achieve a sampling rate higher than 200 Hz without messages being dropped and checksums failures, which is why the values at 200 and 100 signals are capped at 200 Hz.

8.4 Stability over time

An important characteristic to deploy a tactile finger such as ours is that the forward model is stable over time and does not require constant re-training. It is important that the localization and force predictions maintain a certain level of accuracy over time, even when operating at a much later date with respect to the data collected to train the forward model.

To evaluate this characteristic in the DISCO finger, we present in Figure 8.7 the resulting performance as tested on a dataset collected about a month after the training data used to build the forward model. Our benchmark performance shown in Figure 8.7, Top, is the same one used for the

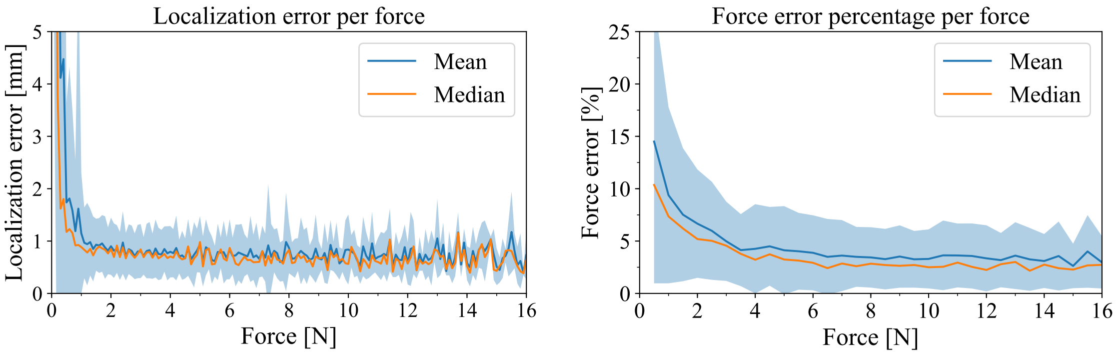

Benchmark performance: Trained on finger #16, tested on #16

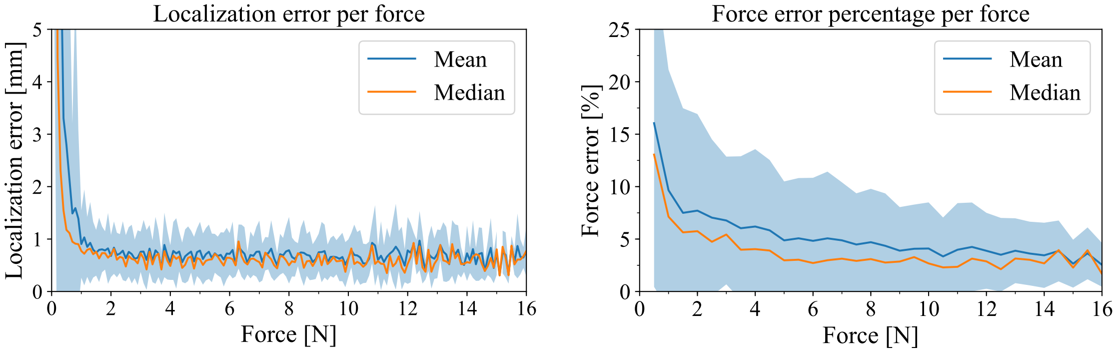

Stability over time: Test data collected a month after benchmark

Figure 8.7: Resulting performance when using a test dataset taken a month later with respect to the training data. Similar performance between our benchmark (Top) where the test data was collected shortly after the training data and a new test dataset collected a month later (Bottom) indicates our model is stable over time and does not require re-training periodically.

model transfer evaluation. The figures at the bottom show the performance when using the same model but using test data collected a month later with respect to the test data for the benchmark.

Results show no loss of performance on localization, while force accuracy presents slightly higher standard deviation and a similar mean and median error.

8.5 Discussion

In this chapter we demonstrate the possibility of transferring a purely data-driven model from one DISCO Finger to another. Our model transfer analysis is particularly important from a practical perspective. It allows us to focus our efforts in building a single robust forward model that can be deployed on many fingers, instead of having to collect training data for each individual finger. Results show that localization performance is almost unaffected when using this model on a new finger. Force predictions, however, show an increase in the mean error across our operational force range. It is possible that a separate regressor specialized for force, as opposed to the multi-task neural network architecture we use, can be more robust and capture the differences between fingers more effectively. It is also possible more training data can improve this metric as well, especially if collected across an even larger number of fingers.

On the hardware side, we present several improvements and further analysis on the latest design iteration of our DISCO Finger. Our hardware improvements have resulted in a more reliable system which is more robust to accidental bending during the manufacturing process of the finger. Improved stability in the photodiodes transimpedance amplification circuit results in less overall noise in our signals as we can sample more consistently while switching LED-photodiode pairs at high frequencies. Adding a black opaque layer to our finger ensures our photodiodes only respond to changes in light provoked by disturbances in the finger surface. Moreover, it allows operation under very different and dynamic lighting situations.

Our spatially overlapping signals method provides us with a large number of signals that encode the deformation of the finger surface as it interacts with objects. The individual contribution of each signal can be very variable. In particular we know that some LED-photodiode pairs can be ignored if a small amount of light from the LED reaches the photodiode. This is the case when the photodiode is physically far away from the LED, even if during the equalization process we configure the LED brightness to its maximum possible setting. Skipping these signals can be beneficial as it can increase the system overall sampling rate. A complete ablation study over 896 signals would require a lot of computational power, which is why in this chapter we used the energy as a proxy to indicate how much information a signal carries. We assume here that higher energy signals have a higher contribution to the localization and force prediction, although this might not be a perfect approximation. Manual inspection does reveal that all the lower ranked signals under this scheme correspond to distant LED-photodiode combinations. Results show that, for our selected touch features, there is enough redundancy to remove a significant portion of our signals and still obtain a model that yields similar performance in both localization and force predictions.

Another interesting approach regarding the signal selection study could be to weight signals differently not only based on their energy level, but also on the location of their receptive fields. One could argue that it is important to maintain the highest performance in the fingertip area of a finger, while it is acceptable to decrease it elsewhere.

Our stability over time test provides important insight into the maintenance aspect of the DISCO Finger in a real application. This test could be improved by performing a stress test in the time interval between the collection of training data and the test data. Such test would cyclically apply forces and friction in many areas of the finger and could inform not only about the stability over time of the model with repeated use, but also about the general durability of the finger outer layer and the system as a whole.

Chapter 9: Conclusion

9.1 Summary of contributions

In this dissertation we aim to address the shortcomings of tactile sensors which limit their use in robot hands. To bridge the existing gap between stand-alone *tactile sensors* and fully integrated *tactile fingers*, we identify coverage, shape and packaging as three fundamental practical aspects that cannot be overlooked if we are to advance the state of the art in grasping and manipulation capabilities of robot hands. At the same time, we cannot neglect the importance of spatial resolution and force sensitivity or such efforts will be for naught. In this context, the spatially overlapping signals method developed in this dissertation successfully tackles these shortcomings.

Our piezoresistive sensor can accurately localize contact on a volume of soft piezoresistive material using only 4 wires. With our MEMS-based tactile dome, we demonstrate the use of FEA simulation tools to aid the sensor design and guide the placement of sensing terminals inside a volume of soft rubber. This dome can accurately localize contact along a spherical surface thanks to the optimized placement of only five Takktile pressure transducers. Our planar optical sensor prototypes demonstrate the capability to localize touch with sub-millimeter accuracy and predict the indentation depth very precisely due to our tuning of the elastomer layer thickness to leverage two separate modes of interaction between the indenter probe and the waveguide. With these sensors we also show the ability to classify different indenter shapes and the sensor performance robustness when encountering a new indenter geometry not previously seen at training time. The final realization of our method comes in the form of our DISCO Finger, a soft tactile robot finger capable of resolving contact locations with 1 *mm* accuracy and determine the normal contact force with 5-10% error over a non-developable three-dimensional surface, in a fully integrated, finger-shaped package. With this finger, we show that it is possible to extract multitouch information from the spatially overlapping signal set.

Overall, we show a transduction-agnostic method that moves away from the traditional taxel paradigm in favor of promoting large overlapping receptive fields that result from terminal pair measurements. This method demonstrates we can maximize the number of signals extracted from a sensor while minimizing the number of wires by taking measurements across all possible pairs of sensing terminals. Across three different transduction methods, we have shown that it is possible to use a purely data-driven approach to extract information from the rich spatially overlapping signal set and map these signals to contacts parameters such as location and force through the collection of data with ground truth labels. Moreover, we believe the results presented in this dissertation make a strong case towards using this methodology to build data-rich sensors that can be used in the continuously evolving field of end-to-end learning to acquire meaningful manipulation skills.

9.2 Challenges and limitations

Our data-driven method enables the deployment of sensing terminals on soft materials with the ability to provide coverage on arbitrary non-planar geometry with simple manufacturing methods and circumvent the need of an analytical model for the sensor. However, there are some limitations to this approach. To predict a contact parameter, we must dedicate enough time to collect training data with ground truth using specialized equipment. In our case, to predict location of touch and indenter force, this includes a 6 degrees of freedom robot arm with a force sensing linear probe used as an end effector.

Another issue is scalability. To obtain a robust contact location model, its necessary to provide a large number of training examples with the indenter contacting the finger across all of its surface. Once we add a second parameter, such as normal force, for each location example we also need to sweep through different applied forces. Adding shear forces would entail even more data, as well as the required equipment to provide the ground truth measurements. Prediction of multitouch presents a similar problem, as we need to sweep through all possible combinations of two contacts. What about three contacts? This is the problem of parametrization of contacts. A general way to encode most of these phenomena would be to discretize the finger surface and predict the pressure or displacement for each cell. We do not show that capability in this study due to the difficulty of collecting ground truth data for such a model, although such approach has been reported in the literature [76].

Perhaps a possible approach to remedy some of these limitations is to use simulation tools whenever available for the transduction method of choice. In chapter 5 we showed the use of FEA simulation can aid in optimizing the location of strain sensing terminals. For our tactile dome, this is possible because of the existence of commercial software capable of solving for the propagation of stress from the surface deformation to each Takktile pressure transducer. Our piezoresistive sensor would require an complex software capable of modeling how the material deformation results in the creation of conductive paths inside the doped elastomer. For optical sensors, this means a ray tracing software combined with FEA analysis to determine the surface deformation and the resulting change in light transport. If such simulation tools are available they can not only aid in the sensor design but, if accurate enough, be used to generate synthetic data and replace the data collection on the physical sensor, or at least significantly reduce the amount of real data needed.

9.3 Future work

There are some paths we can follow to improve the work presented in this dissertation. From a hardware perspective there are many optimizations that could improve the performance of our DISCO Finger. A complete ablation study to determine the impact of each signal on the final performance could inform which sensing terminals (LEDs or photodiodes) can feasibly be removed to reduce the cost and simplify the design of our flexboard. Modifying the transimpedance amplifier to work in photoconductive mode (applying a reverse bias on the photodiode) can increase the width of the photodiode depletion region and lower the junction capacitance, improving the high-frequency performance and enabling higher sampling rates. However this also requires new tuning of the feedback capacitor value to stabilize the system. From a firmware perspective, an interesting possibility is to adopt the use of an auto-encoder to obtain a lower dimensional representation of our signals, which could dramatically reduce the size of the data packet sent to the host PC and improve the performance of reinforcement learning algorithms making use of this latent representation [120].

Another important improvement to our DISCO finger would be to reduce its general footprint, which is approximately 2 times larger than a human finger. The main driver behind the geometry of our finger is the footprint of the electronic components in our flexboard and the number of facets used to follow the finger curvature. Using smaller components, especially photodiodes and operational amplifiers, could significantly reduce the size of the overall package. A modified flexboard design could also extend the sensor coverage to the back of the finger. Both of these tasks would significantly improve our DISCO Finger, but are not without challenges in terms of the flexboard design.

When considering future research directions, we start from the premise that a robot tactile finger must ultimately serve as an enabler for robotic manipulation. How does the work presented here fit in this bigger picture? We believe that are two main avenues for integration of such a tactile finger into a complete manipulation system.

First, model-based control and learning methods for manipulation such as Model Predictive Control [131, 132] make direct use of explicitly derived contact properties, such as contact location and force. For locally convex objects where we can expect a single contact location per finger link, we have shown that we can train machine learning models to provide such information with very high accuracy, and over a large functional surface without blind spots. This can enable a wide range of methods that need this information, e.g., to formulate and solve stability analysis or motion equations for the hand-object system.

The second avenue, one that has recently shown tremendous promise in complex robotic motor control problems, is that of end-to-end, model-free sensorimotor learning [133–137]. These methods learn a direct mapping from raw sensor data to motor commands. Any intermediate representations of the sensor data are learned at the same time as the task itself, without ground truth other than the general reward signal related to task success. In this context, one would use our sensors to directly train manipulation skills, without the need to collect labeled ground truth for intermediate representations such as contact shape or location. The classifiers and regressors we quantify here serve to illustrate the fact that the raw sensor data indeed comprises rich information pertaining to contact, and suggest our sensors can be used for end-to-end learning.

Reinforcement learning methods generally require large amounts of data, which may not be feasibly gathered with a real robot. A common workaround is to utilize simulated environments, along with domain randomization to then transfer the learned policies to a real robot. Accurate simulated physics models of soft contacts and forces remain elusive, which means simulating the raw signals of our optical sensors could prove challenging. As a result, it will be important over the next years to develop effective methods to make our reinforcement learning algorithms more sample efficient. Perhaps equally important will be to develop methods to enable robots to acquire more general skills that can be applied to many different tasks.

It is hard to imagine a future where robots are not deployed in human environments and working side by side with humans. The road to that future will be a long one as roboticists still work to develop robots capable of sorting and packaging objects, assist the elderly and the sick or drive us around in unstructured and dynamic environments. However, most of the tasks we envision future robots performing involve the robot physically interacting with the world. This puts grasping and manipulation skills in a critical path towards that future. We believe the contributions in tactile sensing made in this dissertation will prove to be an important enabler towards enhancing complex motor skills in robot hands.

References

[1] Kris Doelling, Jeongsik Shin, and Dan O Popa. "Service robotics for the home: a state of the art review". In: *Proceedings of the 7th International Conference on PErvasive Technologies Related to Assistive Environments*. ACM. 2014, p. 35.

[2] Dorian J Spero. "A review of outdoor robotics research". In: (2004).

[3] Russell H Taylor et al. "Medical robotics and computer-integrated surgery". In: *Springer handbook of robotics*. Springer, 2016, pp. 1657–1684.

[4] Robert Bogue. "Growth in e-commerce boosts innovation in the warehouse robot market". In: *Industrial Robot: An International Journal* 43.6 (2016), pp. 583–587.

[5] G Westling and RS Johansson. "Factors influencing the force control during precision grip". In: *Experimental brain research* 53.2 (1984), pp. 277–284.

[6] Roland S Johansson and J Randall Flanagan. "Coding and use of tactile signals from the fingertips in object manipulation tasks". In: *Nature Reviews Neuroscience* 10.5 (2009), p. 345.

[7] Jason R Wingert et al. "Tactile sensory abilities in cerebral palsy: deficits in roughness and object discrimination". In: *Developmental Medicine & Child Neurology* 50.11 (2008), pp. 832–838.

[8] Wei Chen et al. "Tactile sensors for friction estimation and incipient slip detection—toward dexterous robotic manipulation: A review". In: *IEEE Sensors Journal* 18.22 (2018), pp. 9049–9064.

[9] Shan Luo et al. "Robotic tactile perception of object properties: A review". In: *Mechatronics* 48 (2017), pp. 54–67.

[10] Mark R Cutkosky, Robert D Howe, and William R Provancher. "Force and tactile sensors". In: *Springer Handbook of Robotics* (2008), pp. 455–476.

[11] Ravinder S Dahiya et al. "Tactile sensing - from humans to humanoids". In: *IEEE Transactions on Robotics* 26.1 (2010), pp. 1–20.

[12] Hanna Yousef, Mehdi Boukallel, and Kaspar Althoefer. "Tactile sensing for dexterous in-hand manipulation in robotics—A review". In: *Sensors and Actuators A: physical* 167.2 (2011), pp. 171–187.

[13] Mallory L Hammock et al. “25th Anniversary Article: The Evolution of Electronic Skin (E-Skin): A Brief History, Design Considerations, and Recent Progress”. In: *Advanced Materials* 25.42 (2013), pp. 5997–6038.

[14] Zhanat Kappassov, Juan-Antonio Corrales, and Véronique Perdereau. “Tactile sensing in dexterous robot hands—Review”. In: *Robotics and Autonomous Systems* 74 (2015), pp. 195–220.

[15] Artur Saudabayev and Huseyin Atakan Varol. “Sensors for robotic hands: A survey of state of the art”. In: *IEEE Access* 3 (2015), pp. 1765–1782.

[16] Ravinder S Dahiya et al. “Directions toward effective utilization of tactile skin: A review”. In: *IEEE Sensors Journal* 13.11 (2013), pp. 4121–4138.

[17] James C. Craig Jayne M. Kisner. “Factors affecting tactile spatial acuity”. In: *Somatosensory & motor research* 15.1 (1998), pp. 29–45.

[18] Robert H LaMotte and Mandayam A Srinivasan. “Tactile discrimination of shape: responses of slowly adapting mechanoreceptor afferents to a step stroked across the monkey fingerpad”. In: *Journal of Neuroscience* 7.6 (1987), pp. 1655–1671.

[19] Liang Zou et al. “Novel tactile sensor technology and smart tactile sensing systems: A review”. In: *Sensors* 17.11 (2017), p. 2653.

[20] Antonio Bicchi and Vijay Kumar. “Robotic grasping and contact: A review”. In: *Proceedings 2000 ICRA. Millennium Conference. IEEE International Conference on Robotics and Automation. Symposia Proceedings (Cat. No. 00CH37065)*. Vol. 1. IEEE. 2000, pp. 348–353.

[21] Martin Grunwald. *Human haptic perception: Basics and applications*. Springer Science & Business Media, 2008.

[22] Q. Wan, R. P. Adams, and R. Howe. “Variability and Predictability in Tactile Sensing During Grasping”. In: *IEEE International Conference on Robotics and Automation*. IEEE. 2016, pp. 158–164.

[23] Oliver Kroemer, Christoph H Lampert, and Jan Peters. “Learning dynamic tactile sensing with robust vision-based training”. In: *IEEE transactions on robotics* 27.3 (2011), pp. 545–557.

[24] Robert D Howe and Mark R Cutkosky. “Integrating tactile sensing with control for dextrous manipulation”. In: *Proc. IEEE Int. Workshop Intell. Motion Control*. Vol. 1. 1990, pp. 369–374.

[25] Allison M Okamura, Niels Smaby, and Mark R Cutkosky. “An overview of dexterous manipulation”. In: *Proceedings 2000 ICRA. Millennium Conference. IEEE International Conference on Robotics and Automation. Symposia Proceedings (Cat. No. 00CH37065).* Vol. 1. IEEE. 2000, pp. 255–262.

[26] Aude Billard and Danica Kragic. “Trends and challenges in robot manipulation”. In: *Science* 364.6446 (2019).

[27] Ilge Akkaya et al. “Solving rubik’s cube with a robot hand”. In: *arXiv preprint arXiv:1910.07113* (2019).

[28] OpenAI: Marcin Andrychowicz et al. “Learning dexterous in-hand manipulation”. In: *The International Journal of Robotics Research* 39.1 (2020), pp. 3–20.

[29] Charles S Smith. “Piezoresistance effect in germanium and silicon”. In: *Physical review* 94.1 (1954), p. 42.

[30] Stefano Stassi et al. “Flexible tactile sensing based on piezoresistive composites: A review”. In: *Sensors* 14.3 (2014), pp. 5296–5332.

[31] Alex Chortos and Zhenan Bao. “Skin-inspired electronic devices”. In: *Materials Today* 17.7 (2014), pp. 321–331.

[32] Jeff Dusek et al. “Carbon black-PDMS composite conformal pressure sensor arrays for near-body flow detection”. In: *OCEANS 2014-TAIPEI*. IEEE. 2014, pp. 1–7.

[33] Darren J Lipomi et al. “Skin-like pressure and strain sensors based on transparent elastic films of carbon nanotubes”. In: *Nature nanotechnology* 6.12 (2011), p. 788.

[34] Kyun Kyu Kim et al. “Highly sensitive and stretchable multidimensional strain sensor with prestrained anisotropic metal nanowire percolation networks”. In: *Nano letters* 15.8 (2015), pp. 5240–5247.

[35] Stefan CB Mannsfeld et al. “Highly sensitive flexible pressure sensors with microstructured rubber dielectric layers”. In: *Nature Materials* 9.10 (2010), p. 859.

[36] Steve Park et al. “Stretchable energy-harvesting tactile electronic skin capable of differentiating multiple mechanical stimuli modes”. In: *Advanced Materials* 26.43 (2014), pp. 7324–7332.

[37] X Alice Wu et al. “Tactile sensing for gecko-inspired adhesion”. In: *Intelligent Robots and Systems (IROS), 2015 IEEE/RSJ International Conference on*. IEEE. 2015, pp. 1501–1507.

[38] Yong-Lae Park, Bor-Rong Chen, and Robert J Wood. “Design and fabrication of soft artificial skin using embedded microchannels and liquid conductors”. In: *IEEE Sensors Journal* 12.8 (2012), pp. 2711–2718.

[39] Daniel M Vogt, Yong-Lae Park, and Robert J Wood. “Design and characterization of a soft multi-axis force sensor using embedded microfluidic channels”. In: *IEEE Sensors Journal* 13.10 (2013), pp. 4056–4064.

[40] Frank L Hammond et al. “Soft tactile sensor arrays for force feedback in micromanipulation”. In: *IEEE Sensors Journal* 14.5 (2014), pp. 1443–1452.

[41] David Holder. *Electrical impedance tomography: methods, history and applications*. CRC Press, 2004.

[42] Akihiko Nagakubo, Hassan Alirezaei, and Yasuo Kuniyoshi. “A deformable and deformation sensitive tactile distribution sensor”. In: *Robotics and Biomimetics, 2007. ROBIO 2007. IEEE International Conference on*. IEEE. 2007, pp. 1301–1308.

[43] Yo Kato et al. “Tactile sensor without wire and sensing element in the tactile region based on EIT method”. In: *Sensors*. IEEE. 2007, pp. 792–795.

[44] David Silvera Tawil, David Rye, and Mari Velonaki. “Touch modality interpretation for an EIT-based sensitive skin”. In: *Robotics and Automation (ICRA), 2011 IEEE International Conference on*. IEEE. 2011, pp. 3770–3776.

[45] Hassan Alirezaei, Akihiko Nagakubo, and Yasuo Kuniyoshi. “A tactile distribution sensor which enables stable measurement under high and dynamic stretch”. In: *3D User Interfaces, IEEE Symposium on*. IEEE. 2009, pp. 87–93.

[46] David Silvera-Tawil et al. “Electrical impedance tomography for artificial sensitive robotic skin: A review”. In: *IEEE Sensors Journal* 15.4 (2015), pp. 2001–2016.

[47] Alexander Gruebele et al. “A stretchable capacitive sensory skin for exploring cluttered environments”. In: *IEEE Robotics and Automation Letters* 5.2 (2020), pp. 1750–1757.

[48] Kenichiro Suzuki, Khalil Najafi, and Kensall D Wise. “A 1024-element high-performance silicon tactile imager”. In: *IEEE Transactions on Electron Devices* 37.8 (1990), pp. 1852–1860.

[49] Bart J Kane, Mark R Cutkosky, and Gregory TA Kovacs. “A Traction Stress Sensor Array for Use in High-Resolution Robotic Tactile Imaging”. In: *Journal of Microelectromechanical Systems* 9.4 (2000), pp. 425–434.

[50] Hidekuni Takao, Kazuaki Sawada, and Makoto Ishida. “Monolithic Silicon Smart Tactile Image Sensor With Integrated Strain Sensor Array on Pneumatically Swollen Single-

Diaphragm Structure". In: *IEEE Transactions on Electron Devices* 53.5 (2006), pp. 1250–1259.

[51] Takao Someya et al. "A large-area, flexible pressure sensor matrix with organic field-effect transistors for artificial skin applications". In: *Proceedings of the National Academy of Sciences* 101.27 (2004), pp. 9966–9970.

[52] Makoto Shimojo et al. "A tactile sensor sheet using pressure conductive rubber with electrical-wires stitched method". In: *IEEE Sensors* 4.5 (2004), pp. 589–596.

[53] Dae-Hyeong Kim et al. "Stretchable and foldable silicon integrated circuits". In: *Science* 320.5875 (2008), pp. 507–511.

[54] Yaroslav Tenzer, Leif P Jentoft, and Robert D Howe. "The feel of MEMS barometers: Inexpensive and easily customized tactile array sensors". In: *IEEE Robotics & Automation Magazine* 21.3 (2014), pp. 89–95.

[55] Leif P Jentoft et al. "Flexible, stretchable tactile arrays from MEMS barometers". In: *2013 16th International Conference on Advanced Robotics (ICAR)*. IEEE. 2013, pp. 1–6.

[56] Christian Reeks et al. "Angled sensor configuration capable of measuring tri-axial forces for pHRI". In: *Robotics and Automation (ICRA), 2016 IEEE Int. Conf. on*. IEEE. 2016.

[57] Ravinder S Dahiya and Maurizio Valle. *Robotic tactile sensing: technologies and system.* Springer Science & Business Media, 2012.

[58] Panagiotis Polygerinos et al. "MRI-compatible fiber-optic force sensors for catheterization procedures". In: *IEEE Sensors Journal* 10.10 (2010), pp. 1598–1608.

[59] Jelizaveta Konstantinova, Agostino Stilli, and Kaspar Althoefer. "Fingertip fiber optical tactile array with two-level spring structure". In: *Sensors* 17.10 (2017), p. 2337.

[60] Alessandro Levi et al. "Soft, transparent, electronic skin for distributed and multiple pressure sensing". In: *Sensors* 13.5 (2013), pp. 6578–6604.

[61] Radhen Patel, Rebecca E Cox, and Nikolaus Correll. *Integrated force and distance sensing using elastomer-embedded commodity proximity sensors.* Tech. rep. Sandia National Lab.(SNL-NM), Albuquerque, NM (United States), 2017.

[62] IM Van Meerbeek, CM De Sa, and RF Shepherd. "Soft optoelectronic sensory foams with proprioception". In: *Science Robotics* 3.24 (2018), eaau2489.

[63] Kazuhiro Shimonomura. "Tactile image sensors employing camera: A review". In: *Sensors* 19.18 (2019), p. 3933.

[64] Stefan Begej. “Planar and finger-shaped optical tactile sensors for robotic applications”. In: *IEEE Journal on Robotics and Automation* 4.5 (1988), pp. 472–484.

[65] Wanlin Li et al. “An Elastomer-based Flexible Optical Force and Tactile Sensor”. In: *2019 2nd IEEE International Conference on Soft Robotics (RoboSoft)*. IEEE. 2019, pp. 361–366.

[66] M. K. Johnson and E. H. Adelson. “Retrographic sensing for the measurement of surface texture and shape”. In: *IEEE Conference on Computer Vision and Pattern Recognition*. 2009, pp. 1070–1077.

[67] Siyuan Dong, Wenzhen Yuan, and Edward H Adelson. “Improved gelsight tactile sensor for measuring geometry and slip”. In: *2017 IEEE/RSJ International Conference on Intelligent Robots and Systems (IROS)*. IEEE. 2017, pp. 137–144.

[68] Elliott Donlon et al. “GelSlim: A High-Resolution, Compact, Robust, and Calibrated Tactile-sensing Finger”. In: *2018 IEEE/RSJ International Conference on Intelligent Robots and Systems (IROS)*. IEEE. 2018, pp. 1927–1934.

[69] Daolin Ma et al. “Dense Tactile Force Estimation using GelSlim and inverse FEM”. In: *International Conference on Robotics and Automation (ICRA)*. IEEE. 2019, pp. 5418–5424.

[70] Mike Lambeta et al. “DIGIT: A Novel Design for a Low-Cost Compact High-Resolution Tactile Sensor With Application to In-Hand Manipulation”. In: *IEEE Robotics and Automation Letters* 5.3 (2020), pp. 3838–3845.

[71] Wenzhen Yuan et al. “Measurement of shear and slip with a GelSight tactile sensor”. In: *2015 IEEE International Conference on Robotics and Automation (ICRA)*. IEEE. 2015, pp. 304–311.

[72] Wenzhen Yuan, Siyuan Dong, and Edward Adelson. “Gelsight: High-resolution robot tactile sensors for estimating geometry and force”. In: *Sensors* 17.12 (2017), p. 2762.

[73] Nathan F Lepora and Benjamin Ward-Cherrier. “Superresolution with an optical tactile sensor”. In: *IEEE/RSJ Intl. Conf. on Intelligent Robots and Systems*. IEEE. 2015, pp. 2686–2691.

[74] Benjamin Ward-Cherrier, Luke Cramphorn, and Nathan F Lepora. “Tactile manipulation with a TacThumb integrated on the open-hand M2 gripper”. In: *IEEE Robotics and Automation Letters* 1.1 (2016), pp. 169–175.

[75] Luke Cramphorn, John Lloyd, and Nathan F Lepora. “Voronoi features for tactile sensing: Direct inference of pressure, shear, and contact locations”. In: *2018 IEEE International Conference on Robotics and Automation (ICRA)*. IEEE. 2018, pp. 2752–2757.

[76] Carmelo Sferrazza et al. "Ground truth force distribution for learning-based tactile sensing: a finite element approach". In: *IEEE Access* 7 (2019), pp. 173438–173449.

[77] Rui Ouyang and Robert Howe. "Low-Cost Fiducial-based 6-Axis Force-Torque Sensor". In: *arXiv preprint arXiv:2005.14250* (2020).

[78] Branden Romero, Filipe Veiga, and Edward Adelson. "Soft, Round, High Resolution Tactile Fingertip Sensors for Dexterous Robotic Manipulation". In: *arXiv preprint arXiv:2005.09068* (2020).

[79] Akhil Padmanabha et al. "OmniTact: A Multi-Directional High Resolution Touch Sensor". In: *arXiv preprint arXiv:2003.06965* (2020).

[80] David Silvera Tawil, David Rye, and Mari Velonaki. "Improved image reconstruction for an EIT-based sensitive skin with multiple internal electrodes". In: *IEEE Transactions on Robotics* 27.3 (2011), pp. 425–435.

[81] Hyosang Lee et al. "Soft nanocomposite based multi-point, multi-directional strain mapping sensor using anisotropic electrical impedance tomography". In: *Scientific Reports* 7 (2017), p. 39837.

[82] David J van den Heever, Kristiaan Schreve, and Cornie Scheffer. "Tactile sensing using force sensing resistors and a super-resolution algorithm". In: *IEEE Sensors Journal* 9.1 (2009), pp. 29–35.

[83] Nathan F Lepora et al. "Tactile superresolution and biomimetic hyperacuity". In: *IEEE Transactions on Robotics* 31.3 (2015), pp. 605–618.

[84] Giorgio Cannata, Simone Denei, and Fulvio Mastrogiovanni. "Towards automated self-calibration of robot skin". In: *Robotics and Automation (ICRA), 2010 IEEE International Conference on*. IEEE. 2010, pp. 4849–4854.

[85] Luca Muscari et al. "Real-time reconstruction of contact shapes for large area robot skin". In: *International Conference on Robotics and Automation*. IEEE. 2013, pp. 2360–2366.

[86] Jacob W Guggenheim et al. "Robust and Inexpensive Six-Axis Force–Torque Sensors Using MEMS Barometers". In: *IEEE/ASME Transactions on Mechatronics* 22.2 (2017), pp. 838–844.

[87] Damith Suresh Chathuranga et al. "A soft three axis force sensor useful for robot grippers". In: *Intelligent Robots and Systems (IROS), 2016 IEEE/RSJ Int. Conf. on*. IEEE. 2016.

[88] Tiago Paulino et al. "Low-cost 3-axis soft tactile sensors for the human-friendly robot Vizzy". In: *Robotics and Automation (ICRA), 2017 IEEE International Conference on*. IEEE. 2017, pp. 966–971.

[89] Koh Hosoda, Yasunori Tada, and Minoru Asada. “Anthropomorphic robotic soft fingertip with randomly distributed receptors”. In: *Robotics and Autonomous Systems* 54 (Feb. 2006), pp. 104–109.

[90] Nicholas Wettels et al. “Biomimetic tactile sensor array”. In: *Advanced Robotics* 22.8 (2008), pp. 829–849.

[91] John Ulmen and Mark Cutkosky. “A Robust, Low-Cost and Low-Noise Artificial Skin for Human-Friendly Robots”. In: *IEEE International Conference on Robotics and Automation*. 2010, pp. 4836–4841.

[92] P. Mittendorfer and G. Cheng. “Humanoid Multimodal Tactile-Sensing Modules”. In: *IEEE Transactions on Robotics* 27.3 (2011), pp. 401–410.

[93] Alex Chortos, Jia Liu, and Zhenan Bao. “Pursuing prosthetic electronic skin”. In: *Nature materials* 15.9 (2016), pp. 937–950.

[94] Gereon H Buscher et al. “Flexible and stretchable fabric-based tactile sensor”. In: *Robotics and Autonomous Systems* 63 (2015), pp. 244–252.

[95] Gereon Buescher et al. “Augmenting Curved Robot Surfaces with Soft Tactile Skin”. In: *International Conference on Intelligent Robots and Systems*. IEEE. 2015, pp. 1514–1519.

[96] Clementine M. Boutry et al. “A hierarchically patterned, bioinspired e-skin able to detect the direction of applied pressure for robotics”. In: *Science Robotics* 3.24 (2018).

[97] Junghwan Byun et al. “Electronic skins for soft, compact, reversible assembly of wirelessly activated fully soft robots”. In: *Science Robotics* 3 (2018).

[98] Luke E. Osborn et al. “Prosthesis with neuromorphic multilayered e-dermis perceives touch and pain”. In: *Science Robotics* 3 (2018).

[99] Yuanzhao Wu et al. “A skin-inspired tactile sensor for smart prosthetics”. In: *Science Robotics* 3 (2018).

[100] Alin Drimus et al. “Design of a flexible tactile sensor for classification of rigid and deformable objects”. In: *Robotics and Autonomous Systems* 62.1 (2014), pp. 3–15.

[101] Joran W. Booth et al. “OmniSkins: Robotic skins that turn inanimate objects into multifunctional robots”. In: *Science Robotics* 3.22 (2018).

[102] Nicholas Wettels and Gerald E Loeb. “Haptic feature extraction from a biomimetic tactile sensor: force, contact location and curvature”. In: *2011 IEEE International Conference on Robotics and Biomimetics*. IEEE. 2011, pp. 2471–2478.

[103] Yasemin Bekiroglu et al. “Assessing grasp stability based on learning and haptic data”. In: *IEEE Transactions on Robotics* 27.3 (2011), pp. 616–629.

[104] J Schill et al. “Learning continuous grasp stability for a humanoid robot hand based on tactile sensing”. In: *2012 4th IEEE RAS & EMBS International Conference on Biomedical Robotics and Biomechatronics (BioRob)*. IEEE. 2012, pp. 1901–1906.

[105] Hao Dang and Peter K Allen. “Stable grasping under pose uncertainty using tactile feedback”. In: *Autonomous Robots* 36.4 (2014), pp. 309–330.

[106] Qian Wan and Robert D Howe. “Modeling the effects of contact sensor resolution on grasp success”. In: *IEEE Robotics and Automation Letters* 3.3 (2018), pp. 1933–1940.

[107] Francois R Hogan et al. “Tactile regrasp: Grasp adjustments via simulated tactile transformations”. In: *International Conference on Intelligent Robots and Systems (IROS)*. IEEE. 2018, pp. 2963–2970.

[108] Emil Hyttinen, Danica Kragic, and Renaud Detry. “Learning the tactile signatures of prototypical object parts for robust part-based grasping of novel objects”. In: *2015 IEEE international conference on Robotics and Automation (ICRA)*. IEEE. 2015, pp. 4927–4932.

[109] Miao Li et al. “Learning of grasp adaptation through experience and tactile sensing”. In: *International Conference on Intelligent Robots and Systems*. IEEE. 2014, pp. 3339–3346.

[110] H. Dang and P. K. Allen. “Grasp adjustment on novel objects using tactile experience from similar local geometry”. In: *2013 IEEE/RSJ International Conf. on Intelligent Robots and Systems*. 2013, pp. 4007–4012.

[111] Bohan Wu et al. “MAT: Multi-fingered adaptive tactile grasping via deep reinforcement learning”. In: *arXiv preprint arXiv:1909.04787* (2019).

[112] Martin Meier et al. “Tactile convolutional networks for online slip and rotation detection”. In: *International Conference on Artificial Neural Networks*. Springer. 2016, pp. 12–19.

[113] Ruben D Ponce Wong, Randall B Hellman, and Veronica J Santos. “Haptic exploration of fingertip-sized geometric features using a multimodal tactile sensor”. In: *Next-Generation Robots and Systems*. Vol. 9116. International Society for Optics and Photonics. 2014, p. 911605.

[114] David Watkins-Valls, Jacob Varley, and Peter Allen. “Multi-modal geometric learning for grasping and manipulation”. In: *2019 International conference on robotics and automation (ICRA)*. IEEE. 2019, pp. 7339–7345.

[115] Michelle A Lee et al. "Making sense of vision and touch: Self-supervised learning of multimodal representations for contact-rich tasks". In: *2019 International Conference on Robotics and Automation (ICRA)*. IEEE. 2019, pp. 8943–8950.

[116] Yang Gao et al. "Deep learning for tactile understanding from visual and haptic data". In: *2016 IEEE International Conference on Robotics and Automation (ICRA)*. IEEE. 2016, pp. 536–543.

[117] Roberto Calandra et al. "The feeling of success: Does touch sensing help predict grasp outcomes?" In: *arXiv preprint arXiv:1710.05512* (2017).

[118] Roberto Calandra et al. "More than a feeling: Learning to grasp and regrasp using vision and touch". In: *IEEE Robotics and Automation Letters* 3.4 (2018), pp. 3300–3307.

[119] Herke Van Hoof et al. "Learning robot in-hand manipulation with tactile features". In: *2015 IEEE-RAS 15th International Conference on Humanoid Robots (Humanoids)*. IEEE. 2015, pp. 121–127.

[120] Herke Van Hoof et al. "Stable reinforcement learning with autoencoders for tactile and visual data". In: *2016 IEEE/RSJ international conference on intelligent robots and systems (IROS)*. IEEE. 2016, pp. 3928–3934.

[121] Stephen Tian et al. "Manipulation by feel: Touch-based control with deep predictive models". In: *2019 International Conference on Robotics and Automation (ICRA)*. IEEE. 2019, pp. 818–824.

[122] Giovanni Sutanto et al. "Learning latent space dynamics for tactile servoing". In: *2019 International Conference on Robotics and Automation (ICRA)*. IEEE. 2019, pp. 3622–3628.

[123] Roberta L Klatzky and Susan J Lederman. "Touch". In: *Handbook of psychology* (2003), pp. 147–176.

[124] N. Hu et al. "Piezoresistive strain sensors made from carbon nanotubes based polymer nanocomposites". In: *Sensors* 11.11 (2011).

[125] C.X. Liu and J.W. Choi. "Improved dispersion of carbon nanotubes in polymers at high concentrations". In: *Nanomaterials* 2.4 (2012).

[126] D Roşca. "New uniform grids on the sphere". In: *Astronomy & Astrophysics* 520 (2010), A63.

[127] David A Chang-Yen, Richard K Eich, and Bruce K Gale. "A monolithic PDMS waveguide system fabricated using soft-lithography techniques". In: *Journal of lightwave technology* 23.6 (2005), p. 2088.

[128] DK Cai et al. “Optical absorption in transparent PDMS materials applied for multimode waveguides fabrication”. In: *Optical materials* 30.7 (2008), pp. 1157–1161.

[129] Ziliang Cai et al. “A new fabrication method for all-PDMS waveguides”. In: *Sensors and Actuators A: Physical* 204 (2013), pp. 44–47.

[130] Pedro Piacenza et al. “Accurate contact localization and indentation depth prediction with an optics-based tactile sensor”. In: *Robotics and Automation (ICRA), 2017 IEEE International Conference on*. IEEE. 2017, pp. 959–965.

[131] Emanuel Todorov and Weiwei Li. “A generalized iterative LQG method for locally-optimal feedback control of constrained nonlinear stochastic systems”. In: *Proceedings of the 2005, American Control Conference, 2005.* IEEE. 2005, pp. 300–306.

[132] Tom Erez, Yuval Tassa, and Emanuel Todorov. “Infinite-horizon model predictive control for periodic tasks with contacts”. In: *Robotics: Science and systems VII* (2012), p. 73.

[133] S. Levine, N. Wagener, and P. Abbeel. “Learning Contact-Rich Manipulation Skills with Guided Policy Search”. In: *IEEE Intl. Conf. on Robotics and Automation*. 2015.

[134] S. Levine et al. “Learning Hand-Eye Coordination for Robotic Grasping with Deep Learning and Large-Scale Data Collection”. In: *Intl. Symp. on Experimental Robotics*. 2016.

[135] Fereshteh Sadeghi and Sergey Levine. “CAD2RL: Real Single-Image Flight without a Single Real Image”. In: *CoRR* abs/1611.04201 (2016).

[136] Xue Bin Peng et al. “Sim-to-Real Transfer of Robotic Control with Dynamics Randomization”. In: *CoRR* abs/1710.06537 (2017).

[137] Marcin Andrychowicz et al. “Learning Dexterous In-Hand Manipulation”. In: *CoRR* abs/1808.00177 (2018).

Appendix A: DISCO Finger mapping

We use an extension of a projection developed by Roşca[126], which maps a uniform square grid in a two-dimensional (A, B) space to a near-uniform grid on a half-sphere embedded in three-dimensional space (x, y, z). This parameterization also aims to preserve local areas as much as possible. Note that this (A, B) space is dimensionless. We use this method directly for the hemispherical chapter of our finger surface (depicted in red in Figure 7.5), which is mapped to a square in (A, B) space. The equator of the sphere thus corresponds to the outer perimeter of the square, and each side of the square gets mapped to a 90° arc along the equator. Formally, a point in the red region of (A, B) space gets mapped to a Cartesian hemisphere of radius r centered at the origin as follows.

If $0 < |B| \leq |A| \leq L$:

$$\begin{aligned} x &= \frac{2A}{\pi}\sqrt{\pi - \frac{A^2}{r^2}} cos\left(\frac{B\pi}{4A}\right) && \text{(A.1)} \\ y &= \frac{2A}{\pi}\sqrt{\pi - \frac{A^2}{r^2}} sin\left(\frac{B\pi}{4A}\right) && \text{(A.2)} \\ z &= r - \frac{2A^2}{\pi r} - d && \text{(A.3)} \end{aligned}$$

If $0 < |A| \leq |B| \leq L$:

$$\begin{aligned} x &= \frac{2B}{\pi}\sqrt{\pi - \frac{B^2}{r^2}} sin\left(\frac{A\pi}{4B}\right) && \text{(A.4)} \\ y &= \frac{2B}{\pi}\sqrt{\pi - \frac{B^2}{r^2}} cos\left(\frac{A\pi}{4B}\right) && \text{(A.5)} \\ z &= r - \frac{2B^2}{\pi r} - d && \text{(A.6)} \end{aligned}$$

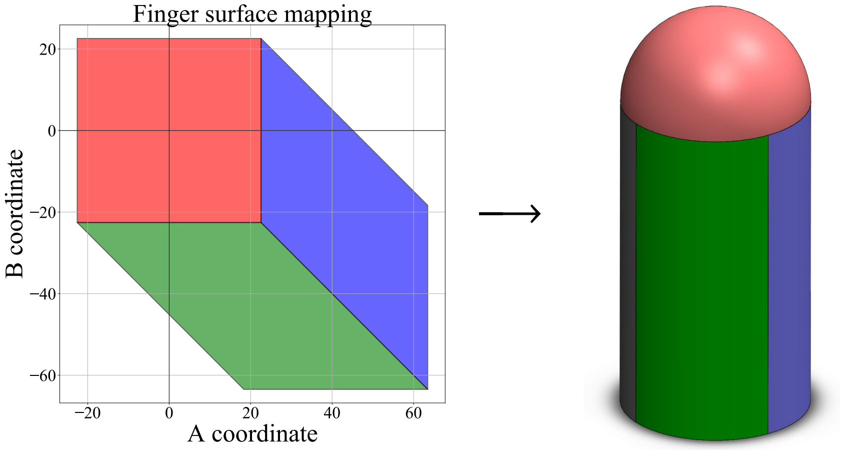

Figure A.1: Finger surface parameterization into two-dimensional (A, B) space

where $L = r\sqrt{\frac{\pi}{2}}$ and $d = 0$.

We then use different values of d to extend beyond the hemispherical tip and onto the cylindrical part of our finger. Starting from the (A, B) square that maps our sphere, we extend the two sides corresponding to 180° of the equator to represent the sensorized area of the cylindrical body. In keeping with the original projection, these new regions are extended such that their areas in (A, B) match the frontal area of the cylinder. Formally, points in the blue or green regions of (A, B) space (Figure 7.5) are projected into Cartesian (x, y, z) space as follows. The first step comprises a projection onto the edge of the red region of (A, B) space:

$$(A^p, B^p) = (L + A + B, -L) \quad \text{if } (A, B) \in \text{green region} \tag{A.7}$$

$$(A^p, B^p) = (L, A + B - L) \quad \text{if } (A, B) \in \text{blue region} \tag{A.8}$$

we then compute d as follows:

$$d = \alpha\sqrt{(A^p - A)^2 + (B^p - B)^2} \tag{A.9}$$

where α is a scaling factor computed as the ratio between the real cylinder height and L2 norm of the segment where the green region meets the blue region. Finally, the projected values (A^p, B^p) along with d are plugged back into Eqs.(A.1-A.6) to obtain the Cartesian (x, y, z) values for the points on the cylindrical area of the finger.

Appendix B: DISCO Finger performance versus sampling rate graphs

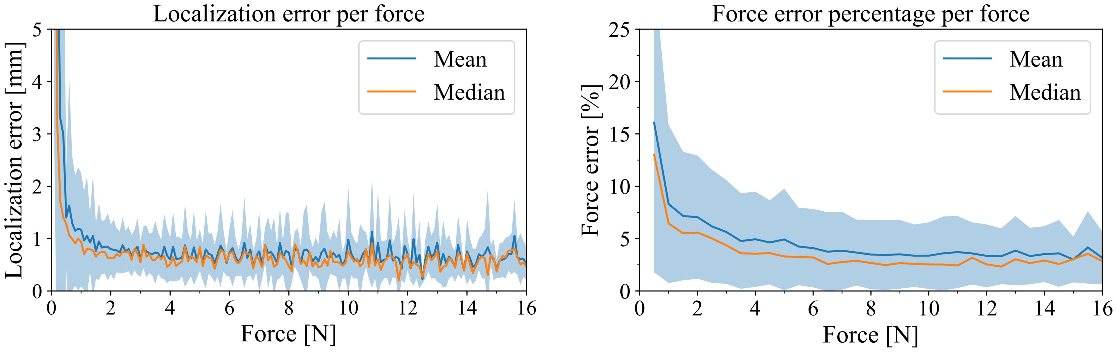

Model trained on top ranking 800 signals

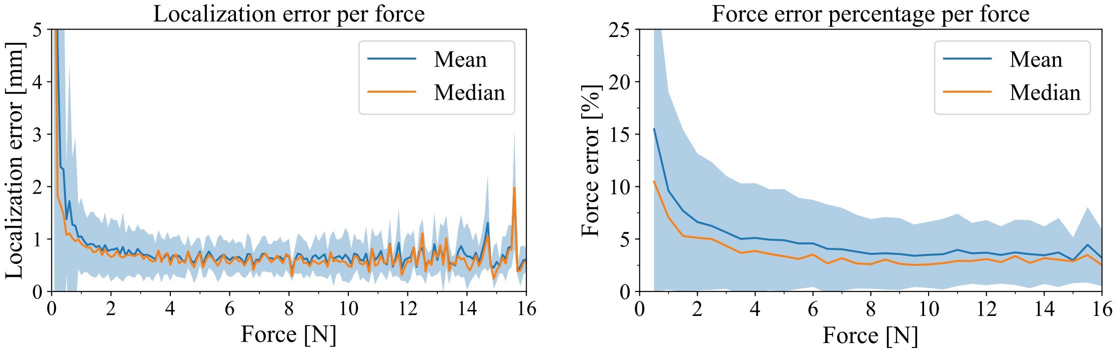

Model trained on top ranking 700 signals

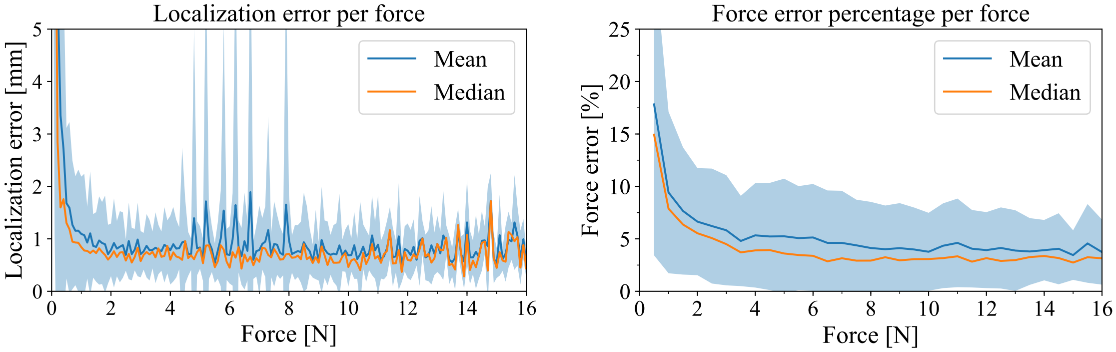

Model trained on top ranking 600 signals

Figure B.1: DISCO Finger localization and force prediction performance for models trained on the top 800, 700 and 600 ranked energy signals

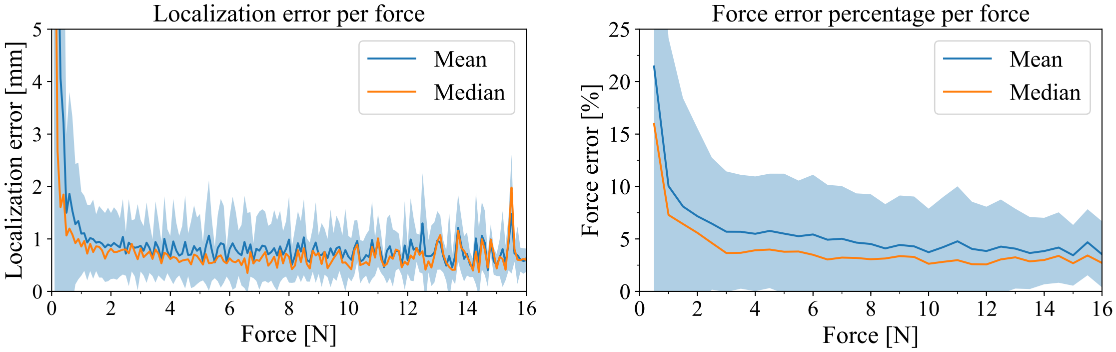

Model trained on top ranking 500 signals

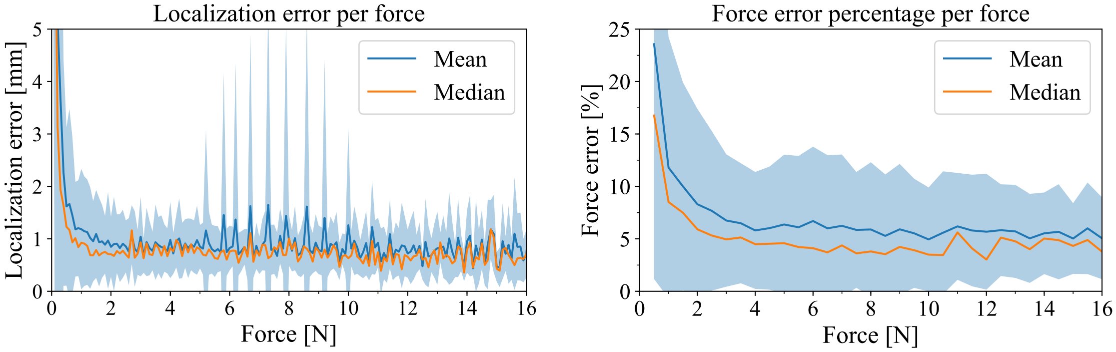

Model trained on top ranking 400 signals

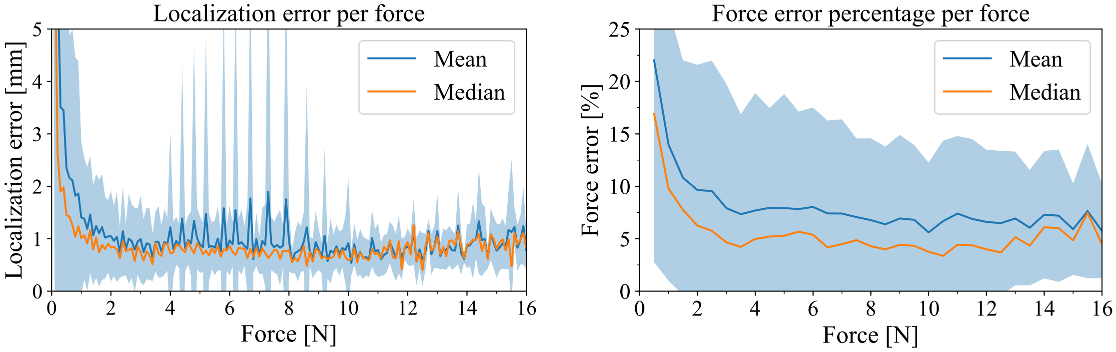

Model trained on top ranking 300 signals

Figure B.2: DISCO Finger localization and force prediction performance for models trained on the top 500, 400 and 300 ranked energy signals

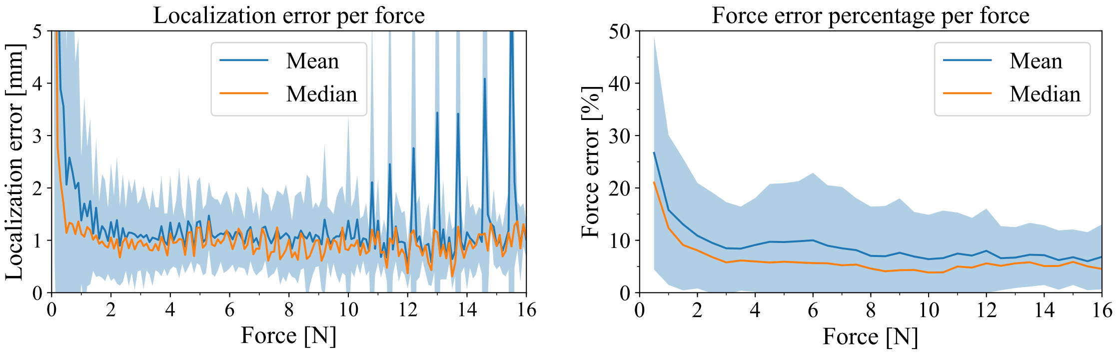

Model trained on top ranking 200 signals

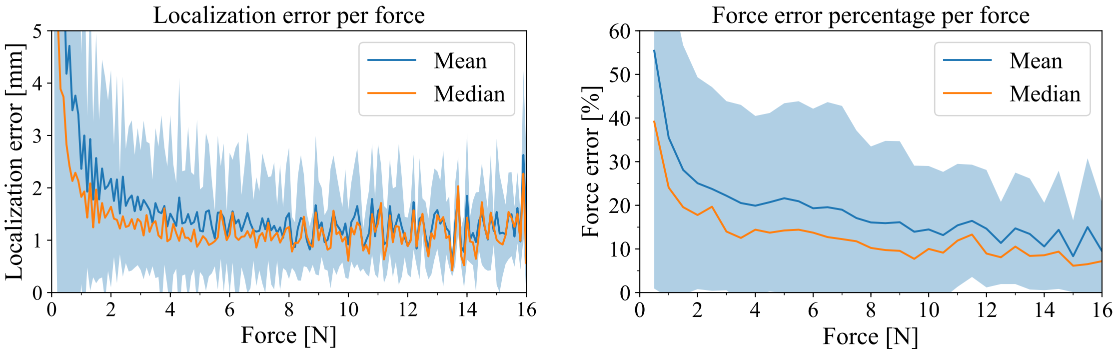

Model trained on top ranking 100 signals

Figure B.3: DISCO Finger localization and force prediction performance for models trained on the top 200 and 100 ranked energy signals